Volume 54
Number 19
7 October 2025
Pages 8527–9118

Chem Soc Rev

Chemical Society Reviews

rsc.li/chem-soc-rev

ISSN 0306-0012

ROYAL SOCIETY OF CHEMISTRY

REVIEW ARTICLE
Zhongwu Li and Aleksandr Noy
Carbon nanotube nanofluidics

Chem Soc Rev

REVIEW ARTICLE

View Article Online
View Journal | View Issue

Cite this: *Chem. Soc. Rev.*, 2025, **54**, 8582

Carbon nanotube nanofluidics†

Zhongwu Li [a] and Aleksandr Noy *[ab]

Fluid flow under extreme spatial confinement exhibits unusual physical behaviors. This *nanofluidic* transport regime is relevant to a variety of mass transport, separation, and energy production processes in biological and industrial systems. Carbon nanotubes (CNTs) offer a nearly ideal platform for exploring nanofluidic transport because of their extremely narrow, smooth, hydrophobic inner pores, which enable very fast molecular flow while providing strong selectivity. In this review, we aim to provide a comprehensive understanding of nanofluidics in CNTs, focusing on the basic physics of mass transport in CNTs, various experimental platforms developed to investigate these phenomena, and key results on the permeation of water, protons, and ions. We focus on the critical factors that influence transport efficiency and selectivity, such as slip flow and charge regulation in CNTs, and the roles of entrance effects, dehydration processes and ion–charge interactions at the CNT entrances. We also explore the confinement effects, highlighting how the unique one-dimensional structure of CNTs imposes distinct constraints on fluid behavior and leads to novel single-file transport phenomena. Finally, we address current challenges and future directions of CNT nanofluidics.

Received 4th March 2025

DOI: 10.1039/d5cs00233h

rsc.li/chem-soc-rev

1 Nanofluidics: fluid flow in very small channels

Over the last 50 years, water, ion, and proton transport through channels with at least one dimension below 100 nm has been studied in many experimental and modeling studies across

[a] *Materials Science Division, Physical and Life Sciences Directorate, Lawrence Livermore National Laboratory, Livermore, CA 94550, USA. E-mail: noy1@llnl.gov*
[b] *School of Natural Sciences, University of California Merced, Merced, CA 95344, USA*

† Electronic supplementary information (ESI) available. See DOI: https://doi.org/10.1039/d5cs00233h

Zhongwu Li

Zhongwu Li is currently a postdoctoral researcher at Lawrence Livermore National Laboratory (LLNL). He received his BE and PhD in Mechanical Engineering from the China University of Mining and Technology (2015) and Southeast University (2021), respectively, including joint PhD training at LLNL. His research focuses on nanofluidic transport at the nano- and sub-nanoscale, integrating experiments, modeling, and simulations to study interfacial, confinement, and quantum effects. He develops artificial nanofluidic channels from a variety of nanomaterials and integrates them into biomimetic architectures. These efforts enable membrane and bioiontronic applications in energy, separation, sensing, and computing.

Aleksandr Noy

Aleksandr Noy is a Senior Research Scientist at the Materials Science Division at the Lawrence Livermore National Laboratory (LLNL). He joined LLNL in 1998 as its first EO Lawrence Fellow after getting his PhD in Physical Chemistry from Harvard University and became an Indefinite Career Staff Scientist in 2001. His research group works at the intersection of nanoscience, biomaterials, and bioengineering, with the core research activities centering on nanofluidics and transport in highly confined environments of nanotube pores, precision separations in other nanomaterials platforms, and neuromorphic ionic computing. Since 2005 Noy has also served as an Adjunct Professor at the University of California Merced. He is a Fellow of the Materials Research Society.

various disciplines.[1–3] Researchers quickly noticed that transport in these *nanofluidic* channels, which have a very high surface-to-volume ratio and create spatial confinement that can approach the single molecule scale, exhibited unusual physical phenomena not observed on the more common *microfluidic* scale. Water and ions would flow through incredibly small and seemingly impassable pores;[4–6] water would spontaneously enter highly hydrophobic channels[4] or become electrically dead,[7] and ions would seemingly violate impregnable rules of condensed matter physics.[8]

In the past 20 years, nanofluidics has emerged as a distinct field driven by advances in nanofabrication technologies, development of new instruments and tools, and adoption of sophisticated modeling approaches.[9–11] These advancements have enabled the fabrication of individual artificial channels,[12,13] allowing researchers to investigate the fluid flow in nanometer and even sub-nanometer confinement.[9] One-dimensional (1D) nanotubes[14,15] and two-dimensional (2D) materials,[16–19] such as those made from carbon,[20–22] boron nitride,[23–26] molybdenum disulfide,[27–31] or MXenes,[32–34] are now routinely available to study nanofluidic transport. Consequently, the exploration of nanoscale fluid behaviors and related phenomena has become more controllable and reproducible, enhancing its relevance to many areas of nanoscience and nanotechnology,[35,36] and enabling a wide range of nanofluidic applications that include biosensors,[37–42] membrane separation,[43–46] energy harvesting[47–51] and neuromorphic ionic computing.[52–58]

As confinement in the channel reaches the range of 1 to 100 nm, surfaces and interfaces start to dominate the transport (Fig. 1).[1,35] At this scale, new physical phenomena and mechanisms emerge that are not observed in microfluidic or bulk scale channels.[10,59] For example, very low surface friction at the channel wall can cause the slip lengths for fluid flows in carbon nanotubes (CNTs) to reach up to tens of micrometers, playing a crucial role in the fast water transport phenomena,[6,25,60] which we will discuss in subsequent sections. Another example is the reorientation and inductive polarization effects from the hierarchical layering of interfacial water, which significantly reduce the effective radial dielectric constant, resulting in electrically dead water inside the CNT.[59,61,62] Indeed, Geim and co-workers observed abnormally low water dielectric constants in a related class of channels—graphite nanoslits.[7] Reducing the size of water-filled nanochannels from 100 nm to 1 nm caused the average radial dielectric constant to drop from ~80 to ~2, reflecting the insufficient number of water molecules for effective dielectric screening in the highly confined, "single-digit nanopore" regime.

At sub-nanometer confinement levels (<1 nm), short-range steric forces, such as van der Waals (vdW) and steric-hydration interactions, become more prominent, and the structure of the confined fluid starts to deviate significantly from the bulk configuration.[22,63] For example, water molecules can only fit into 0.8-nm-diameter CNTs as a single-file chain[64] and, similarly, a graphene nanoslit with a height of 0.4 nm fits only one molecular layer of water.[65] Under these conditions, the classical mechanics and thermodynamic equations, such as the Navier–Stokes,[1] Kelvin,[66] Hertz–Knudsen,[67] and Nernst–Einstein[68,69] equations, come under strain. Researchers who studied voltage-controlled streaming currents in 2D graphene slits also observed unexpected coupling between ion and water transport.[70] Furthermore, under such strong confinement the length scales associated with fluid dynamics become comparable to the characteristic length scales of the electrons in the confining solids.[71,72] Indeed, recent experiments reported coupling between water flows and electronic currents.[73,74] These observations suggest that discrete particle effects are significant, and it is necessary to describe the confining solids at the level of condensed matter physics rather than simply as passive walls impenetrable to fluids.

The phenomena discussed in the previous paragraphs primarily arise from confinement-related surface effects inside a channel, but entrance effects can also influence nanofluidic transport. For nanometer-scale confinements, pressure or electric field losses in the surrounding bath and at the entrance or exit of the nanochannel cannot be neglected.[75,76] Charges at the nanochannel entrance can influence the nearby fluid, thereby affecting the overall flow in and out of the channel.[77–79] In sub-nanometer confinement, water molecules must adapt to the narrow channel configuration by reducing the number of hydrogen bonds that they form.[22] For example, to enter a sub-1 nm CNT, each water molecule must lose two hydrogen bonds out of the four it forms in the bulk state.[80] Similarly, when ions enter a narrow channel, their hydration shells reorient or lose some water molecules, reducing the overall screening.[69,81,82] The additional energy required for this transition is responsible for the dehydration barrier that could prevent ions from entering the channel, unless there is a

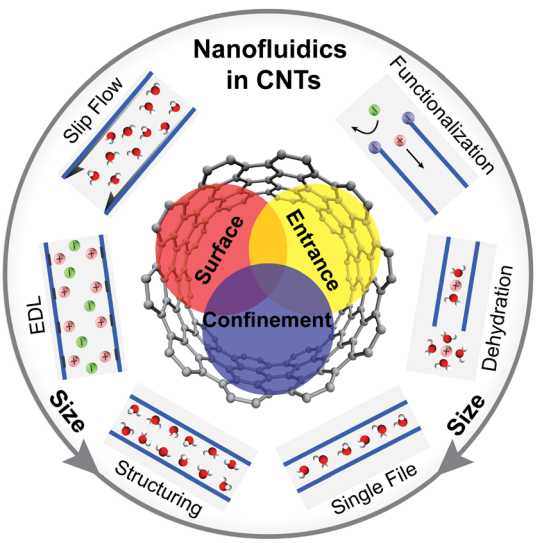

Fig. 1 Key physical phenomena and mechanisms that govern nanofluidic transport in CNT pores. Key mechanisms include surface interactions that determine fluid slip and electrostatic coupling, entrance effects that include dehydration and interaction with charged functional groups, and confinement effects that encompass fluid ordering and single-file transport.

compensating attraction between the ions and the channel wall.[69,82–84]

The remarkable transport physics seen in these channels demands an experimental platform that, in the words of G. Whitesides, is *easy, flexible, and data-rich*. Biological ion channels[85–87] and traditional membrane materials have traditionally provided the bulk of the experimental information about transport under spatial confinement, but both of these systems suffer from additional complexity resulting from their structure as well as from sophisticated functionality that they are required to perform. For example, aquaporin (AQP) water channels[88–90] need to balance the conflicting tasks of being extremely permeable to water while blocking proton transport. Synthetic artificial water channels can show remarkable performance,[91,92] but their structure is often complicated by moieties that enable these molecules to stack in the membrane and form pores, or they only form a transient pore.

Artificial nanofluidic devices can be classified into 0D pores or holes, 1D tubes, and 2D channels (note that 2D channels are beyond the scope of this review).[10,22,35] Early 0D nanopores, typically a few nanometers in diameter, were created by drilling thin Si_3N_4 membranes using transmission electron microscopy (TEM) or focused ion beam (FIB).[93–95] Another 0D platform employs atomically thin 2D materials, such as graphene or MoS_2, suspended over perforated Si_3N_4 membranes. These platforms feature (sub)nanometer pores from intrinsic defects or formed by etching,[29,31,96–101] but they typically require complex cleanroom fabrication, complicating experimental measurements. 1D nanofluidic channels can be formed in polymer membranes (*e.g.*, polyethylene terephthalate or polycarbonate) using track etching or FIB milling.[102–104] These methods produce various pore shapes, cylindrical, conical or funnel-like, but still lack nanometer-scale precision. Alternatively, glass nanopipettes fabricated by pulling capillaries[57,105] provide simple 1D channels, but do not offer sub-nanometer confinement or atomic surface control.

By Whitesides' criteria, a CNT stands out as a simple model channel offering a well defined purely cylindrical pore with strong confinement, well-defined pore size and smooth chemically-inert pore walls with tunable electronic properties.[15,20,106] Their inner cavities form 1D channels for fluids, which can be extensively studied through experiments[5,6,13,25,60,64,69,74,79,81,107–146] and simulations.[4,76,147–173] Molecularly-smooth inner surfaces of CNTs facilitate ultrafast transport.[4,64] Moreover, CNTs can be synthesized with different chiralities, allowing fabrication of channels with well-defined diameters and electronic properties.[21,174–176] CNTs are normally terminated with COOH functional groups that allow extensive chemical modifications of the pore entrances,[79,177] and they can be integrated into synthetic structures[25,126,136] and lipid membranes.[178,179] As we will discuss further in this article, this combination of nanoscale geometry, unique structure and surface properties, as well as easy tunability of the major structural features of the CNTs, has allowed researchers to use these channels to observe and study fast water transport,[6,25,60,64] enhanced proton conductance,[121,180] tunable ion selectivity,[64,81,115,145] unusual ion conductance scaling,[122,136,145] strong water–ion coupling,[114,126,132] and unusual ion transport mechanisms.[68,69]

The relative simplicity of the CNT structure has also been a boon for simulation efforts. Since the pioneering simulation of fast water diffusion in sub-nanometer CNTs by Hummer *et al.*[4] in 2001, numerous experimental platforms and simulation models have been developed to explore nanofluidics in CNTs.[4–6,13,25,60,64,69,74,76,79,81,107–173] While several review articles have highlighted the importance of nanofluidic materials, devices, and their applications,[14,22,36,38–40,42,45,46,51,85,86,181–183] a comprehensive review specifically focusing on the nanofluidic transport phenomena in CNTs is notably absent. Moreover, despite significant progress in CNT nanofluidics, many uncertainties remain regarding the mechanisms of water and ion transport, or even the nature of the reported conductance enhancements.[9,184,185] In this review, we examine promising findings from various experimental studies on CNT nanofluidics, discuss the key mechanisms governing fluid transport, and emphasize significant observations and unresolved questions in this field.

We begin with a foundational overview of nanofluidics, focusing on key length scales in nanometer-scale confinement. Next, we provide an overview of the CNT structure, electronic properties and CNT fabrication approaches relevant to nanofluidic systems. We then explore the origins of nanofluidic phenomena in CNTs and briefly summarize the experimental platforms and modeling methods employed in CNT nanofluidics. Subsequently, we discuss water, ion and proton transport in CNTs, and discuss it in terms of the dominant roles played by CNT walls, entrances, and spatial confinement. We also focus on the latest advances in nanofluidics in sub-nanometer CNT porins (CNTPs) and describe how these transport phenomena extend beyond classical fluid dynamics. We end with a discussion of challenges and future directions for CNT nanofluidics.

2 How small is small?

A significantly increased surface-to-volume ratio in nanochannels leads to fluid flow being dominated by interfacial interactions. This effect becomes especially pronounced when channel sizes shrink to just a few nanometers. For example, if we assume an interatomic interaction range of a, the ratio of the number of surface atoms (those within this interaction range) to the total number of atoms in a square cross-section channel can be estimated as $(x^2 - (x - 2a)^2)/x^2$, where x is the channel side length. When $x = 10$ nm and $a = 1$ nm, this ratio is 36%, but when x is reduced to 5 nm, the ratio rises to 64%.

2.1 Key length scales for nanofluidics

To understand the transitions between different transport phenomena that happen as the nanochannel confinement increases and conventional continuum physical models start to break down, we have to start with a brief survey of the

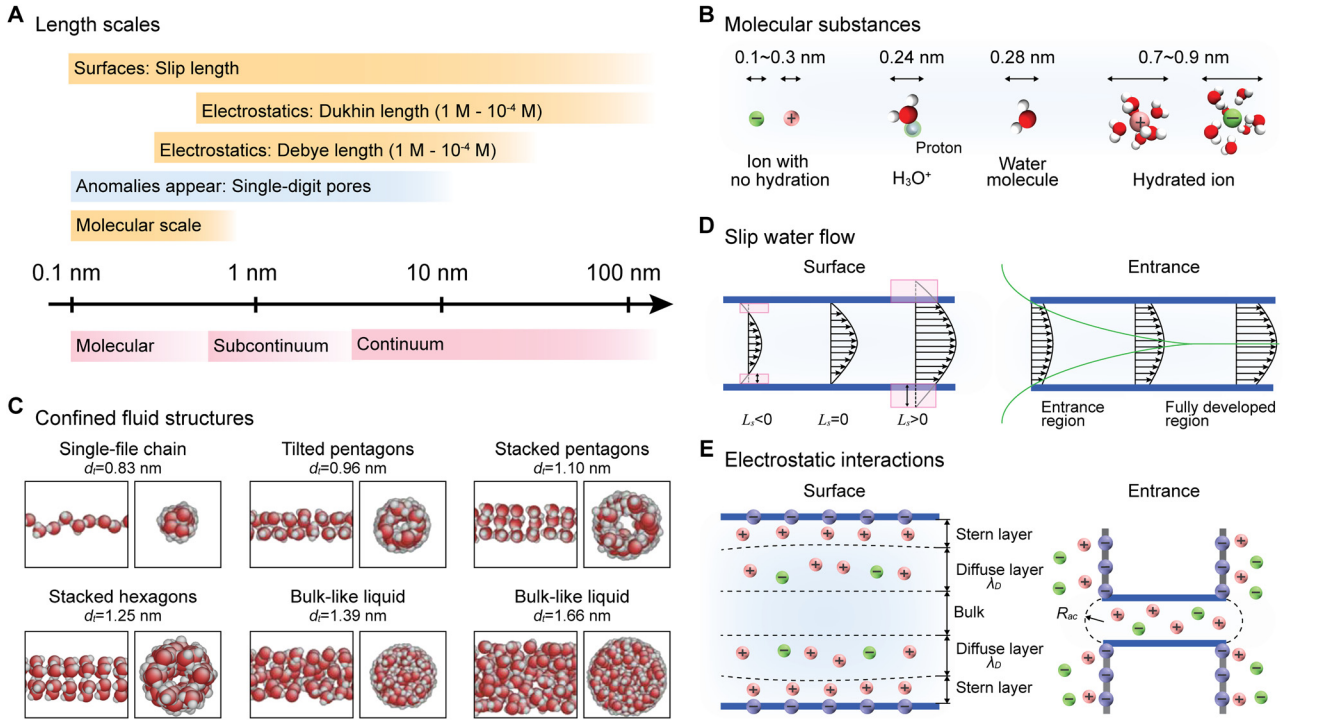

Fig. 2 Key length scales in CNT channels. (A) Key length scales governing flow in nanochannels. (B) Typical size distributions of species involved in nanofluidic transport. (C) Molecular dynamics snapshots showing water in CNTs of different diameters, illustrating confinement effects on the water structure. Reproduced from ref. 169 with permission from American Physical Society, copyright 2009. (D) Water slip in nanochannels. Left: Flow in an infinitely long channel with negative, zero, or positive slip lengths (L_s), where surfaces are dominant. Right: Flow entering a channel with a positive slip length, highlighting entrance effects. (E) Schematic of electrostatic interactions during ion transport. Left: Ion transport in a negatively charged channel, where an electric double layer (EDL) forms. Right: Ion transport in a channel with negatively charged external surfaces or entrances, highlighting entrance effects and access resistance (R_{ac}).

associated length scales (Fig. 2). Continuum flow models already start to break down even in single-digit nanopores, that is, nanopores that are less than 10 nm in diameter.[9,186] Under even tighter confinement of ~2 nm diameter, the channel is only a few water molecules wide and holds only one ion per 50 nm of length at physiological (150 mM) salt concentrations. In the case of even stronger sub-1 nm confinement, a 10 nm-long channel holds only ~30 water molecules arranged into a 1D chain.[4,64,80]

2.1.1 Molecular length scales. At the smallest scales, typically ranging from 0.1 to 0.3 nm for bare ions, protons, hydronium, and water molecules (Fig. 2B), the granularity of fluids and their components, such as solvents, ions, and dissolved species, becomes critical, and conventional fluid mechanics no longer applies.[187] The most pronounced deviations occur when only a single molecule can occupy a confined pore, leading to highly correlated and collective fluid dynamics known as single-file transport.[188] This mode of transport deviates significantly from bulk hydrodynamic predictions, giving rise to non-Fickian transport,[189,190] stochastic burst-like flow,[188] and rapid water and ion translocation.[64,69] Biological channels exploit a similar degree of confinement to achieve very high permeability and selectivity of AQPs,[191] extreme potassium ion selectivity of KcsA channels,[192] and high mechano-sensitivity of piezo channels.[193]

2.1.2 Limits of continuum hydrodynamics. The Navier–Stokes (NS) equation, developed over two centuries ago, remains highly effective for describing fluid flow even at very small scales. The breakdown of the NS equation occurs at a characteristic length scale, L_c, as suggested by Bocquet and Charlaix.[1] They proposed that this threshold is reached when the hydrodynamic timescale, defined by the fluid's kinematic viscosity, becomes comparable to the molecular timescale. This length scale, L_c, represents the lower limit at which fluid viscosity, η, can be defined. In macroscopic fluid mechanics, the kinematic viscosity $\nu = \eta/\rho$ (where ρ is the mass density) acts as a diffusion coefficient for fluid momentum. For this coefficient to remain valid, the time required for momentum to diffuse across a system, L_c^2/ν, must exceed the timescale of molecular motion, which is the fundamental driver of diffusion. At thermal agitation speeds of around 300 m s^{-1}, a water molecule travels a distance comparable to its own size in *ca.* $\tau_c = 10^{-12}$ s, defining the molecular timescale. The minimum system size at which viscosity remains meaningful can then be estimated as:

$$L_c = \sqrt{\nu\tau_c} \approx 1 \text{ nm} \quad (1)$$

Below this surprisingly low value, roughly corresponding to three water layers, subcontinuum phenomena, such as water structuring at surfaces, begin to dominate.[194–197] In CNTs,

water behaves somewhat similar to a bulk liquid for pore diameters greater than 1 nm (Fig. 2C).[64,169] However, below this limit, water molecules begin to organize into ordered structures, eventually forming single-file chains within sub-1 nm CNTs.[4,64,169] Similar semi-ordered arrangements have also been observed for water confined between two graphene sheets separated by less than a nanometer.[65,194]

2.1.3 Slip length scales. The NS equations require boundary conditions at the solid–liquid interface for modeling nanoscale fluid flows. At the macroscopic scale, researchers often assume a no-slip boundary condition that matches the fluid's tangential velocity at the solid surface to that of the solid. However, if those fluid and solid velocities differ, the fluid *slips* on the surface (Fig. 2D). The slip boundary condition is essential for capturing non-continuum flow behaviors in nanochannels while still using the continuum hydrodynamics formalism, where the slip length can serve as a measure of the interaction between water and channel surfaces.[6,60]

Slip length also quantifies the effective friction at the fluid–solid interface, with larger slip lengths indicating lower friction. In linear response theory, the friction force is proportional to the liquid's velocity. For a fluid moving in the x-direction with slip velocity v_x along a surface with normal z, the force balance per unit area is $\sigma_{xz} = \lambda v_x$, with σ_{xz} being the stress tensor and λ the friction coefficient (in N s m^{-3}). For a Newtonian fluid, $\sigma_{xz} = \eta \partial_z v_x$, where η is the fluid viscosity, allowing the Navier boundary condition to be rewritten as $v_x = L_s\left(\frac{\partial v_x}{\partial z}\right)$ where the slip length L_s is given by:

$$L_s = \frac{\eta}{\lambda} \tag{2}$$

Geometrically, the slip length represents the distance inside the solid where the extrapolated fluid velocity profile reaches zero. A no-slip condition corresponds to $\lambda \to \infty$ or $L_s \to 0$, when the velocity profile terminates (reaches zero) at the wall. A finite slip length ($L_s \neq 0$), which refers to partial slip condition, describes the situation when the flow velocity profile at the wall does not reach zero at the wall, and instead, if continued beyond the wall, would reach zero at the distance equal to the slip length. Experimental and theoretical studies reveal that the slip length of water on solid surfaces strongly depends on surface wettability and can range from nanometers to microns.[198–201] As we will discuss, large slip lengths indicating low friction at the wall in CNTs and other nanochannels are often linked to significant enhancements in water flow rates.[6,25,60]

2.1.4 Electrostatic length scales. Electrostatic interactions (Fig. 2E) are another major force in nanofluidics, governing interactions between charged species, such as ions dissolved in the fluid and surface charges. Additionally, the dipolar nature of water molecules and hydrogen bonding between them also play a critical role. Length scales associated with electrostatics and surface charge can extend to several tens of nanometers.[1,3,202] Electrostatic length scales are central to key nanofluidic phenomena such as ion selectivity and ion current rectification.[18,48,51,203]

2.1.4.1 Bjerrum length. The Bjerrum length, L_B, represents the distance at which the electrostatic interaction between two charged species becomes comparable to the thermal energy, k_BT. For two ions with valence z_i, in a dielectric medium, the Bjerrum length is given by:

$$L_B = \frac{z_i^2 e^2}{4\pi\varepsilon k_B T} \tag{3}$$

where e is the elementary charge and ε is the dielectric constant. By definition, the Bjerrum length is the distance below which electrostatic interactions dominate over thermal fluctuations.[204] As a result, its impact on nanofluidic transport is most significant at the molecular scale. For instance, in bulk water with monovalent ions ($z_i = 1$), the Bjerrum length is $L_B \approx 0.7$ nm, which closely aligns with the molecular length scale. In confinements smaller than L_B, removing an ion from its hydration shell and introducing it into a molecular-sized pore incurs a high free-energy cost. The long-range nature of electrostatic interactions also means that the effects of the Bjerrum length extend to larger scales. For instance, in media with lower dielectric constants, L_B can be much larger, leading to the formation of long-lived ion pairs.[204]

2.1.4.2 Debye length. The Debye length is a key concept in electrostatics that is critical for understanding the electric double layers (EDLs) that form to screen charged surfaces (Fig. 2E). Debye length characterizes the thickness of the EDL and is independent of surface charge. It is expressed as:

$$\lambda_D = \sqrt{\frac{\varepsilon\varepsilon_0 k_B T}{e^2 N_A \sum_i z_i^2 C_i}} \tag{4}$$

where ε is the dielectric constant of the medium, ε_0 is the permittivity of free space, k_B is the Boltzmann constant, T is the absolute temperature in Kelvin, e is the elementary charge, N_A is Avogadro's number, z_i is the valence of ion i, and C_i is the molar concentration of ion i. Physically, the electrostatic free energy of an ion surrounded by its spherical cloud of counterions with radius λ_D is on the order of k_BT. Debye length depends on ion concentration and can range from several nanometers to sub-nanometer scales. For instance, for KCl solutions, the Debye length decreases from 30 nm at a salt concentration of $C_0 = 10^{-4}$ M to 0.3 nm at $C_0 = 1$ M. When EDLs overlap in channels, fluid transport can be strongly influenced, resulting in phenomena such as surface-dominated ion transport.[205,206]

2.1.4.3 Gouy–Chapman length. If the Debye length represents the interactions of the ions in the solution, another key length scale, the Gouy–Chapman length, L_{GC}, emerges when we consider the behavior of salt solution near a charged surface. L_{GC} represents the distance from the charged wall at which the electrostatic interaction between a single ion and the wall becomes comparable to k_BT. It is defined by the surface charge

density σ, and is given by:

$$L_{GC} = \left(\frac{2\pi\sigma L_B}{e}\right)^{-1} \quad (5)$$

Unlike the Debye length, the Gouy–Chapman length explicitly depends on the surface charge density σ of the confining surface (in C m^{-2}), and does not rely on the bulk ion concentration. For typical surface charge densities, such as $\sigma \approx 50$ mC m^{-2} ($\approx 0.3e$ nm^{-2}), $L_{GC} \approx 1$ nm. This length scale becomes particularly relevant in solutions with very low salt concentrations, where it can significantly influence ionic conductance.

2.1.4.4 Dukhin length. The Dukhin length (L_{Du}) characterizes the relative importance of surface *versus* bulk conduction,[206,207] and can be rewritten as $L_{Du} \approx \frac{\kappa_{surf}}{\kappa_b}$, where κ_{surf} is the surface conductivity and κ_b is the bulk conductivity.[208] The Dukhin length is defined as:

$$L_{Du} = \frac{|\sigma|}{eN_A C_0} \quad (6)$$

For instance, with a surface charge density $\sigma \approx 50$ mC m^{-2} ($\approx 0.3e$ nm^{-2}), L_{Du} is ~ 0.5 nm when $C_0 = 1$ M. However, for very dilute concentrations such as $C_0 = 10^{-4}$ M, L_{Du} increases dramatically to ~ 5 μm.

2.1.4.5 Ion–ion interaction length. In bulk water, ions interact *via* a Coulomb potential $\phi(r) = \frac{e}{4\pi\varepsilon_0\varepsilon_w r}$, where ε_w is the dielectric permittivity of water. However, inside nanochannels, ions are no longer surrounded by a uniform fluid, and their interaction potential is influenced by the dielectric properties of the surrounding medium. This phenomenon was first noted decades ago for ions crossing lipid bilayers and has since become a common consideration in biological ion channel studies.[209] For a simple 1D channel of infinite length and diameter d, filled with water (with isotropic permittivity ε_w), and surrounded by a medium with permittivity ε_s (typically, $\varepsilon_s \ll \varepsilon_w$), ions would experience a stronger Coulomb potential as the channel size shrinks. For instance, in a system where a low-dielectric medium ($\varepsilon_s \sim 2$) confines a water-filled channel ($\varepsilon_w \sim 80$), the interaction energy of monovalent ions exceeds the thermal energy (k_BT) for channels smaller than $d \sim 15$ nm, while the Bjerrum length L_B is ~ 0.7 nm. These stronger Coulomb interactions would result in enhanced ion correlation effects. For example, Bocquet and co-workers predicted that the enhanced formation of Bjerrum ion pairs in the strong 1D confinement would lead to ionic Coulomb blockade.[210]

2.2 Channel length limitations

The length scales that we have discussed in the preceding sections define the physical mechanisms that make water and ions behave differently in nanofluidic channels. Those length scales also largely refer to the confinement *across* the channel. A related question is how far nanofluidic phenomena, such as the existence of the single-file water configuration and strong orientational order driven by hydrogen-bonding interactions between the water molecules and electrostatic interactions of the ions with water dipoles in narrow channels could extend in the third dimension, *i.e. along* the channel. Statistical mechanics tells us that such ordering cannot extend forever, and that at non-zero temperature in a long channel thermal fluctuations are bound to disrupt this order and eventually create defects. Such defects could, for example, interrupt the Grotthuss mechanism of fast proton transport[211] by creating domain boundary walls in the water chain. Thus, an effective "coherence" length, associated with these effects, would define the critical length scale at which clean nanofluidic phenomena can still be observed in such channels.

Köfinger *et al.* used a lattice dipole model to analyze the coherence effects in 1D water wires,[212] noting that emergence of such defects is largely governed by the energy of creating a defect in such water wires, E_D. Assuming these defects are uncorrelated, the associated "coherence" length is then determined by the number of molecules, N, in the water chain at which the probability of observing this defect ceases to become vanishingly small. In a simplified case, this probability is given by:

$$P \approx \left(1 + \exp\left(-\frac{E_D}{k_BT}\right)\right)^{-N} \quad (7)$$

The energy required to create such defects in a 1D water wire inside a sub-1 nm channel of a CNT is surprisingly high, $E_D \approx 8$ kcal mol^{-1} (13.4 k_BT),[212] leading to the astonishing prediction that water wires in CNTs and other 1D water channels should remain coherent over lengths up to 0.1 mm, and perhaps explaining experimental observations of fast proton transport in ultra-long CNTs.[121] This estimate also indicates that fast water transport in CNTs, discussed in detail in Section 6.2, is also expected to persist on the similar length scales.

The situation is quite different for the peculiar ion transport mechanism in sub-1 nm CNTs mediated by formation of ion-water clusters and partial de-wetting of the CNT pore.[69] A rough estimate of the limiting length scale for this mechanism can be obtained by considering that the energy of the formation of the ion–water cluster[68] needs to offset the energy penalty associated with expelling the rest of the water column from the CNT interior.[4] This estimate produces a value of ~ 25 nm, indicating that very fast electrophoretic ion transport is likely to be restricted to short CNTs and that ion conductance in longer CNTs could be governed by a different mechanism, perhaps supporting the mechanism of proton-mediated conductance proposed by Strano and co-workers for very long CNT channels.[121]

We also want to mention that strong confinement in CNTs should amplify the role of structural defects along the nanotube walls. As real-world nanotubes are never completely defect-free, the length scale defined by the average distance between such defects, could be one of the most important parameters that define the extent of pure nanofluidic behaviors in the CNTs. An early estimate[213] based on gas transport measurements[6] placed

this length at 160 nm for vertically-aligned double-walled CNTs grown on a substrate (other growth methods could produce even lower defect densities). Thus, it is reasonable to expect that transport phenomena in macroscopically-long CNTs could be significantly affected by structural defects, while shorter CNTs, such as CNT porins,[13] should be largely defect-free.

3 Carbon nanotubes

CNTs are nanocrystalline molecules composed of a hexagonal network of sp^2 hybridized carbon atoms rolled into cylindrical, one-dimensional structures (Fig. 3A). Depending on the number of coaxial layers, CNTs can be classified as single-walled (SWCNTs), double-walled (DWCNTs), or multiwalled (MWCNTs) (Fig. 3B), with diameters ranging from sub-nanometer to a few nanometers and lengths extending up to several millimeters. CNTs were first observed by Sumio Iijima in 1991 when he synthesized MWCNTs by arc discharge.[216] Later in 1993, Iijima *et al.*[217] and Bethune *et al.*[218] independently discovered SWCNTs. These carbon atom cylinders with internal cavities have since then become a truly iconic molecule of nanotechnology.[15,20,219–225]

CNTs are renowned for their exceptional strength, attributed to the uniform sp^2 bonds within their graphitic lattice.[226,227] While structural defects such as dangling bonds, carbon vacancies, sp^3 defects, and rotated bonds may occur, these are typically minimal.[228–230] CNTs boast an extraordinary length-to-diameter ratio, large surface area, and significant flexibility.[231–233] Their mechanical properties are equally

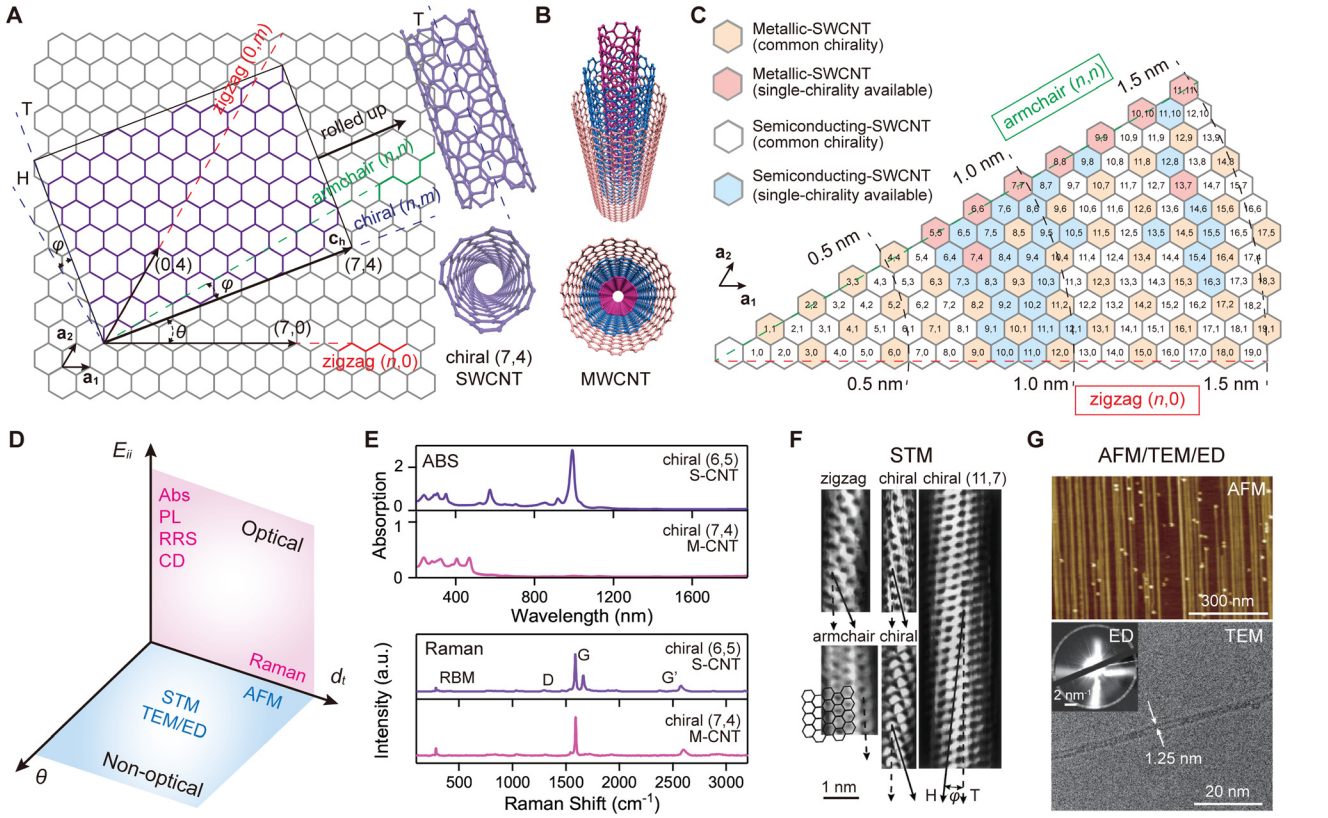

Fig. 3 Carbon nanotubes. (A) Schematic showing how a graphene sheet is rolled along the roll-up vector $\mathbf{c_h}$ to form a single-walled CNT (SWCNT), with the (7,4) CNT as an example. Wrapping vectors along the red or green dotted lines produce zigzag or armchair tubes, while other angles result in chiral tubes (*n*,*m*). The chiral angle θ is measured relative to the zigzag direction, and $\varphi = 30^\circ - \theta$ is measured relative to the armchair direction. The vector **T**, perpendicular to $\mathbf{c_h}$, defines the tube axis, and **H**, perpendicular to the armchair direction, specifies the nearest-neighbor hexagon rows. The angle between **T** and **H** is φ. (B) Multi-walled CNTs (MWCNTs). (C) SWCNT (*n*,*m*) nomenclature, showing examples of typical diameters. Common chiralities are synthesized using methods like CoMoCat and HiPCo, while single chiralities can be achieved through post-synthesis sorting with purity exceeding 99%. (D) Overview of (*n*,*m*) chirality assignments based on E_{ii}, d_t, and θ, determined using optical methods (*e.g.*, absorption (Abs), Raman, photoluminescence (PL), resonance Rayleigh scattering (RRS), and circular dichroism (CD)) and nonoptical methods (*e.g.*, scanning tunneling microscopy (STM), Atomic force microscopy (AFM), transmission electron microscopy (TEM), and electron diffraction (ED)). Adapted from ref. 21 with permission from American Chemical Society, copyright 2020. (E) Absorption spectra and Raman spectra of (6,5) and (7,4) SWCNTs. Adapted from ref. 176 with permission from Springer Nature Limited, copyright 2024. (F) Atomically resolved STM images of individual SWCNTs, showing the lattice structure on the tube surface for precise chirality identification. Dashed arrows represent the tube axis **T**, and solid arrows indicate the direction of nearest-neighbor hexagon rows **H**. Reproduced from ref. 214 with permission from Macmillan Magazines Ltd, copyright 1998. (G) AFM image of horizontal (12,6) SWCNTs arrays (top) and the corresponding TEM of an individual tube (bottom). Bottom inset: A typical ED pattern of a (12,6) CNT. Reproduced from ref. 215 with permission from Macmillan Publishers Limited, part of Springer Nature, copyright 2017.

impressive, with an average Young's modulus ranging from 0.3 to 1.5 TPa, along with bending and shear moduli of ~1 TPa and ~1 GPa, respectively;[232,233] these characteristics allow CNTs to bend, twist, kink, and buckle, yet return to their original shape, retaining their properties.[234,235] When compressed, CNTs can form kink-like structures that relax elastically once the stress is released.[236,237] These properties make CNTs promising candidates for use as fluidic channels and for incorporation into membrane structures.

Numerous review articles cover CNT synthesis, sorting, functionalization, characterization, and material properties,[21,177,238–245] as well as their applications[219,220,223–225,246,247] in areas such as chemical sensing, fluorescent probes, transparent conductive films, nanotube templates, and thermoelectric devices; therefore, we will focus only on those properties that influence nanofluidic transport.

3.1 Carbon nanotube chirality

CNT chirality is defined by its chiral vector $\mathbf{c_h}$ (Fig. 3A).[248–250] This vector, represented by the equation $\mathbf{c_h} = n\mathbf{a_1} + m\mathbf{a_2}$, where n and m are integers indicating the number of steps along the zig-zag carbon bonds, and $\mathbf{a_1}$ and $\mathbf{a_2}$ are the graphene lattice basis vectors in real space, fully describes CNT's geometry. The chiral vector forms an angle θ with the zig-zag direction (or $\mathbf{a_1}$), known as the chiral angle, which determines the degree of "twist" in the CNT. When the chiral angle is 0° or 30°, the CNT adopts a *zig-zag* or *armchair* configuration, respectively.[251] Any configuration where $0^\circ < \theta < 30^\circ$ is considered chiral, with atomic arrangements of the armchair and zig-zag CNTs being symmetrical relative to the tube axis. Unlike achiral species, each specific chiral nanotube has a symmetric mirror structure (different handedness) defined as its (m,n) enantiomer.

The carbon nucleus-to-nucleus diameter (d_t) and chiral angle (θ) of a SWCNT can be calculated as follows:

$$d_t = \mathbf{c_h}/\pi = a_{cc}\sqrt{3(m^2 + n^2 + nm)}/\pi \quad (8)$$

$$\theta = \tan^{-1}\left(\sqrt{3}m/(2n + m)\right) \quad (9)$$

where the distance between the nearest neighboring carbon atoms (a_{cc}) is 0.142 nm. For fluid transport, one can estimate the effective diameter of a CNT by subtracting the carbon atom diameter from the carbon nucleus-to-nucleus diameter. Over 160 possible chiralities can be derived for SWCNTs with diameters in the range of 0.4–2.2 nm, allowing for highly tunable cavities with diameter increments of about 0.01 nm between adjacent chiralities (Fig. 3C), thus far exceeding pore size precision achievable with biological channels or other materials.

3.2 Electronic properties

The properties of SWCNTs are intrinsically linked to their structures, as reflected in their density of states (DOS).[252,253] Even slight variations in atomic arrangement can significantly alter the bandgap structure, influencing their electrical properties.[254,255] SWCNTs can be either semiconducting or metallic, with their bandgaps determined by their chirality and charge carrier mobility.[214,250,256–260] Metallic SWCNTs (M-SWCNTs) have exceptional electrical conductivity,[225,261–263] while semiconducting SWCNTs (S-SWCNTs) have structure-dependent bandgaps and associated carrier mobilities.[20,239,244,264–270] The different electronic properties of S-SWCNTs and M-SWCNTs may have complex effects on nanofluidic transport, potentially due to liquid–electron coupling and polarization effects.[71,170,176,271]

The chiral indices (n,m) of a SWCNT can be used to determine whether it is semiconducting or metallic (Fig. 3C) with a simple equation[272] $|n - m| = 3q$. If q is an integer, the CNT is metallic with a continuous DOS at the Fermi energy; otherwise, it is semiconducting with chirality-dependent transition energies between van Hove singularities. Due to additional curvature effects, only armchair SWCNTs ($n = m$) are truly metallic, while other metallic SWCNTs ($n \neq m$) exhibit a chirality-dependent energy gap at low temperatures.[273] If all chiral species form with equal probability, a nonselective synthesis protocol should produce two-thirds semiconducting and only one-third metallic species.[274] DWCNTs are typically produced as a polydisperse mixture with varying diameters and electronic structures, further complicated by SWCNT contamination.[242] DWCNTs are more structurally stable than SWCNTs, with interlayer interactions minimally affecting their band structure, although the potential barrier depends on the chirality pairing. MWCNTs with small diameters (<10 nm) behave similarly to SWCNTs, with minimal interaction between adjacent shells.[275] However, for larger diameter MWCNTs, each individual tube exhibits a metallic nature.[276]

3.3 Synthesis, sorting, functionalization and characterization

3.3.1 CNT synthesis. CNTs are primarily synthesized using three methods: arc discharge, laser ablation, and chemical vapor deposition (CVD).[21,277–283] The earliest MWCNTs, produced by Sumio Iijima using the arc discharge method, were formed as bundles on the negative electrode in a helium atmosphere.[216] The first SWCNTs were also synthesized using this method with transition metal catalysts like Fe and Co.[217,218] A significant advancement came from the Smalley group who introduced laser ablation, where laser pulses were used to heat a Co–Ni/graphite target to 1200 °C, converting 70–90% of the graphite into SWCNTs.[284] Both arc discharge and laser ablation use high-temperature carbon vaporization, producing high-quality CNTs while also generating significant byproducts. The next major breakthrough was the development of CVD synthesis protocol that used hydrocarbon gases as the carbon source and Fe catalyst nanoparticles as growth seeds.[285–287] CVD gained wide adoption due to its ability to produce both isolated nanotubes and densely packed arrays.[284,288–295] Over the past three decades, researchers have shown that CVD can produce high-purity SWCNTs (over 90%) on an industrial scale.[20,287,296] The selective growth of chirally-pure SWCNTs, such as (6,5)/(7,5) enriched types, began in 2003[297] and has since led to various methods for producing pure semiconducting SWCNTs.[298–307] CVD protocols can also

be optimized to produce high-purity DWCNTs and MWCNTs.[308–310]

3.3.2 CNT sorting. Despite advances in structure-controlled synthesis, the purity and yield of as-grown CNTs still do not meet the purity requirements for nanofluidic transport experiments, requiring post-synthesis structure separation.[240,243] To date, researchers have been able to isolate ~40 types of enriched or high-purity (n,m) species and their enantiomers (Fig. 3C). Based on their conductivity and atomic structure, SWCNT separation can be categorized into three stages: metallic/semiconducting separation, chirality separation, and enantiomer separation.

Separation of SWCNTs into metallic and semiconducting fractions began in 2003. Krupke *et al.*[311] developed a dielectrophoresis method for isolating metallic SWCNTs, where CNTs with larger dipole moments moved quicker. In the same year, Strano *et al.*[312] used diazonium reagents to selectively react with metallic SWCNTs, thereby enriching semiconducting SWCNTs. However, these techniques lacked true chirality selectivity, limiting their practical use. In contrast, liquid-based separation methods, such as polymer wrapping, density gradient centrifugation (DGU),[313,314] ion-exchange chromatography (IEX),[315] gel chromatography,[316] and aqueous two-phase (ATP),[317] offer better prospects for SWCNT sorting. These techniques can not only separate metallic from semiconducting SWCNTs but also isolate single-chirality species and even their enantiomers using precise modulation of interactions between CNTs and polymers, DNA, or surfactants. These separation techniques have proven to be efficient and reliable pathways for producing large quantities of chirally-pure SWCNT.

3.3.3 CNT functionalization. The high stability of the graphitic carbon structure of CNTs poses challenges for their chemical functionalization.[318] Researchers typically use the covalent functionalization strategy to place chemical groups at the CNT entrances. These approaches often involve oxidation agents such as nitric acid, oxygen, concentrated sulfuric acid, or aqueous hydrogen peroxide.[319] Plasma oxidation (using oxygen, air, or water plasmas) is also commonly used to open sealed CNTs to fluid flow. These approaches introduce oxygen-containing groups (*e.g.*, carboxy and hydroxy) at CNT ends and sometimes on the sidewalls. These functional groups can then be further modified[320–324] to attach alkane chains,[325] polypeptides,[325] highly charged dye molecules,[326–328] large biomolecules,[5,329,330] zwitterions,[79] and methacrylic acids[331] to the CNT entrance.

CNT sidewalls are typically modified with non-covalent functionalization, primarily using π-stacking that does not disrupt the sp^2 lattice of CNTs.[332] Non-covalent attachments take advantage of adsorption of traditional surfactants such as sodium dodecyl sulfate (SDS),[333,334] surfactant-like amphiphilic biopolymers such as DNA and RNA oligonucleotides,[335] peptides,[336–339] and polycyclic aryl complexes with hydrophilic appendages like proteins and polymers.[340–343] These modification strategies allow CNTs to retain their aromatic structure and electronic properties and are often used to solubilize CNTs.

3.3.4 CNT characterization. The distinct electronic structure of CNTs directly influences their optical, electrical, and optoelectronic properties (Fig. 3D). Optical methods, such as Raman spectroscopy, absorption, photoluminescence (PL), X-ray scattering, neutron scattering, resonant Rayleigh scattering (RRS), nuclear magnetic resonance (NMR), and circular dichroism (CD) spectroscopy, assign chiralities and diameters (d_t) to the CNTs based on the transition energies between the van Hove singularities (E_{ii}).[272,344] For instance, SWCNTs exhibit distinct Raman bands that can be used to distinguish metallic and semiconducting CNTs, identify defects and assess CNT quality, as well as determine CNT diameter from the position of its Radial breathing mode (RBM) peak[176] (Fig. 3E). Non-optical methods can identify the chiral indices (n,m) using diameter (d_t) and chiral angle (θ) information obtained from techniques such as scanning tunneling microscopy (STM), atomic force microscopy (AFM) or transmission electron microscopy (TEM) combined with electron diffraction (ED)[214,215,250,345–351] (Fig. 3F and G).

We note that some of these optical and non-optical approaches can also be used to investigate water filling in CNTs. Electron microscopy[129,352,353] has been utilized to probe water filling in CNTs. Optical methods such as X-ray scattering,[354–356] neutron scattering,[357,358] NMR,[111,359–362] IR spectroscopy,[363] PL spectra,[364] and Raman spectroscopy[107,110,365–370] provide both water filling and structural information inside CNTs.

4 Carbon nanotube nanofluidics: the early days

Experimental studies of fluid transport in CNTs encountered two early challenges: opening CNTs and filling them.[373–379] Most synthetic protocols produce closed CNTs, and researchers introduced plasma etching processes to open them.[373,374,377,378] However, filling CNTs turned out to be much more complex and CNTs were initially considered as candidate "molecular straws" capable of absorbing molecules from liquids or gases rather than true fluidic channels.[376] Early studies showed capillary filling with liquid metals[373,374] and molten inorganic compounds.[379] Notably, the hydrophobic nature of CNT walls led to a widespread consensus that capillary filling of CNTs with water or ions was highly unlikely.

This consensus collapsed in 2001 when Hummer *et al.*[4] used MD simulations to show that water could spontaneously fill the ~0.8 nm diameter CNT (6,6) (Fig. 4). Strikingly, the water molecules formed a single-file chain in the nanotube cavity resulting in burst-like water conduction with astonishingly fast rates that exceeded those even of AQPs! In the same year, Gogotsi *et al.*[353] conducted an *in situ* TEM study showing excellent wettability of ~100 nm diameter CNTs and providing the first high-resolution TEM images of a water-carbon nanotube interface. Further research by Gogotsi and colleagues[129] in 2004 showed that water could fill ~2–5 nm diameter CNTs through sidewall defects and remain trapped even under TEM vacuum conditions. Complementing these findings, Zanotti

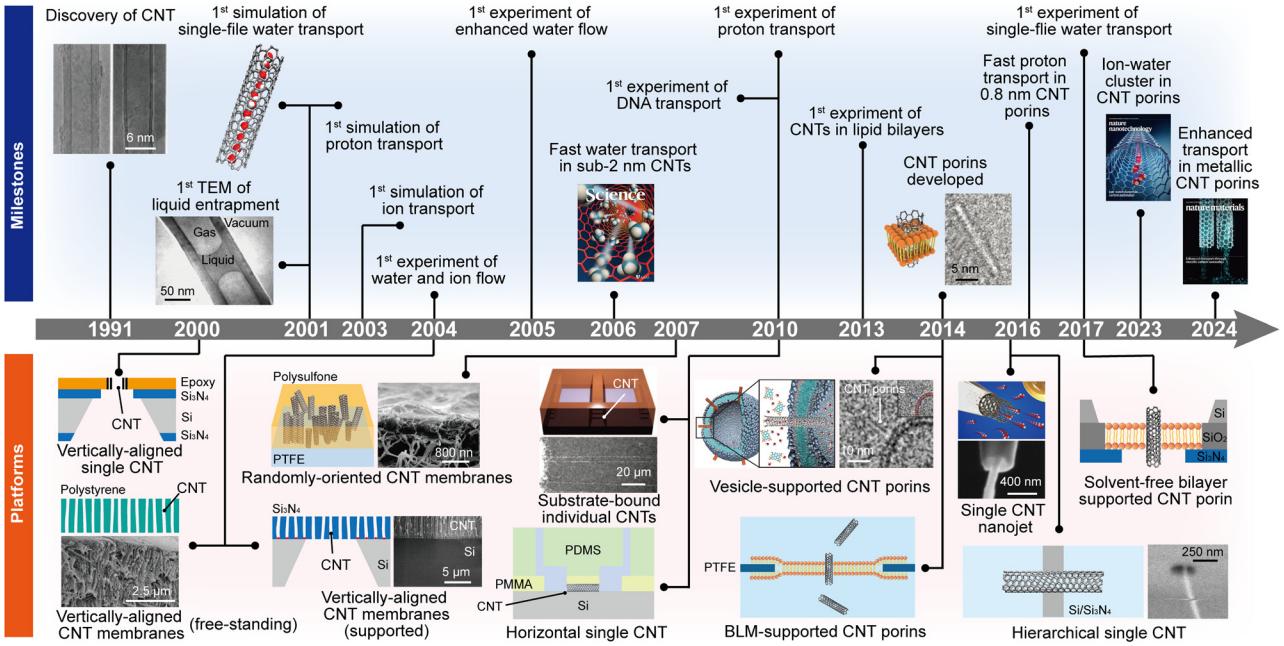

Fig. 4 Timeline of advancements in CNT nanofluidics. This timeline highlights over 20 years of progress in water, ion, and proton transport research, as well as the development of experimental platforms. The schematic diagrams and images include: TEM images of first discovered CNTs, reproduced from ref. 216 with permission from Springer Nature Limited, copyright 1991; TEM image of liquid entrapment in the CNT, reproduced from ref. 353 with permission from AIP Publishing, copyright 2001; journal cover image illustrating fast water transport in sub-2 nm CNTs, reproduced from ref. 6 with permission from the American Association for the Advancement of Science, copyright 2006; development of CNT porins, reproduced from ref. 13 with permission from Springer Nature Limited, copyright 2014; journal cover image depicting ion-water clusters in CNT porins, reproduced from ref. 69 with permission from Springer Nature Limited, copyright 2022; journal cover image illustrating enhanced transport in metallic CNT porins, reproduced from ref. 176 with permission from Springer Nature Limited, copyright 2024; vertically aligned single CNT platforms, adapted from ref. 371 with permission from American Chemical Society, copyright 2000; vertically aligned free-standing CNT membranes, adapted from ref. 5 with permission from the American Association for the Advancement of Science, copyright 2004; vertically aligned supported CNT membranes, adapted from ref. 6 with permission from the American Association for the Advancement of Science, copyright 2006; randomly oriented CNT membranes, adapted from ref. 372 with permission from American Chemical Society, copyright 2007; substrate-bound individual CNTs, reproduced from ref. 121 with permission from the American Association for the Advancement of Science, copyright 2010; horizontal single CNT, adapted from ref. 122 with permission from American Association for the Advancement of Science, copyright 2010; vesicle-supported CNT porins, with the cartoon reproduced from ref. 64 with permission from the American Association for the Advancement of Science, copyright 2017, and the cryo-TEM image reproduced from ref. 13 with permission from Springer Nature Limited, copyright 2014; BLM-supported CNT porins, adapted from ref. 69 with permission from Springer Nature Limited, copyright 2022; single CNT nanojets, adapted from ref. 25 with permission from Macmillan Publishers Limited, part of Springer Nature, copyright 2016; hierarchical single CNT structures, adapted from ref. 126 with permission from Springer Nature Limited, copyright 2020; and solvent-free bilayer supported CNT porins, adapted from ref. 69 with permission from Springer Nature Limited, copyright 2022.

et al.[358] and Mamontov *et al.*[380] observed ice-shell and water-chain structures along with phase transitions in 1.4–1.6 nm diameter CNTs with neutron scattering techniques. In 2010, the first experimental demonstration of single-file water structure in CNTs was achieved by monitoring radial breathing modes (RBM) in Raman spectra.[110] These results demonstrated that water indeed spontaneously enters CNTs with diameters of 0.55 nm or larger. Collectively, these studies opened up the possibility of using CNTs as nanofluidic channels.

Crooks and colleagues conducted initial investigations of mass transport in CNTs starting in 2000.[371,381,382] They indirectly quantified hydrodynamic and electrophoretic flow in individual extremely large (~60–160 nm diameter) CNTs using polystyrene particles as probes in a vertically-aligned single CNT platform. The key breakthroughs however came from the experimental studies that aimed to explore water transport in smaller diameter CNTs following Hummer's simulation. The pioneering demonstration of nanofluidic transport in CNT channels was achieved in 2004 by Hinds *et al.*,[5] who reported gas and ion transport through free standing vertically-aligned membranes composed of ~4 nm diameter CNTs embedded in a polymer matrix. The following year, Majumder *et al.*[60] reported fast water flow through ~7 nm diameter CNTs using the same polymer-filled CNT membrane. Their findings indicated flow rates 4–5 orders of magnitude faster than those predicted by classical hydrodynamics, suggesting astonishingly large slip lengths of 3–70 μm. In 2006, Holt *et al.*[6] further reported exceptionally rapid water and gas transport through sub-2 nm diameter CNTs embedded in a ceramic Si_3N_4 matrix, cementing the concept of enhanced water flow in CNTs. The next breakthrough came in 2010, when several groups introduced experimental platforms for measuring transport through individual CNT channels.[25,64,80,114,119,134,176]

The study of ion transport in CNTs paralleled these advancements in water transport measurements. Pioneering MD simulations on ion transport in CNTs were conducted by

Aluru *et al.*[156,165] in 2003. They predicted that ions could be transported through ~2–6 nm diameter CNTs under external electric fields and that ion selectivity could be modulated by surface charges on the CNT walls or by functional groups located at the nanotube entrances. Hinds and co-workers achieved the initial experimental observation of ion transport through CNT pores in their seminal work on CNT membranes,[5] where they observed the diffusion of $Ru(NH_3)_6^{3+}$ ions across the membrane. Subsequent research led by Bakajin and Noy[115] in 2008 highlighted the capabilities of CNT membranes in ion transport and the selective rejection of different salt ions, regulated by charged carboxylate (COO^-) groups at CNT entrances. After single CNT transport measurement platforms were developed, researchers determined single CNT conductance and investigated conductance scaling and enhancement behaviors. For example, Liu *et al.*[122] reported the first ion transport measurements in individual 1–2 nm diameter CNTs under external voltage in 2010 and reported electrophoretic transport of short single-stranded DNA oligomers through these CNTs. They also reported ion conductance scaling and some evidence of metallicity dependence on CNT transport, but small number of samples investigated and associated fabrication and characterization difficulties precluded truly reliable observations.

The initial studies on proton transport in CNTs began in 2003 with molecular dynamics (MD) and *ab initio* MD (AIMD) simulations conducted by Dellago *et al.*,[383] Zhu *et al.*,[384] and Mann *et al.*;[385] all of them predicted enhanced proton mobility inside CNTs compared to bulk water due to spatial confinement stabilizing the hydrogen-bonded water chains and promoting the Grotthuss transport mechanism. In 2010, Lee *et al.*[121] provided early experimental evidence of high proton mobility in 1.3–2.3 nm diameter micron-long CNTs. Subsequent experiments in 2016 on ~0.8 nm diameter CNT porins by Tunuguntla *et al.*[180] provided the definitive evidence of enhanced proton transport facilitated by single-file water chains in the narrow CNTs.

5 Platforms for studying CNT transport

5.1 Experimental platforms

Since the earliest studies of CNT nanofluidics,[371] experimental platforms (Fig. 4 and Table S1, ESI†) have been a critical component to advancing the field. Aligned CNT membranes enabled the first demonstrations of enhanced transport in CNTs.[5,6,60] Researchers used these micron-long CNT pore arrays to study pressure-driven water flow and ion conductance. However, several drawbacks quickly emerged. These key concerns include the purity and polydispersity of CNT membranes, which contained mixed CNT chiralities and diameters, the presence of sidewall defects and bends in the CNT comprising the array, and general reproducibility and yield of the fabrication process.[324] Determining and controlling the CNT diameters relevant for transport was also a key challenge for the aligned CNT membrane platform.

To overcome these drawbacks, researchers also developed single CNT based platforms.[121,122,222] Transport measurements on individual CNTs can reveal detailed structure–property correlations, avoid complications from pore size diversity and enable quantitative interpretations of transport efficiency. They, in principle, should also allow investigation of the impact of CNT metallicity on fluid transport.[122,176] Subsequently, Noy and co-workers developed a biomimetic CNT transport measurement platform, CNT porin,[13,179] which combines some of the advantages of the two previous approaches.

5.1.1 CNT membranes. Membrane fabrication typically begins with the CVD growth of a CNT forest on a silicon or quartz support. The forest is then infiltrated with an impermeable matrix *via* a liquid-phase or vapor-phase process, with the latter better preserving CNT alignment. Excess matrix material, support, and catalyst particles are then etched away or polished off to open the CNT ends. Afterwards, gas permeance and size exclusion tests are used to confirm that fluid flows through the CNTs and not through the defects in the matrix.[386]

5.1.1.1 Free-standing vertically aligned CNT membranes. The Hinds group first demonstrated the fabrication of free-standing, vertically aligned CNT membranes.[5,60,125] They grew arrays of CNTs (~7 nm in diameter) on silicon dioxide (SiO_2) substrates using CVD. These CNT arrays were then infiltrated with a polystyrene (PS) solution producing a 5–10 μm thick, free-standing, rigid CNT–PS film. Residual PS, catalyst particles, and capped CNTs were subsequently removed by water plasma oxidation, yielding vertically aligned CNT membranes with a density of 6×10^{10} tubes per cm^2. Building on Hinds' approach, researchers explored various methods to improve membrane integrity, tube density, and overall area, focusing primarily on changing the catalyst in CVD growth, replacing matrix materials, and optimizing the matrix infiltration process.[109,139,142,283,386–390] Currently, the most effective strategy involves growing CNT forests on silicon wafers using Fe/Mo/Al_2O_3 multilayer catalysts, using low C_2H_2 flux to facilitate the formation of very small, densely packed CNTs, which are then infiltrated by parylene-N to produce wafer-scale CNT membranes containing ultrahigh densities (up to $\sim 10^{12}$ tubes per cm^2) of CNTs smaller than 2 nm in diameter.[109,386,388–390]

An alternative fabrication route involves orienting CNTs in a polymerizable dispersion with an external field, then solidifying the matrix to preserve their alignment. This *postgrowth* alignment approach[24,143,391–393] can accommodate CNTs of different diameters and provides access to various polymeric matrices, although it typically produces membranes with 1–2 orders of magnitude lower pore density (10^{9-10} tubes per cm^2) than CVD-growth based protocols. Recently, Shan's group[24,143,392,393] reported a scalable technique that employs combined AC and DC electric fields to align CNTs (0.8–100 nm in diameter and 2–100 μm in length) at densities of up to 10^{10} tubes per cm^2.

5.1.1.2 Supported vertically aligned CNT membranes. The Bakajin group[6,115,117,394] developed vertically aligned CNT membranes on silicon substrates. They synthesized dense

CNT arrays with 1–2 nm diameters and 2–3 μm thickness using catalytic CVD, infiltrated them with Si_3N_4, and opened the CNTs *via* plasma etching. This approach was later adapted by Krishnakumar *et al.*,[395] who coated 7 nm-diameter, 40 μm-long CNTs with vapor-deposited parylene, and by Lokesh *et al.*,[124] who infiltrated CNT arrays with TiO_2. These membranes were thin, mechanically robust (withstanding >1 atm pressure), and achieved high CNT densities of up to $\sim 2.5 \times 10^{11}$ tubes per cm^2. However, a key limitation was the small active membrane area on the silicon support.

5.1.1.3 Randomly-oriented macroscopic CNT membranes. Researchers also introduced a hybrid CNT platform incorporating semi-aligned or randomly dispersed CNTs into polymer matrices[372,396,397] that featured randomly oriented CNTs partially protruding from the membrane. These platforms stand out due to their simplicity and scalability, enabling the production of large-scale membranes (~ 20 cm $\times$ 20 cm) with a density of $\sim 7.5 \times 10^{10}$ tubes per cm^2. Microtomed membranes, developed by the Hinds group[141,327,398] allowed researchers to use CNTs with a wide size range, but those membranes suffered from very low active open areas, which limited their use.

5.1.2 Single CNT platforms. Various approaches have demonstrated nanofluidic platforms where a single isolated CNT serves as the transport pathway across an impermeable matrix. The first platform based on an individual, isolated CNT was developed by Crooks and colleagues[371,381,382,399] who microtomed an epoxy block embedded with a CNT into 1 μm-thick membranes with a single embedded 60–160 nm diameter CNT (this approach was limited to CNTs larger than ~ 50 nm in diameter).

In 2010, Lindsay and Strano groups reported platforms that used single long CNTs spanning a barrier between two microfabricated reservoirs,[121,122,132,137,400] which allowed them to perform a series of transport measurements involving the translocation of ions, protons and DNA through these channels.[121,122] Subsequent variants of this platform incorporated modifications, such as different CNT dimensions, CNT numbers, resist materials, or the addition of gate electrodes.[74,79,108,114,134,146,401,402]

Bocquet and co-workers introduced a distinctly different and elegant approach with the introduction of the single-CNT nanojet platform[25] and the hierarchical single-CNT platform[26,126,136] in 2016. The nanojet platform enabled water transport measurements by extracting a single CNT from a CNT forest and maneuvering it into the orifice of a glass nanocapillary or a Si_3N_4 membrane and then sealing it with an electron beam-induced deposition. Both approaches required precise CNT handling inside an operating scanning electron microscope (SEM), which limited the types and sizes of usable CNTs to MWCNTs with diameters larger than ~ 4 nm.[126]

5.1.3 Carbon nanotube porins. The platforms that we have described in the previous paragraphs enabled a number of key early discoveries in nanofluidics; however they still presented a number of challenges that ranged from complicated fabrication and low yields, to uncertainties associated with the presence of defects, to inability to access sub-1 nm CNT size regimes, or to reliably probe CNTs with defined chirality. Further progress required an experimental platform that was easy and facile, flexible enough to address a range of sizes and chiralities, and that allowed a number of different transport measurements.

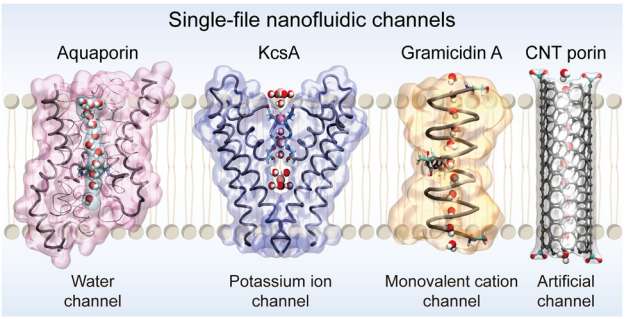

Fig. 5 Schematic illustration of selected biological membrane channels (AQPs, KcsA, and gramicidin A) and CNT porins embedded in lipid bilayers. Key selectivity filter groups are shown in licorice representation. Protein structures were obtained from the Protein Data Bank,[403] and rendered using VMD.[404]

Highly efficient biological membrane channels (Fig. 5), with their sophisticated transport characteristics, serve as benchmarks for the structure and transport performance of artificial channels.[46,86,87,106,405,406] Among these, AQPs,[90,191,407,408] are particularly notable for their exceptional water permeability combined with near-perfect selectivity including effective proton exclusion. The remarkable performance of AQPs arises from their hydrophobic interior, a narrow constriction zone, inward-facing carbonyl groups, and a precise arrangement of amino acid residues near the constriction. Beyond AQPs, other biological channels such as the KcsA potassium channel and gramicidin A (gA) have also inspired the design of synthetic membrane systems. KcsA conducts K^+ ions across membranes with exceptional selectivity and efficiency, facilitated by a highly conserved selectivity filter that ensures size- and charge-specific ion coordination *via* hydration-mediated binding and ion–ion Coulomb knock-on mechanisms.[409–411] Gramicidin A forms a β-helical, water-filled pore through dimerization of two subunits within lipid bilayers.[412–417] Its narrow, peptide-lined channel supports single-file water transport and also exhibits selectivity for certain monovalent cations and protons.

These natural systems have inspired the development of artificial channels that emulate key structural and functional features of their biological counterparts. Common design elements include the ability to self-assemble within membrane matrices for proper alignment, a cylindrical architecture that creates a continuous yet molecularly-confined pore enabling single-file transport, and strategically positioned functional groups at the channel entrance and interior surface. CNTs embody many of these characteristics, making them ideal candidates for artificial analogues. Such a platform was realized when Noy[13,179] and Wu[123,178] groups introduced *carbon nanotube porins* (CNTPs), a biomimetic CNT membrane

platform based on ultrashort (~5–15 nm), narrow diameter (sub-2 nm) CNTs embedded in a lipid bilayer.

Simulations predicted that short CNTs could penetrate lipid membranes,[418–427] a capability demonstrated experimentally with CNTs piercing cell walls.[428,429] In 2013, Wu *et al.*[123,133] took it one step further by showing that a microinjector can force very short CNTs to insert into lipid bilayers. However, this microinjection-based approach was not facile and the acid-cut CNTs[178,430] used for these experiments had a high number of defects, as indicated by a low ratio of the graphitic (G) to defect (D) Raman bands.

A significant step forward came in 2014, when the Noy group reported ultrashort CNTs stabilized with a phospholipid coating that could self-insert into a lipid membrane.[13,179,431,432] Subsequently, they extended this approach to polymer membranes[433] or peptoid nanosheets,[434] and showed that lipid coating can be replaced by surfactants without significant loss of functionality.[435] The sonication-assisted cutting used for this protocol also preserved the CNT quality and minimized damage to the CNT walls as evidenced by a high G/D ratio. This approach could use CNT stocks with different diameters and chiralities, producing CNT porins of varying metallicities, thereby enabling investigations into the impact of CNT electronic properties (metallic or semiconducting) on nanofluidics.[176] Geng *et al.*[13] demonstrated DNA translocation through ~1.5 nm diameter CNT porins, confirming that CNT porins formed well-defined transmembrane channels. They also showed that CNT porins can spontaneously incorporate into live cell membranes.[13] In a significant step, this team developed CNT porins with a diameter of ~0.8 nm, enabling the first study of water, proton, and ion transport in the all-important single-file regime and direct comparisons of transport efficiency between CNTs of different sizes.[64,180] Ion selectivity and pH-dependent transport measurements indicated the presence of negatively charged COO^- groups at the entrance of these CNT porins.[64,145,436] In addition to their nanofluidic properties, CNT porins have demonstrated capabilities as electron conductors for controlling redox reactions,[437] proton conductors for pH sensors,[438,439] ion conductors for liver cell channelopathies,[440] water conduits for desalination,[441] and even as fusion peptide mimetics that facilitated drug or probe delivery through membranes.[442–444] More recently, the same team expanded the nanotube porin family by demonstrating the synthesis of boron nitride nanotube (BNNT) porins, their incorporation into lipid membranes, and their use for osmotic energy harvesting.[445]

The key advantage of the CNT porin platform, stemming from its resemblance to a membrane protein, is its ability to adapt to most of the biophysical measurement protocols developed for quantifying transport in membrane channels. CNT porins can be incorporated in the walls of lipid vesicles and used for bulk-scale transport assay to measure water flow and ion diffusion.[64,69,80,81,119,176,180] At the same time, CNT porins are well-suited to single channel scale measurements in the planar lipid bilayer (BLM) and droplet interface bilayer (DIB) platforms which can quantify ion and proton electromigration.[13,69,176] The size and membrane configuration of CNT porins embedded in bilayers can be characterized by small-angle X-ray scattering (SAXS) and cryo-TEM.[13,119,180,356] To determine the average number of CNT porins in a vesicle (a number required for calculating single channel permeability values) researchers also introduced approaches based on labeling CNT ends with fluorescent nanoparticles, which are subsequently quantified using a combination of optical spectroscopy and cryo-EM,[180] or Oregon Green dye molecules that were then quantified with fluorescence correlation spectroscopy (FCS).[80,176]

Notably, the BLM and DIB approaches that measure ion electromigration through individual CNT porins[13,69,176,446] obviate the need to quantify the nanotube loading in the lipid bilayer. In addition to using common biological protocols for these measurements Noy and Wanunu also developed a modified planar lipid bilayer setup[64,145] based on a small (~100 nm diameter) nanopore etched in a thin Si_3N_4 membrane, which provides a clean hydrophilic surface for fusing lipid vesicles containing CNT porins. This solvent-free bilayer-supported CNT platform offers several advantages over traditional planar lipid membrane setups, including precise control over the number of CNT porins in the small bilayer patch and reduction in bilayer undulations and associated capacitive noise.

5.2 Computational tools

Since the pioneering MD simulation by Hummer *et al.* that launched CNT nanofluidics,[4] modeling and simulation have played a pivotal role in advancing this field.[4,147,383–385,448] Researchers used MD simulations to investigate the transport of water, ions, and protons in CNTs, shedding light on their structure, phase transitions, and transport dynamics.[147] With the progress of experimental techniques for CNT nanofluidics, computer simulations also played a critical role in interpreting the observed transport phenomena and revealing underlying mechanisms.[69,80,145,176]

Several computational tools are available for studying nanofluidics in CNTs, each offering unique insights at different length and time scales (Fig. 6A). The primary methods include quantum simulations, force-field-based MD simulations, and continuum modeling. Multiscale methods[69,449,450] have also been developed to bridge the gaps between different system sizes and timescales.

5.2.1 Quantum methods

5.2.1.1 Density functional theory. Density functional theory (DFT) is a widely used quantum method based on solving the Schrödinger equation using the Born–Oppenheimer approximation, where the nuclei are treated as fixed, and their interactions are modeled as an external potential. In DFT, the interaction energies are calculated by accounting for the electronic structure of CNTs and fluid molecules, which is highly accurate for modeling CNT nanofluidics.[80,161,451–456] For example, Lu *et al.*[453] applied DFT to calculate the electronic properties and dielectric behavior of finite-length CNTs in order to develop a CNT–water empirical model. They showed that atomic partial charges at CNT entrances primarily govern the

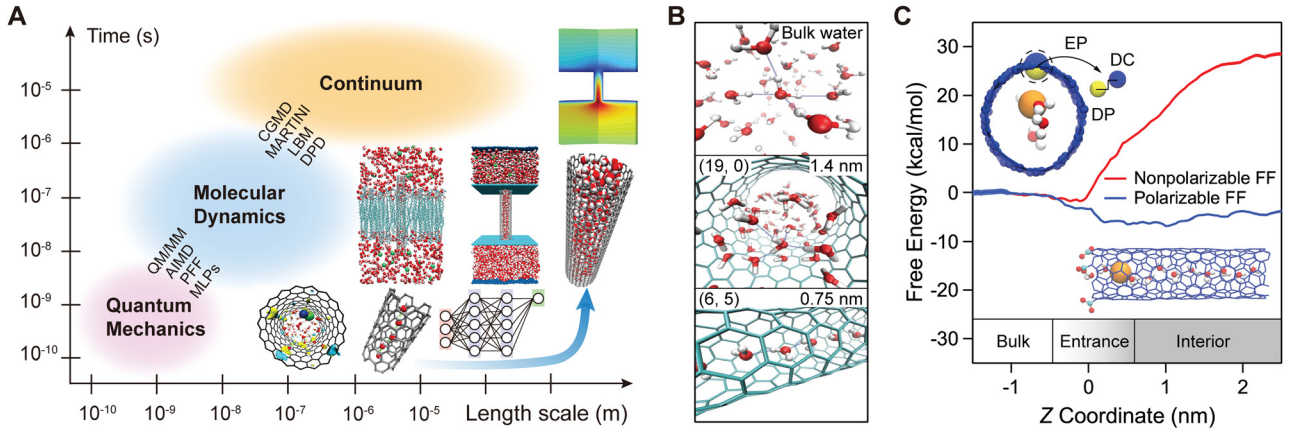

Fig. 6 Computational modeling of nanofluidic transport in CNTs. (A) Overview of computational modeling approaches categorized by their applicable length and time scales. Bridging methods, such as QM/MM (quantum mechanics/molecular mechanics), AIMD (*ab initio* molecular dynamics), PFF (polarizable force fields), MLPs (machine learning potentials), CGMD (coarse-grained molecular dynamics), MARTINI (a coarse-grained MD framework), LBM (lattice Boltzmann method), and DPD (dissipative particle dynamics), are included. Adapted from ref. 9 with permission from American Chemical Society, copyright 2023. Representative molecular images for various modeling techniques are displayed on the right, with the lower-right image illustrating a computational framework integrating quantum mechanics with MD using deep learning. The ion-CNT electronic density map from AIMD was reproduced from ref. 447 with permission from American Chemical Society, copyright 2016. (B) Molecular snapshots showing water structures in bulk, confined within a 1.4 nm CNT, and confined within a 0.75 nm CNT, based on AIMD simulations. Reproduced from ref. 64 with permission from American Association for the Advancement of Science, copyright 2017. (C) Change in Helmholtz free energy as a K^+ ion transitions from bulk water to the CNT interior, calculated using polarizable and nonpolarizable force fields. Top inset: Modeling of electronic polarization (EP) effects using the classical Drude oscillator model, where each CNT carbon atom is represented as a pair comprising a Drude particle (DP, representing the electron cloud) and a Drude core (DC, representing the nucleus). Bottom inset: Schematic of a K^+ ion inside the CNT, with Z = 0 corresponding to the Z-coordinate of the lowermost carbon atoms along the CNT axis. Reproduced from ref. 69 with permission from Springer Nature Limited, copyright 2022.

interaction between the tube and the entering water molecules. Additionally, the polarization of the CNT reduces the electrostatic energy of the water molecules inside the tube, further influencing the overall interaction. Li *et al.*[80] used DFT to explore the energy barriers for water and ion transport through 0.8 nm diameter CNT porins, providing insights into single-file transport kinetics. However, the high computational cost of DFT simulations limits the practical system size to sub-nanometer or nanometer scales and picosecond trajectory times. This limitation makes it difficult to capture long-timescale transport processes or incorporate structural heterogeneity relevant to experiments.

5.2.1.2 ***Ab initio* molecular dynamics.** *Ab initio* molecular dynamics (AIMD) extends computational capabilities by combining DFT with MD simulations, while keeping the quantum mechanical accuracy of DFT. In AIMD, DFT calculations are performed at each time step to determine the forces acting on atoms, which are then used to update their positions and velocities according to Newton's laws of motion. The first AIMD simulation of liquid water was conducted 30 years ago,[457,458] and since then, the method has been widely used to study water systems[457,459–464] and CNT nanofluidics.[64,176,383,385,447,465–470] For instance, AIMD simulations have been employed to simulate the water and proton diffusion, alignment, and free energy evolution in CNTs of different dimensions featuring a single-file configuration or bulk arrangement (Fig. 6B).[64,383,385,469,470] However, AIMD remains computationally demanding, restricting its application to smaller systems and short timescales, which can preclude statistically meaningful sampling of water dynamics or rare transport events.

5.2.2 Molecular dynamics simulations. MD simulations are widely used to study CNT nanofluidics, offering the ability to address larger time and length scales compared to quantum methods. MD simulations have played a foundational role in CNT nanofluidics[4] and have been employed to investigate various factors influencing nanofluidic behavior in CNTs, including diameters,[164,168,169,471–475] chiralities,[150,170,476–480] lengths,[75,76,171,450,481–483] and surface charges.[76,151,160,396,419,484–486] In MD simulations, all atoms are explicitly modeled, and their dynamics are governed by Newton's equations of motion. Interatomic forces, including vdW interactions, Coulombic forces, and bond constraints, are calculated using predefined force fields. Critically, the reliability of MD simulations depends heavily on the accuracy of these force fields.[487,488]

5.2.2.1 Classical MD simulations. Classical MD simulations rely on empirical potentials to model atomic interactions. Since the introduction of the first water models over 50 years ago,[489,490] numerous models have been developed, ranging from simple pair interaction models to more complex many-body potentials. Prominent examples include SPC/E, TIP3P, TIP4P, and TIP5P.[491–501] While classical MD models are typically calibrated to reproduce bulk water behavior,[498,499,502] they often fail under nanoconfinement. Standard water models (*e.g.*, TIP3P, SPC/E) can significantly underestimate confinement-induced changes in dielectric response, hydrogen bonding, and transport dynamics. The results are highly sensitive to the choice of water and carbon force fields, leading to inconsistent predictions across studies.[448,503–510] Most conventional force fields, such as AMBER, CHARMM, and OPLS-AA, neglect

electronic polarization. This is a serious limitation, particularly in small-diameter CNTs, where the dielectric mismatch and strong field gradients could significantly affect the nanofluidic behaviors.[69,176]

The results of MD simulations of nanofluidic transport are somewhat sensitive to whether non-equilibrium MD (NEMD) or equilibrium MD (EMD) are used. NEMD directly measures properties by applying external forces, such as pressure or electric fields, to mimic experimental conditions. However, to improve computational efficiency, many NEMD simulations apply unrealistically large perturbations, such as shear velocities exceeding 100 m s^{-1}, temperature gradients of 10^8 K m^{-1}, or electric fields on the order of 10^9 V m^{-1}.[75,76,171,173,511–517] These conditions can drive nonlinear or even nonphysical behavior, complicating direct comparison with experimental results. The method of force application can also influence outcomes: some studies apply a constant acceleration to oxygen and hydrogen atoms,[150,518] while others apply forces to water molecules at reservoir boundaries[168,169,482] or use a solid piston to push water.[162,171] The results from NEMD simulations often require careful extrapolation to align with experimental conditions. In contrast, EMD simulations calculate transport properties using linear response theory.[4,147] EMD is particularly useful for studying fluid structure, diffusion, and shear viscosity.[4,148,163,169,170,448,476,484,519–523] Additionally, EMD allows the estimation of slip lengths by calculating interfacial friction and viscosity using the Green–Kubo relationship.[150,162,168,483,524–536] However, multiple independent EMD simulations are often required to address phase space sampling limitations and ensure convergence.

The results from MD simulations can also be sensitive to the periodic boundary conditions applied. Most MD studies model nanofluidics in individual CNTs using periodic boundary conditions along the flow direction, representing either infinitely long or finite systems. In the infinite model, the CNT is filled with fluid and placed in a periodic simulation cell, effectively mimicking the high aspect ratios of CNTs.[150,163,165,168,513,518,523,537–539] This approach enables the study of fully developed flow within CNTs, providing insights into local fluid properties across different tube diameters. However, periodic boundary conditions do not account for entrance and exit effects, which can significantly influence flow behavior.[76,450,482,540,541] In contrast, finite tube models explicitly include entrance and exit regions by connecting to two water reservoirs, enabling the examination of how these factors impact nanofluidic transport, albeit at an increased computation cost.[4,69,75,76,80,162,169,171,173,176,450,482,511–515]

5.2.2.2 Multistate empirical valence bond MD simulations. Water models used in classical MD simulations cannot simulate the dissociation and recombination of water molecules, which are key to proton transport and pH equilibria.[211] The multistate empirical valence bond (MS-EVB) MD simulation method[542–546] bridges this gap by combining classical MD with empirical modeling techniques to study chemical reactions, particularly proton and electron transfer. MS-EVB MD is based on valence bond theory, where a system′s potential energy is expressed as a combination of bonding arrangements or reaction states (*e.g.*, reactants, intermediates, and products). Compared to AIMD, MS-EVB MD is computationally efficient, making it well-suited for studying complex reactions in large biomolecular or condensed-phase systems. MS-EVB MD has provided critical insights into proton dynamics in CNTs.[383,547–550] MS-EVB MD captures key proton transfer events by generating empirical potential energy surfaces that model proton hopping and water molecule reorientation, revealing how the CNT environment influences proton conductivity. For example, studies by Brewer *et al.*[547] and Dellago *et al.*[383] demonstrated that single-file hydrogen-bonded water molecules in CNTs efficiently conduct protons *via* the Grotthuss mechanism.

5.2.2.3 MD Simulations with polarizable force fields. Many directional intermolecular interactions cannot be accurately captured by scalar, pairwise-additive empirical potentials.[551] Electronic effects, such as polarization interactions, play a critical role in shaping fluid transport properties at interfaces and within CNTs. For instance, research has demonstrated that the polarization of carbon atoms by the water molecules and ions significantly influences ion hydration and diffusion in ~1.1 nm diameter CNTs.[447,468] In sub-nanometer CNTs, the influence of polarization and cation–π interactions becomes even more significant.[69,176,271,552]

Polarizable force fields integrate quantum mechanical insights to capture the electronic properties of CNTs and charge distribution variations at CNT/water interfaces. Misra and Blankschtein[69,176,553] introduced a polarizable force field based on quantum–chemical simulations to model ion and water interactions at carbon/water interfaces (Fig. 6C). Their approach employs the classical Drude oscillator model, representing each carbon atom with a Drude particle (DP) for the electron cloud and a Drude core (DC) for the nucleus, with equal but opposite charges. The Thole dipole field tensor models the interactions between the DP and DC, effectively reproducing the anisotropic polarizability tensor of carbon. One of the key findings provided by this model was that incorporating electronic polarization effects, which account for the strong electric fields exerted by partially dehydrated cations on the CNT wall, produces a large negative ion–CNT polarization energy within the CNT interior. This energy compensates for the dehydration energy, allowing ions to enter and permeate 0.8 nm diameter single-file CNTs,[69] which aligns with AIMD simulations[554] and experimental observations.[64,69,176] In contrast, classical MD simulations using empirical force fields, which neglect electronic polarization, predicted a significant free energy barrier and incorrectly concluded that ions could not enter the interior of sub-nanometer CNTs.[83,84,471] This comparison underscores the critical importance of capturing relevant interactions physics for nanofluidic transport simulations.

5.2.2.4 Machine learning based MD simulations. Machine learning (ML) approaches have emerged as powerful tools for modeling polarization interactions in MD simulations.[458] These methods leverage neural network potentials to predict charge distributions on solid surfaces based on the configurations of ions and water molecules. ML techniques aim to combine the accuracy of quantum methods with the computational efficiency of empirical potentials. Machine-learned potentials (MLPs) are typically trained on data derived from density functional theory (DFT) calculations, effectively reproducing the system's potential energy surface (PES).[555,556] Once trained, MLPs can be seamlessly integrated with classical MD simulations, enabling quantum-level accuracy in modeling condensed systems.[557–560]

The first full-dimensional MLP for bulk water and ice was introduced in 2016.[561] A significant breakthrough followed in 2018 with the development of DeePMD, a deep neural network-based approach for modeling water using MLPs that accurately reproduces PES.[562] Recently, DeePMD has been extended to study water behavior in confinements, such as graphene channels and CNTs, investigating properties like water structure,[559,563] dielectric permittivity,[564] surface friction,[467] and proton conduction.[176] As advancements in artificial intelligence continue and the complexity of modeled systems increases, innovations in MLPs are expected to drive rapid progress in the field of CNT nanofluidics. Furthermore, as more high-quality data (both experimental and simulated) become available, we expect ML-driven predictive platforms for nanofluidic transport in CNTs to emerge.

5.2.3 Continuum methods. Continuum models solve partial differential equations (PDEs) using numerical methods such as the finite element method (FEM) and finite difference method (FDM). In this approach, although both ions and water molecules have finite physical sizes, the mean-field approximation ignores their size effects, representing them only through average concentrations.[565,566] Continuum models are well-suited for mesoscale nanofluidic systems, where discrete molecular effects are negligible, provided that key factors such as channel geometry and surface boundary conditions (*e.g.*, slip length and surface charge) are properly incorporated. For instance, they are commonly used to calculate ion conductance and water flux in channels with larger diameters.[35,136,145,481,567] The continuum framework for nanofluidic transport typically relies on a combination of Poisson–Nernst–Planck (PNP) equations and the NS equations.[35,449,568]

The electric potential ϕ is described by the Poisson equation:

$$\nabla^2\phi = -\frac{eN_A\sum c_i z_i}{\varepsilon_0\varepsilon_w} \quad (10)$$

where e is the elementary charge, N_A is Avogadro's number, c_i is the local ion concentration, z_i is the ion valence, ε_0 is the vacuum permittivity, and ε_w is the relative permittivity of water.

The local ion distribution follows the Boltzmann equation:

$$c_i = c_i^0 \exp\left(-\frac{z_i e\phi}{k_B T}\right) \quad (11)$$

where c_i^0 is the bulk ion concentration, k_B is the Boltzmann constant, and T is the absolute temperature.

The ion flux J_i is governed by the Nernst–Planck (NP) equation, which accounts for diffusion under concentration gradients, electromigration in the electric field, and convective water flow:

$$J_i = -D_i\nabla c_i - \mu_i c_i z_i e\nabla\phi + uc_i \quad (12)$$

where D_i is the ion diffusion coefficient, μ_i is the ion mobility, and u is the water velocity.

Finally, the water velocity satisfies the continuity equation, $\nabla\cdot u = 0$, and the NS equation:

$$\rho(u\cdot\nabla)u = -\nabla p + \nabla\cdot\eta\nabla u - e\sum c_i z_i\nabla\phi \quad (13)$$

where ρ is the fluid density, p is the pressure, and η is the dynamic viscosity. When a simulation focuses solely on ion transport, the NS equations are often omitted, resulting in a model that neglects electroosmosis. The NS equations also rely on boundary conditions that implicitly assume a slip length, which may not be valid at subcontinuum scales where bulk viscosity description breaks down.

We caution that continuum descriptions and assumptions often break down in nanofluidic systems.[569–573] For instance, mean-field approximations fail to capture local correlations between ions and water near interfaces,[574,575] and the dielectric profile becomes non-uniform and anisotropic.[576] Additionally, properties such as viscosity and surface friction are strongly confinement-dependent.[577] Despite these limitations, continuum approaches can still be effective under extreme confinement when they properly account for spatial variations in transport properties, finite sizes of water and ions, and specific interactions. For example, Bazant *et al.* proposed a higher-order Poisson equation to incorporate electrostatic correlations, such as charge inversion.[578–581] Multiscale models have also been developed to bridge the gap between computational regimes. Hybrid MD–continuum methods combine the accuracy of MD for local interactions with the efficiency of continuum models for larger-scale behavior, which offer a powerful framework for capturing nanoscale effects while remaining computationally tractable.[450,582–586]

6 Water and ion transport in CNTs

We now describe the results of the investigations of fluid and ion transport under extreme confinement, surface interactions, and channel entry effects in CNTs. We focus primarily on the results of the experimental probing of the CNT nanofluidic transport, and supplement these findings with relevant simulation studies to offer additional physical insights.

6.1 Transport phenomena dominated by extreme confinement in CNTs

Fluid behavior in CNTs varies significantly with their diameter. As the diameter decreases below a critical threshold, typically several times the size of a water molecule, fluid behavior

diverges from bulk-like properties (Fig. 2), entering a sub-continuum regime.[1,35] As the CNT diameter narrows further, fluid structuring and solute dehydration effects gain prominence, culminating in sub-1 nm CNTs where only a single-file arrangement of molecules is possible.[4,64,80] We now describe some of these phenomena starting from the transport in ultra-narrow, single-file CNT pores.

6.1.1 Enhanced water transport in single-file CNTs. Extreme spatial confinement and single-file water arrangement in narrow CNTs facilitates a highly ordered and efficient water flow through the channel that significantly minimizes energy dissipation and maximizes the overall flux. Theoretical and computational studies have been pivotal in predicting and elucidating the physics of enhanced water transport in single-file CNTs.[4,148,152,157,164,169,171,419,423,466,472,485,486,515,521–523,588–598] Simulations show that the primary energy barrier for water transport is dominated by the rearrangement of intermolecular hydrogen bonds. As water molecules enter these CNTs, they must reorganize their hydrogen-bonding network to fit within the confined space, which is crucial for facilitating the entry and subsequent flow of water molecules through the CNT. The unique properties of CNTs, such as their hydrophobic interior and smooth, frictionless walls, then contribute to the rapid nearly frictionless transport of water molecules. A number of experimental studies[64,80,134,143,436] have provided solid confirmation of the enhanced water transport capabilities of single-file CNTs and offered new perspectives on the water transport mechanism in these channels.

6.1.1.1 Water permeability of single-file CNTs. Hummer *et al.*[4] first simulated water transport in 0.8 nm diameter CNTs (6,6) and calculated a water conduction rate of $p_f \sim 5.1 \times 10^{-13}$ cm^3 s^{-1} (1.7×10^{10} H_2O per s), which was comparable to the transport rate found in aquaporin-1 (AQP1) (the historically reported value of $p_f \sim 1.17 \times 10^{-13}$ cm^3 s^{-1} (3.9×10^9 H_2O per s)[191] or the recently updated value of $p_f \sim 5.4 \times 10^{-13}$ cm^3 s^{-1} (1.8×10^{10} H_2O per s)[599]). Following this initial discovery, researchers dedicated substantial effort to further studying water transport in single-file CNTs; however, these efforts mainly involved simulations.[148,152,153,157,164,169,171,419,423,466,472,485,515,521–523,588–598,600] Surprisingly, due to significant technical challenges in experimentally measuring water flow in sub-1 nm diameter CNTs, only the Liu,[134] Noy[64,80,176,436] and Shan[143] groups reported water transport efficiency in single-file CNTs.

The Noy group[64,80,176,436] investigated water transport in single-file CNT porins using a liposome-based measurement in which water flux was driven by osmotic imbalance (Fig. 4 and 7). Tunuguntla *et al.*[64] measured water transport by monitoring changes in liposome volume using light scattering, reporting a water permeability of $\sim 6.8 \times 10^{-13}$ cm^3 s^{-1} (2.3×10^{10} H_2O per s) per channel for narrow CNT porins with an average diameter of $\sim$0.8 nm and a length of $\sim$10 nm (Fig. 7A). Later, Li *et al.*[80] refined this measurement using a similar approach based on the self-quenching of carboxyfluorescein (CF) dye to detect volume changes in liposomes. This approach provided a more precise water permeability value of $\sim 2.3 \times 10^{-13}$ cm^3 s^{-1} (7.7×10^9 H_2O per s) per channel, avoiding the artifacts and complexities associated with the relationship between liposome size and light scattering. The refined value aligns with MD predictions[4] and is comparable to the unitary permeability of AQP1.[191,599] Notably, these values exceed the permeability of wider 1.5 nm CNT porins ($\sim 5.9 \times 10^{-14}$ cm^3 s^{-1}). Additionally, the experimental data show that altering the solution from neutral to acidic pH, where the anionic COO^- groups on the CNT porin rim become protonated, enhances water permeability in both 0.8 nm and 1.5 nm diameter CNT porins.[64]

The water diffusion coefficient can be calculated from the unitary permeability, p_f, values. Although the continuous approximation is not strictly valid in this context, we assume, for comparison purposes, that the water density within the pore remains similar to the bulk water density value. Under this assumption, the effective diffusion coefficient D can be estimated as follows:

$$D = \frac{4L}{\pi d^2} p_f \tag{14}$$

where D is the diffusion coefficient, L is the CNT length, and d is the CNT diameter. The water diffusion coefficient measured at pH 3 for the 1.5 nm diameter CNT porins is found to closely align with the value observed in bulk water (Fig. 7B). This observation suggests that, under these conditions, the influence of protonated COO^- groups at the porin rim becomes negligible, allowing water molecules to diffuse in a manner similar to their behavior in the bulk phase (Fig. 6B). In contrast, the higher water diffusion coefficient measured in the 0.8 nm diameter CNT porins highlights the unique transport dynamics in the single-file configuration that is distinct from and more efficient than bulk water diffusion (Fig. 6B).

In addition, water permeability (p_f) is typically expressed as the rate of water permeation normalized by the osmolyte concentration driving the flow, equivalent to a pressure of $\sim$25 bar ($\sim$360 psi). Accurate measurements require careful use of the vant Hoff equation ($\Delta\Pi = \Delta C_{osm} RT$) to avoid misinterpretations:

$$J_w = j_w V_w = p_f \Delta C_{osm} = \frac{p_f V_w}{RT} \Delta\Pi \tag{15}$$

Here, j_w represents the molar flux of water (mole s^{-1}), ΔC_{osm} is the osmolyte concentration (osmol per m^3), J_w is the volumetric water flux (L s^{-1}) per channel, V_w is the molar volume of water (18.07 cm^3 mol^{-1}), R is the ideal gas constant, T is temperature (K), and $\Delta\Pi$ is the osmotic pressure. Considering the cross-sectional area of a 0.8 nm CNT porin ($\sim$0.5 nm^2), the ideal water permeance for a single channel is $\sim 1.66 \times 10^{-19}$ L s^{-1} per bar. The corresponding permeability is $\sim$1200 LMH per bar (liters per square meter per hour per bar), significantly higher than that of AQP1 ($\sim$35 or 155 LMH per bar).

Besides the single-file water transport in ultrashort CNT porins, the other two groups reported the water transport in the micron-long single-file CNTs (Fig. 7B), which highlights the importance of entrance effects on water transport. Qin *et al.*[134] used a field-effect transistor (FET) array to track water filling

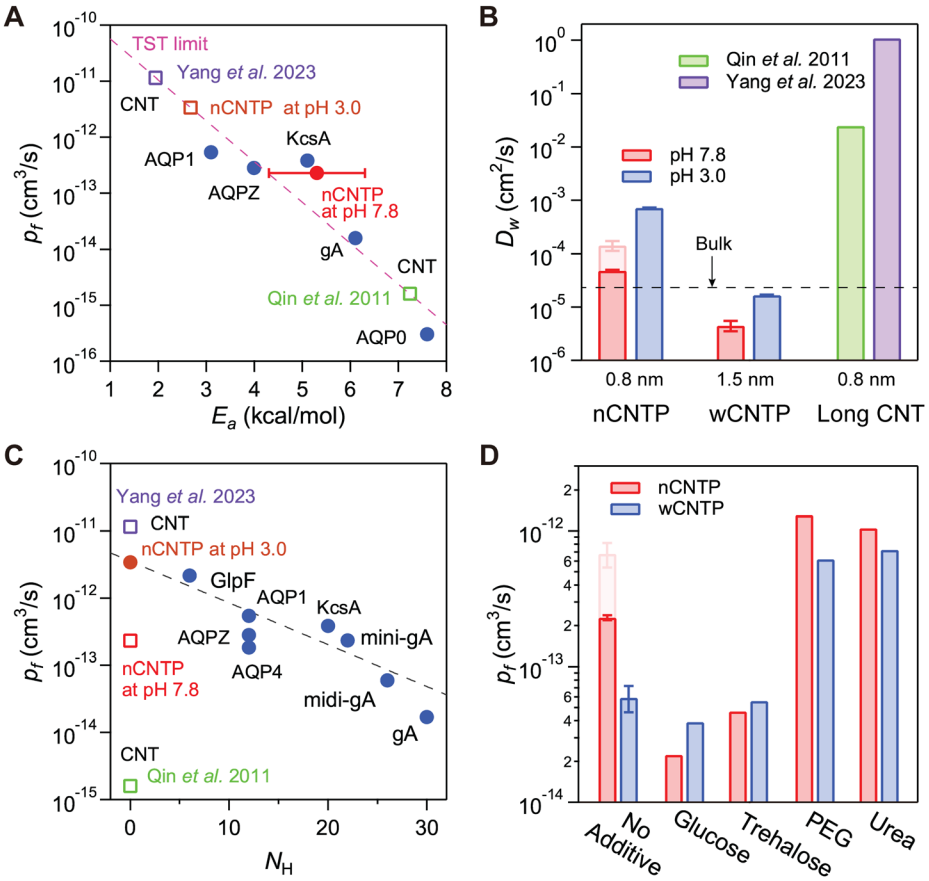

Fig. 7 Water transport in single-file CNTs. (A) Relationship between unitary water permeability (p_f) and activation energy barrier (E_a) for single-file CNTs, CNT porins (CNTPs), and biological channels. The pink line represents theoretical values calculated using transition state theory (TST, eqn (16)). Circle markers show experimentally determined permeability and activation energy, while square markers indicate experimental permeability with estimated activation energy derived from eqn (16). (B) Diffusion coefficients derived from water permeability at various pH levels for short 0.8 nm diameter narrow CNT porins (nCNTPs), 1.5 nm diameter wide CNT porins (wCNTPs), and long CNTs. For nCNTPs, semi-transparent red bars represent earlier measurements,[64] while solid red bars reflect more recent data.[80] (C) Unitary water permeability of a channel plotted as a function of the number of available hydrogen bond donors and acceptors (N_H) inside the channel. Dashed lines provide an exponential fit to the data as a visual guide. (D) Water permeability of CNT porins measured at neutral pH in the presence of chaotropes (*e.g.*, PEG and urea) and kosmotropes (*e.g.*, glucose and trehalose). Data for biological channels were extracted from ref. 587, CNT porin data from ref. 64 and 80, and other CNT data from ref. 134 and 143.

velocity in individual CNTs, reporting that water transport does not increase consistently with decreasing diameter and that there is a discontinuity below 1 nm. For CNTs with 0.81 nm diameter and 800 μm length, they measured a water permeability of $p_f \sim 1.6 \times 10^{-15}$ cm^3 s^{-1}, which is two orders of magnitude lower than values predicted by MD[4] and AQP1 rates.[191,599] However, the driving force for water filling into CNTs was estimated based on MD simulations, which could be inaccurate. Yang *et al.*[143] used a free-standing CNT membrane aligned with an electric field to measure water transport, obtaining an extremely high permeability of approximately $\sim 1.15 \times 10^{-11}$ cm^3 s^{-1} for 0.82 nm diameter, 5 μm long CNTs. However, potential issues with CNT density estimates and membrane leakage could have affected those results.

6.1.1.2 Activation energy and hydrogen bonding dynamics for water transport in single-file CNTs. Water transport through single-file CNTs is considered an activated process, characterized by an activation energy E_a.[601] The water permeability in these systems can be described using transition state theory[44,587] as follows:

$$p_f = \frac{v_0 V_w}{N_A} \exp\left(-\frac{E_a}{RT}\right) \quad (16)$$

where E_a (kcal mol^{-1}) represents the activation energy, and $v_0 \approx 10^{13}$ s^{-1} is the molecular attempt frequency. This relationship relies on the alignment of water molecules in a single-file column within the nanotube, where each molecule "hops" from one position to the next. The rapid permeation observed in single-file biological channels is linked to the low activation energy, typically around ~ 5 kcal mol^{-1}—similar to the self-diffusion activation energy of water (~ 4.2 kcal mol^{-1}).[601,602] Li *et al.*[80] measured the activation energy for water transport in narrow CNT porins by analyzing permeability as a function of temperature, reporting an E_a of ~ 5.3 kcal mol^{-1}. This value is consistent with the typical range for single-file water channels and aligns well with theoretical predictions (Fig. 7A). Then

based on transition state theory (eqn (16)), the water permeability at physiological temperature ($\sim$37 °C) is estimated to be $\sim$1.5 times higher than that at room temperature. MD simulations[80] also revealed that water transport in single-file CNT porins can be divided into three stages. First, a water molecule approaching the CNT entrance undergoes partial desolvation at the CNT entrance. Then, a pseudo-solvation shell forms, composed of oxygen atoms from both the solvent and COO^- groups at the CNT entrance. Finally, the water molecule loses two hydrogen bonds and becomes part of the single-file chain inside the CNT. This loss incurs an energy cost, which is compensated by several factors:[164] strengthening of the two remaining hydrogen bonds, favorable vdW interactions with the CNT walls, and the residual rotational entropy of the unbound OH bond. Once the water molecules are within the CNT wall, they move collectively with minimal resistance over the smooth CNT surface.

The exponential dependence of water permeability on the number of intra-channel hydrogen bonding sites N_H suggests that single-file water molecules experience nearly frictionless transport inside CNTs (Fig. 7C).[599,601] Evidence of the single-file configuration in water transport can also be observed through the impact of compounds that influence the intermolecular hydrogen-bonding network in water. Tunuguntla *et al.*[64,436] found that weakening the hydrogen bond network in bulk water, using chaotropic co-solvents such as PEG4 or urea, promotes water permeability (Fig. 7D). Conversely, kosmotropic co-solvents that strengthen hydrogen bonds, such as glucose or trehalose, reduce water permeability.[436]

6.1.2 Ultrafast proton transport in single-file CNTs. Proton transport in water is fundamental to biological systems and critical for technological applications such as fuel cell membranes.[546,604,605] Proton conduction occurs through two main mechanisms: vehicular diffusion, where a hydrated proton (hydronium ion) travels with its surrounding water molecules intact, and Grotthuss diffusion, where the proton hops along a chain of hydrogen-bonded water molecules.[211,606–608] This nearly 100-year-old concept[609] explains how protons can "tunnel" along a chain of hydrogen bonds, moving rapidly across water molecules in a cascade-like process similar to Newton's cradle.[606,610,611] In bulk water, protons display much higher mobility than other small ions, largely due to Grotthuss transport.[211,606,607] Once a proton is introduced in water, it typically binds to a water molecule, forming a hydronium ion.[612] More precisely, hydronium ions exist in two main forms:[606,613–615] the Eigen cation ($H_9O_4^+$), where the proton is bound within a larger solvation shell, and the Zundel cation ($H_5O_2^+$), where the proton sits between two water molecules, enhancing its transfer ability. The Grotthuss mechanism depends on these solvation states to facilitate fast proton transport, as protons hop across water molecules without requiring the actual movement of the water molecules themselves along the diffusion path.

When water is confined within narrow hydrophobic nanopores, the dynamics of proton transport changes significantly.[180,383–385,465,470,546–549,616–619] In these restricted environments, the typical 3D hydrogen-bond network found in bulk water shifts to a 1D hydrogen-bonded chain, limiting the usual solvation patterns of protons and potentially altering the proton transfer mechanism. For instance, the natural proton channel gramicidin A achieves ultrafast proton transport by aligning water molecules in a single file, thus creating a continuous hydrogen-bonded pathway that enables efficient proton hopping.[417] In contrast, similar biological channels with single-file water chains, such as AQPs, are less permeable to protons due to differences in pore chemistry, which affect the orientation and dipole alignment of water molecules within the chain.[415,620] Experimental and simulation studies have shown that sub-1-nm diameter CNTs promote the formation of single-file water chains and provide an ideal model for exploring proton transport within a confined 1D environment.[148,157,358,384,621–626] Research on proton transport in CNTs began with early studies using AIMD and MS-EVB MD methods in 2001.[383–385,547] These foundational studies and the subsequent experimental works[46,65,176,180,438,627] established single-file water chains in CNTs as perhaps the ultimate models of efficient proton conductance.

6.1.2.1 Grotthuss proton conduction along single-file water. Early studies on Grotthuss proton transport in single-file CNTs focused primarily on understanding the rates and dynamics of proton movement. In 2003, researchers observed that in CNTs with single-file water, protons move efficiently through shifts in ionic defects (hydronium and hydroxide ions) and through hydrogen-bond defects (Fig. 8A).[383,589] Proton transport along a water chain requires a specific dipole orientation within the chain: hydronium ions move along chains where dipole moments point outward, while hydroxide ions move along chains where dipoles are directed inward. Once an ionic defect is present in the chain, it can diffuse in both directions. Proton diffusion in a 0.8 nm diameter CNT reaches $\sim 1.7 \times 10^{-3}$ cm^2 s^{-1} ($\sim$40 times faster than the simulated diffusion coefficient in bulk water). As protons or hydroxide ions travel, they reorient nearby water molecules, creating a flipped chain alignment in their path. To reset this alignment after charge translocation, hydrogen-bond defects must diffuse along the chain. These defects, formed at the junctions between oppositely aligned water chains, move through dipole flips and serve as charge carriers. Analogous to ice defects, these are termed *D*-defects (double acceptor bonds) and *L*-defects (double donor bonds). Although slower than proton hopping, with diffusion rates of $\sim 5 \times 10^{-4}$cm^2 s^{-1} for *D*-defects and $\sim 3 \times 10^{-4}$ cm^2 s^{-1} for *L*-defects, they are essential in completing the proton transport cycle. Together, the movement of ionic and hydrogen-bond defects allows the ordered water chain within CNTs to sustain continuous proton flow, predicting approximately one order of magnitude enhancement of the proton transport rate over the bulk water value.[383]

Subsequent studies considered the formation of single water wires and alternative proton transport mechanisms in CNTs, examining the behavior of larger cationic clusters such as the Zundel ($H_5O_2^+$), Eigen ($H_9O_4^+$), and linear $H_7O_3^+$

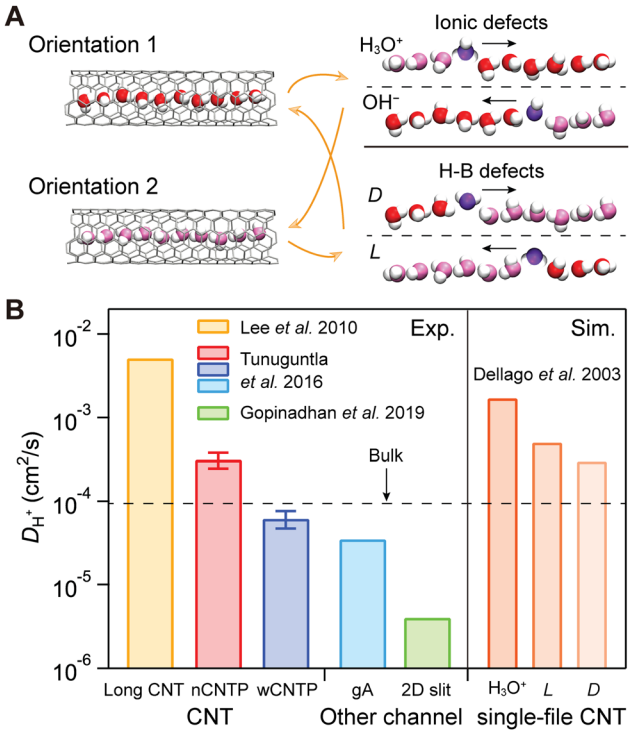

Fig. 8 Enhanced proton transport in CNTs. (A) Schematic of the charge transport mechanisms. (B) Proton diffusion coefficients across different environments, including bulk water,[603,604] two-dimensional (2D) graphite slits,[65] gramicidin A (gA) channels,[180,604] long CNTs[121] and CNT porins.[180] Simulations from ref. 383 provide proton transport data for a CNT (6,6) in an ideal case and in presence of a *D* or *L* defect.

cations.[385,470,548] Mann and Halls[385] investigated the stabilization of protons in CNTs through the formation of the Eigen ($H_9O_4^+$) complex, predicting enhanced proton conduction. Cao *et al.*[548] proposed a "Zundel–Zundel ($H_5O_2^+$)" mechanism for proton transport along extended (greater than 5 nm) one-dimensional water chains in CNTs, involving a transient $H_7O_3^+$ structure. This finding, also supported by further research,[628–632] differs from the conventional Grotthuss mechanism in bulk water, where proton transport follows a "Zundel–Eigen–Zundel" sequence.[606,613–615] In confined CNTs, unique effects, such as changes in curvature, electrostatic interactions from fixed charges, polar or charged amino acids, and external electric fields, can influence proton conduction, similar to effects seen in biological channels.[188,384,620,626,633,634] For instance, Zhu and Schulten[384] demonstrated that proton transport in CNTs is highly sensitive to charge distribution, especially at the pore entrance, where local charges can reorient water molecules. Positive charges attract electronegative oxygen atoms, forming *L*-defects, while negative charges attract hydrogen atoms, resulting in *D*-defects. Additionally, curvature-induced dipoles within the CNT also reorient water molecules, causing each molecule to act as a hydrogen bond donor to adjacent molecules and resulting in *L*-defects, which are more prevalent than *D*-defects due to orientation effects at the CNT entry.[626] These insights also suggest possible mechanisms for controlled water and proton transport in CNTs.

6.1.2.2 Enhanced proton transport in single-file CNT porins. The pioneering simulation studies on proton transport in CNTs identified key characteristics that have since driven extensive experimental research. Early work in 2010 by the Strano group provided experimental evidence of high proton conduction in 500 μm-long, 1.5 nm-diameter CNTs using a substrate-bound CNT platform (Fig. 4).[113,121] Under an electric field, these CNTs showed protons as the dominant charge carriers even at neutral pH, with cation identity affecting the duration and degree of conductance decrease during pore-blocking events. At lower pH and high ion concentrations, both single-channel current and blockade intensity increased, indicating that protons were the primary conductors. The estimated proton mobility was $\sim 0.2\ cm^2\ V^{-1}\ s^{-1}$, equating to a proton diffusion coefficient of $\sim 5.1 \times 10^{-3}\ cm^2\ s^{-1}$, nearly 50 times higher than in bulk water ($\sim 9.3 \times 10^{-5}\ cm^2\ s^{-1}$).[603,604] To this day, discrepancies across different long CNT nanofluidic platforms and research teams remain. For instance, while a proton-dominated ionic current and cation-blocking events were observed by Strano *et al.*,[113,121] other studies reported electrolyte ions as the main current carriers for similar long CNT sizes.[74,108,122,132,143,401]

The development of sub-1-nm diameter CNT porins by the Noy group offered a different opportunity to explore proton transport in single-file water channels. In 2016, Tunuguntla *et al.*[180] investigated proton conduction in CNT porins embedded in lipid vesicles containing a pH indicator dye (Fig. 4). Proton permeability measured in 0.8-nm-diameter CNT porins was $\sim 1.5 \times 10^{-12}\ cm^3\ s^{-1}$, while for wider 1.5-nm-diameter CNT porins, it was $\sim 8.2 \times 10^{-13}\ cm^3\ s^{-1}$, yielding diffusion coefficients of $\sim 3.2 \times 10^{-4}\ cm^2\ s^{-1}$ and $\sim 6.2 \times 10^{-5}\ cm^2\ s^{-1}$, respectively (Fig. 8B). This comparison implies that 1.5 nm CNTs are not narrow enough to induce strong molecular confinement, resulting in a hydrogen bonding network similar to bulk water,[603,604] a conclusion also supported by simulations.[64,169] In contrast, the narrow CNT porins exhibited a proton diffusion coefficient ~ 5 times higher than that in the larger diameter CNT porins, exceeding the bulk value by an order of magnitude and confirming simulation predictions for Grotthuss proton transport in single-file CNTs. Indeed, the measured diffusion coefficient for narrow CNT porins was lower than that for pure protonic (H_3O^+) transport in 0.8 nm CNTs but matched calculated values for proton transport coupled to a *D*- or *L*-defect[383] (Fig. 8B). These findings establish a combination of proton hopping and defect reorientation as the key mechanism for rapid proton translocation in CNTs.

Note that transport in narrow CNT porins is faster than in gramicidin A channels (diffusion coefficient $\sim 3.5 \times 10^{-5}\ cm^2\ s^{-1}$[180,604]), likely due to the smooth carbon surface and more precise single-file arrangement of water molecules. Additionally, proton conduction through narrow CNT porins decreased upon adding Ca^{2+} ions,[180] suggesting that divalent cations influence proton transport either by direct interaction with negatively charged pore entrances or by screening the ionic environment at the membrane interface, similar to gramicidin A channels. Interestingly, proton diffusion in narrow

CNT porins was up to two orders of magnitude higher than in ~0.4 nm 2D graphite slits (~4×10^{-6} cm^2 s^{-1}),[65] where water molecules form a square-like hydrogen-bonded monolayer that restricts rotation. This observation confirms that single-file hydrogen bonding in narrow CNTs is crucial for enhanced proton transport.

Choi *et al.*[113] found activation energies ranging from 6 to 15 kcal mol^{-1} for micron-long CNTs with a diameter of ~1.6 nm. Tunuguntla *et al.*[180] reported activation energies of ~13.3 kcal mol^{-1} for 0.8 nm diameter CNT porins and ~8 kcal mol^{-1} for 1.5 nm diameter CNT porins. These values closely align with simulation predictions,[549] but are significantly higher than the activation energies (2–4 kcal mol^{-1}) typically associated with the Grotthuss mechanism,[412,606,635,636] such as those observed in gramicidin A channels. The elevated activation energies could be attributed to barriers encountered during the entry or exit of protons in the CNTs, or to the temperature-dependent dynamics of proton and water structures. Further simulations and experimental investigation of these questions are warranted, as the current activation energy values in CNTs appear too high to account for the observed rapid proton transport.

6.1.3 Electrophoretic ion transport in narrow CNTs and Nernst–Einstein relation under confinement. Unlike water and proton transport in single-file CNTs, ion transport presents more complex dynamics in narrow channels. First, ions in the bulk are surrounded by a hydration shell that must deform or partially shed for ions to enter narrow CNTs, which makes ion transport more energy-intensive.[83,209,471,637,638] Ions in CNTs also experience confinement differently due to the dielectric contrast between the aqueous environment and the CNT wall, impacting transport behavior.[35,209,210,639,640] Research has shown that ion concentration within sub-nanometer CNTs does not necessarily match that of the surrounding reservoirs, a characteristic typically observed in larger, uncharged CNTs.[641] Second, water and proton transport in single-file channels is facilitated by hydrogen bonding and proton hopping mechanisms, allowing smoother, continuous movement. These mechanisms are unavailable to ions. For example, a single cation in a CNT lined with water molecules is hydrated by the water chain on either side, with oxygen atoms from each water molecule aligning near the ion.[69] Consequently, ions must either physically diffuse through the CNT, exchanging positions with the water molecules, or push the entire chain forward in piston-like fashion,[642] both of which introduce significant resistance. Furthermore, ions carry an intrinsic charge, introducing electrostatic interactions that influence transport patterns.[64,643,644] These electrostatic effects, coupled with the electronic properties of CNTs,[69,176,252,400,564] create potential barriers that regulate ion flow, distinguishing ion transport dynamics from those of protons and water.

6.1.3.1 Breakdown of the Nernst–Einstein relation in single-file CNT porins. In continuum modeling of ion transport within CNTs and other nanochannels, the NP equation (eqn (12)) is commonly used to describe ion flux and conductance. In the equation, the diffusion coefficient D reflects the rate at which ions propagate due to random thermal motion, while the electrophoretic mobility μ indicates the ion's velocity in response to an electric field. Since both diffusion and electrophoretic movement are influenced by collisions between ions and surrounding water molecules, a relationship always exists between D and μ, expressed as:

$$D = \frac{k_B T}{q}\mu \tag{17}$$

where q represents the ion charge, k_B is the Boltzmann constant, and T is the temperature. This famous relationship, known as the Nernst–Einstein relation, was first introduced by Walther Nernst[645] and subsequently advanced by Albert Einstein.[646] This relation, which is a specific case of the fluctuation–dissipation theorem,[647] lies at the heart of statistical physics, and any insights into its violation are crucial for understanding transport phenomena in nanostructures.[648] In the past, deviations from the Nernst–Einstein relation have been proposed[8,649–651] and observed[652–656] in solid-state semiconductors; in contrast, it has been extensively validated in bulk solutions and is generally assumed to hold even in channels as narrow as a few nanometers.[208,657,658]

Nevertheless, Li *et al.*[69] demonstrated that the Nernst–Einstein relation breaks down for ion transport in 0.8 nm diameter single-file CNT porins. Using a liposome-based platform (Fig. 4 and Fig. 9A inset), the authors measured ion diffusion in CNT porins. The resulting K^+ ion permeability of a single CNT, ~3.69×10^{-17} cm^3 s^{-1}, corresponds to a diffusion coefficient of ~7.34×10^{-13} m^2 s^{-1}, more than three orders of magnitude lower than in bulk solution (Fig. 9A). While a reduction in the K^+ ion diffusion coefficient aligns with the intuitive expectation of reduced diffusion efficiency in a crowded and confined CNT porin interior, this significant decrease still cannot be explained by classical hindered transport models.[659,660] Surprisingly, the measured CNT porin ion conductance of ~35.7 pS corresponded to a K^+ ion electrophoretic mobility of ~7.85×10^{-8} m^2 V^{-1} s^{-1} (Fig. 9A), which approached the bulk value. Consequently, the Nernst–Einstein ratio $r_{NE} = \left(\frac{\mu}{D}\right) \Big/ \left(\frac{q}{k_B T}\right)$ deviated from the expected value of 1 by over three orders of magnitude (Fig. 9B)!

MD simulations with polarizable force fields[69,553,644] solved this puzzle (Fig. 6C and 9C). First, the simulations confirmed that K^+ ions diffuse very slowly within CNT porins due to the strict single-file confinement, making it challenging for ions to exchange places with neighboring water molecules (Fig. 9C). The simulations also reveal a striking behavior where under the influence of an electric field the water chain within the nanotube breaks apart and K^+ ions fly through the empty nanotube in the form of ion–water clusters, accounting for the high electrophoretic mobility observed experimentally. This ion–water cluster structure extends until the attractive force between an ion and a water molecule falls below $k_B T$, limiting the cluster size to approximately eight water molecules with a

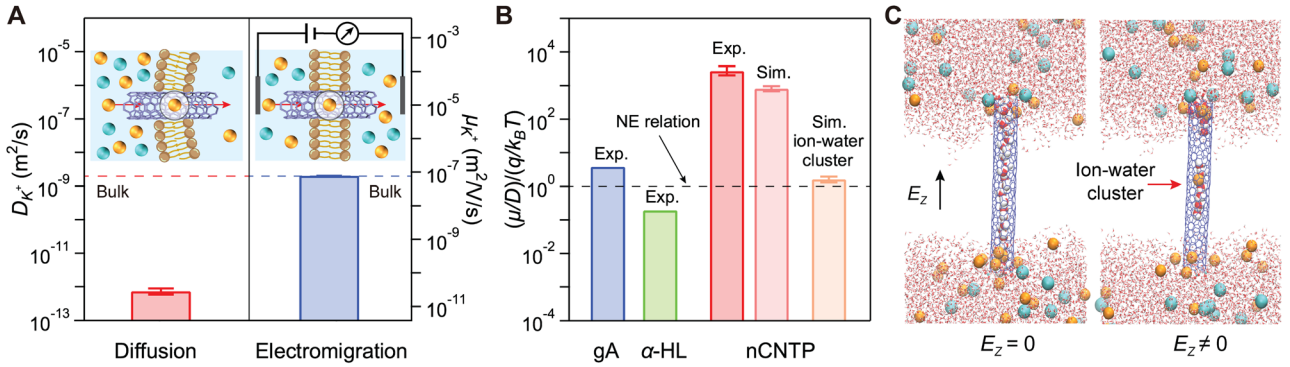

Fig. 9 Ion diffusion, electromigration, and the Nernst–Einstein (NE) ratio in single-file CNT porins. (A) K^+ ion diffusion coefficient and mobility in 0.8 nm diameter narrow CNT porins (nCNTPs). Dashed lines indicate bulk values of the diffusion coefficient and mobility of K^+ ions. Left inset: Cartoon showing K^+ ion diffusion across CNT porins under concentration gradients. Right inset: Cartoon showing K^+ ion electromigration through CNT porins under an external electric field. (B) Experimentally determined ion mobility-to-diffusion coefficient ratios $\left(\text{NE ratio, } \frac{\mu}{D}\Big/\frac{q}{k_B T}\right)$ for K^+ ion transport in CNT porins and gramicidin A (gA) channels, as well as Ca^{2+} ion transport in alpha-hemolysin (α-HL) channels, as well the NE ratios for CNT porins calculated from MD simulations. The dashed line indicates the expected value of the NE relation, $\frac{\mu}{D}\Big/\frac{q}{k_B T} = 1$. (C) MD simulation snapshots of CNT porins showing a single-file water chain inside the CNT porin without an external electric field (E_z = 0) and the translocation of a K^+ ion in the form of a stable ion-water cluster under an external electric field ($E_z \neq 0$). Data in panels (A) and (B) are extracted from ref. 69, and snapshots in the panel (C) are reproduced from ref. 69 with permission from Springer Nature Limited, copyright 2022.

slightly asymmetric shape. Remarkably, the Nernst–Einstein ratio estimated from the simulations matched the experimental values and confirmed the drastic differences in the microscopic mechanism of diffusion and electromigration in these channels as the main origin of its violation. Subsequently, Lau *et al.*[68] demonstrated that ion–water cluster movement in single-file CNTs is governed by dry friction rather than viscous friction. They developed an analytical modeling of ion flow, where the ion is hydrated by short water chains on each side. By solving the Fokker–Planck equation for a Langevin equation incorporating dry friction, the model quantitatively reproduces the experimentally observed violation of Nernst–Einstein relation.[69] Notably, the ion–water clusters still follow the Nernst–Einstein relation (Fig. 9B), affirming that this relation holds as long as diffusion and electrophoresis are governed by similar microscopic interactions.

6.2 Transport phenomena dominated by CNT wall properties

In addition to the strong confinement effects, transport phenomena in CNTs are profoundly influenced by the distinctive properties of their walls, which act as dynamic interfaces rather than just static boundaries. A marquee feature of CNTs, their exceptional water transport efficiency,[5,6,25,60,64,119,127,134,143] is driven by a low-friction environment characterized by pronounced wall slip (Fig. 2D). Beyond hydrodynamic attributes, CNT walls also modulate ion conductance and charge regulation, with surface charges (Fig. 2E) dynamically influencing ion selectivity, concentration, and ion mobility.[122,136,145,661,662] The electronic properties of CNT walls, defined by their chirality and corresponding electronic band structure, play a critical role, with electronic polarization effects (Fig. 6C) influencing charge distribution, fluid-wall interactions, and molecular transport efficiency.[9,15,69,73,113,122,123,176,222,400,472] The coupling between ions and water molecules in CNTs also introduces additional complexity and can give rise to phenomena such as electroosmosis and streaming currents.[74,114,124,126,132,141,145,663]

6.2.1 Water transport and wall slip. The seminal MD-based prediction of fast water flow in CNTs[4] triggered extensive experimental studies of this phenomenon,[6,25,60] establishing a benchmark for efficient nanofluidic transport. Fast water flow in CNTs is attributed to their intrinsic hydrophobicity and atomically smooth CNT walls, which facilitate high slip flow (Fig. 2D) and enable flow rates far exceeding those predicted by classical Hagen–Poiseuille (H-P) theory. A large number of MD simulations and experimental studies have consistently reported unexpectedly high flow enhancements in CNTs; however, the reported flow-enhancement ratios (ε) vary substantially, ranging from 1 to 106 (Fig. 10 and Table S2, ESI†). Furthermore, a persistent discrepancy of up to three-orders-of-magnitude between MD predictions and experimental measurements in CNTs remains unresolved. In this section, we review the available data on water flow enhancements in CNTs, examine the factors influencing fast water transport, and explore the relationship between slip flow and the properties of CNT walls.

6.2.1.1 Slip flow enhancement in CNTs. When a CNT of diameter d and length L is subjected to a pressure gradient ΔP, the radial water velocity profile $u(r)$ (m s^{-1}) (Fig. 2D) can be described by eqn (18), a specific solution to the NS equations for laminar flow in a cylindrical tube:

$$u(r) = \frac{(d/2)^2}{4\mu}\left[1 - \frac{r^2}{(d/2)^2} + \frac{2L_s}{(d/2)}\right]\frac{\Delta P}{L} \qquad (18)$$

where μ is the viscosity of water ($\sim$1.002 mPa s in bulk), and L_s is the slip length at the water/CNT interface, describing the

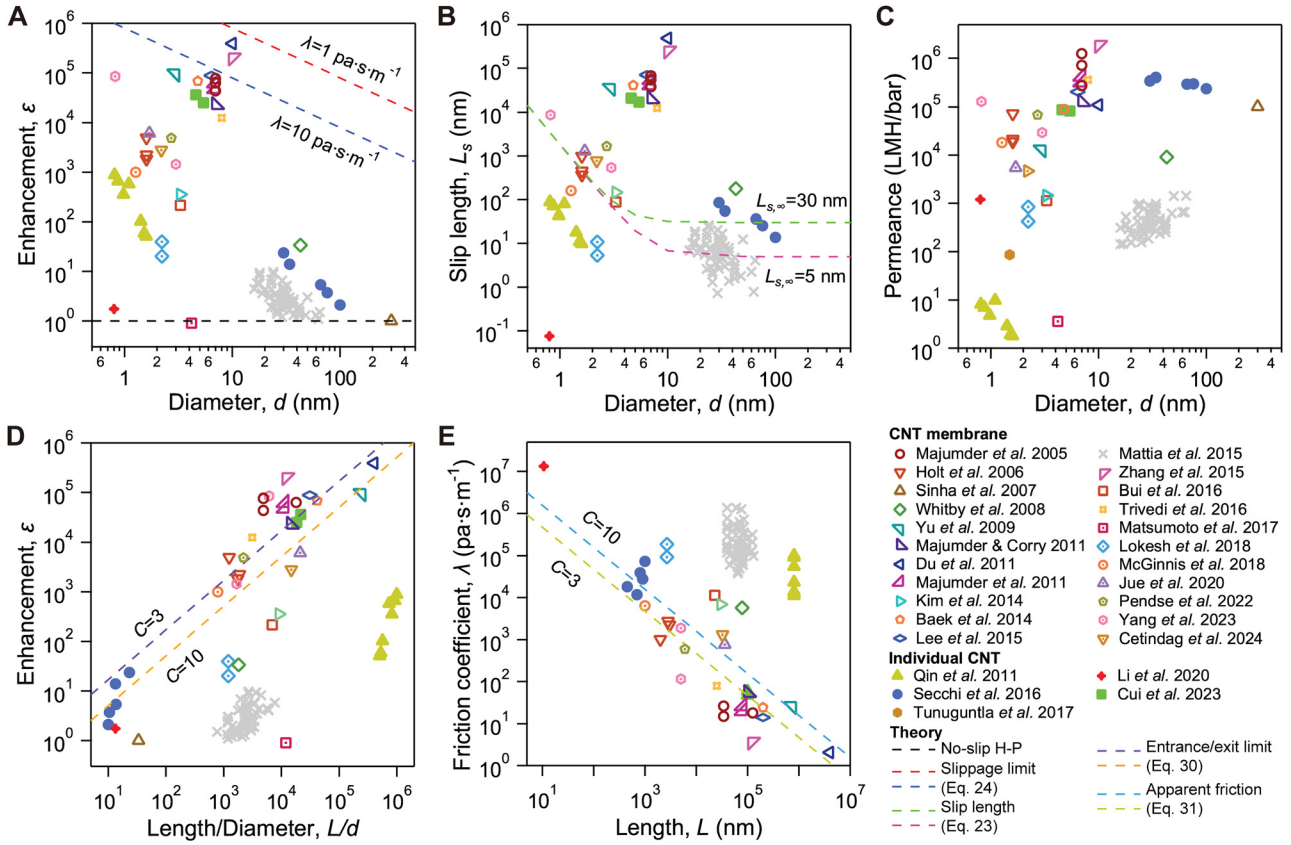

Fig. 10 Water flow enhancement in CNT channels. (A) Reported flow enhancement factor (ε) as a function of CNT diameter (d). For studies without reported ε, values were estimated using the reported slip length and eqn (22). Dashed lines indicate ε limits due to slippage, excluding entrance/exit losses (eqn (23)). (B) Slip length (L_s) *versus* d, calculated using eqn (22), ignoring entrance/exit losses. Dashed lines represent fits based on different slip lengths for flat graphene surfaces (eqn (25)). (C) Water permeance through single CNTs, normalized by the CNT area, calculated using flow enhancement factors (ε) from the literature and eqn (19) and (21). (D) ε as a function of the CNT length-to-diameter ratio, with dashed lines showing limits due to entrance/exit losses for C = 3 and C = 10 (eqn (35)). (E) Apparent friction coefficient (λ) for the water–carbon interface (eqn (23)). Dashed lines depict predictions from eqn (36) for C = 3 and C = 10 under entrance/exit-dominated losses. Data were extracted from ref. 6, 24, 25, 60, 64, 80, 109, 114, 124, 125, 127, 134, 140, 143, 386, 387 and 664–674. For very narrow tubes, uncertainties in defining actual diameters (*e.g.*, vdW radius) could significantly affect the reported results. Nominal diameters were used for consistency when inner diameters were not specified in the literature.

velocity discontinuity between the liquid and the solid. The volumetric flow rate with slip, Q ($m^3\ s^{-1}$), is then given by

$$Q = \frac{\pi\left[(d/2)^4 + 4(d/2)^3 L_s\right]}{8\mu L}\Delta P \tag{19}$$

This equation modifies the classical H–P relation to include slip effects; the no-slip classical H–P flow rate, Q_c, is found by setting L_s to zero:

$$Q_{HP} = \frac{\pi(d/2)^4}{8\mu L}\Delta P \tag{20}$$

In experiments, the flow rate enhancement, ε, is defined as the ratio of the measured flow rate Q to the classical H–P flow rate Q_{HP}:

$$\varepsilon = \frac{Q}{Q_{HP}} \tag{21}$$

Thus, the flow rate enhancement ratio can be expressed as a simple function of the dimensions of the CNT and the slip length for infinitely long CNTs:

$$\varepsilon = 1 + \frac{8L_s}{d} \tag{22}$$

This equation is considered valid within continuum length scales (see Fig. 2) and is useful for estimating slip lengths and friction coefficients in experimental analyses, where the viscosity η of water inside CNTs retains its bulk value down to the continuum limit (~1 nm) (see eqn (1)).[1] As the slip length can be expressed as a ratio of the viscosity η and the friction coefficient λ (see eqn (2)), we can also estimate the friction coefficient at the water–carbon surface as:

$$\lambda = \frac{8\eta}{(\varepsilon - 1)d} \approx \frac{8\eta}{\varepsilon d} \tag{23}$$

where the last step assumes that $\varepsilon \gg 1$. However, from a molecular perspective, the classical H–P equations often fail at the nanoscale as they do not account for the variation in fluid viscosity under confinement. MD simulations have demonstrated the spatial viscosity variation

of water confined within CNTs, where water density varies within the interfacial region that typically spans a few water molecules.[75,168,450,472,483,523,528,675–677] Thomas *et al.* introduced a diameter-dependent effective viscosity $\eta(d)$ for the H–P equations, derived from the weighted average of the regional viscosity in CNTs. The effective viscosity is highly dependent on both the water viscosity and the surface area of the interfacial region and the dimensions and viscosity oscillations of the interfacial region remain under investigation. Wu *et al.*[185] reviewed a significant body of both experimental and MD simulation studies and proposed that the critical thickness of the interfacial region for water is ~0.7 nm. Consequently, the modified enhancement factor becomes:

$$\varepsilon = \left[1 + \frac{8L_s}{d}\right]\frac{\eta_\infty}{\eta(d)} \tag{24}$$

Furthermore, simulations indicate substantial slip lengths in CNTs, reaching hundreds of nanometers, that increase further at smaller CNT diameters.[150,168,676,678,679] An empirical relationship for the slip length relative to CNT diameter has been proposed:[168]

$$L_s(d) = L_{s,\infty} + \frac{A}{d^3} \tag{25}$$

where $L_{s,\infty}$ represents the slip length over a flat graphene sheet, and A is a fitting parameter.

6.2.1.2 Enhanced flow and permeance in CNTs. Experimental studies on water transport in CNTs have consistently reported flow rate enhancements on the order of $\varepsilon = 1 - 10^6$ and similarly huge slip lengths ($L_s = 1 - 10^6$ nm) (Fig. 10A and B).[6,24,25,60,64,80,109,114,124,125,127,134,140,143,386,387,664–674] These investigations primarily employed CNT membrane platforms and focused on water flow under hydrostatic pressure gradients.[6,60,109,124,125,127,140,143,386,387,664–673] For instance, Majumder *et al.*[60] explored water flow through free-standing vertically aligned CNT membranes composed of 7 nm diameter CNTs with lengths ranging from 34 to 126 μm. They observed flow rates that were four to five orders of magnitude higher than those predicted by the H–P model, with estimated slip lengths of 40–70 μm. Shortly after, Holt *et al.*[6] studied CNTs with even smaller diameters (1.3–2 nm) and shorter lengths (2–3 μm), reporting flow enhancements of 10^3–10^4 and slip lengths between 300 and 1000 nm. These discrepancies in flow enhancement values reported by these early studies and significant variability in their magnitude highlight some of the experimental challenges in this field that range from difficulties in determining the number of conducting CNTs to variations in their size and chirality. For example, the presence of defects in smaller diameter CNTs can significantly diminish water flow rates,[160,680–682] making fabrication of perfect defect-free micrometer-long CNTs an important but extremely difficult experimental goal.

Qin *et al.*[134] measured water flow through single CNTs with diameters below 2 nm using a field-effect transistor array. They observed flow enhancements between 50 and 1000 in CNTs with diameters ranging from 0.81 to 1.59 nm. Notably, the enhancement factor did not scale linearly with decreasing diameter, as a discontinuity between 0.98 and 1.10 nm indicated a shift from continuum to sub-continuum regimes. However, their calculations, which relied on MD simulations to estimate the driving force from water density inside the CNTs, raise questions about the accuracy of these flow enhancements. Secchi *et al.*[25] used a single-CNT nanojet platform to study CNTs with diameters of 30–100 nm. Their results showed a monotonic non-linear increase in water flow enhancement as CNT diameter decreased. More recently, Cui *et al.*[114] indirectly estimated slip lengths for water flow in CNTs with diameters of 4.6 nm and 5.5 nm to be 21 μm and 17 μm, respectively. However, the calculations were based on ion conductance and electroosmotic flow coupling theory,[205] which can also introduce inaccuracies. A comparison of water transport in ultrashort (~10 nm) CNT porins with 1.5 nm and 0.8 nm diameters found that single-file water configuration in the narrowed sub-1 nm diameter nanotubes produced faster flow.[64,80,176] However, direct comparison of slip lengths values between these experiments and other measurements in long nanotubes is complicated because in these short CNTs, most energy dissipation occurs at the entrances rather than inside the tube.[171] Overall, water permeance of the CNT can be a more meaningful performance metric for nanopore transport than flow enhancement or slip length, as it directly reflects the speed of water transport. On this metric the reported water permeance of 1.5 nm CNT porins (~10^2 LMH per bar) exceeds the values reported by Qin *et al.*,[134] and falls below the values reported for most other experiments with macroscopically-long CNT pores, again highlighting the possible contributions of the CNT porin entrances.

Overall, the reported water permeance values for single CNTs fall in the range of 1 to 10^6 LMH per bar (Fig. 10C), which is up to five orders of magnitude higher than the permeance of state-of-the-art commercial filtration membranes (1–10 LMH per bar).[471,683,684] Although the overall permeability of CNT membranes depends heavily on pore density, which remains relatively low (experimentally reported maximal pore density ~10^{12} tubes per cm^2 (ref. 386 and 389) is still two orders of magnitude lower than the theoretical possible pore density ~10^{14} tubes per cm^2),[685] this permeability advantage highlights potential uses of CNT membranes in filtration applications.[686–688] For instance, Jue *et al.*[386] successfully fabricated large-scale (~60 cm^2) CNT membranes with a pore density of ~1.9×10^{12} tubes per cm^2 using 1.7 nm diameter CNTs, achieving a high overall water permeance of ~200 LMH per bar. Li *et al.*[80] also presented an intriguing prediction that a membrane with only 3% density of sub-nanometer diameter CNT pores could in theory overcome the fundamental trade-off between permeability and selectivity in polymer-based desalination membranes.[689]

The ultrahigh water flow enhancement observed in CNTs has been extensively studied and corroborated through MD simulations.[75,76,150,155,168,184,185,450,483,675,677] While these simulations have provided valuable insights, they have not yet fully aligned with experimental findings, particularly regarding the

huge flow enhancements reported for larger diameter CNTs. For instance, MD simulations suggest that flow enhancement asymptotically stabilizes for CNT diameters greater than ~10 nm, whereas experiments have reported significant enhancement even at diameters up to ~100 nm.[25] Nevertheless, MD studies have made substantial contributions and partially support experimental observations. For example, Thomas[168,169] reported that flow enhancement factors decrease monotonically with increasing CNT diameter beyond 1 nm, attributing to reduced water viscosity and increased slip length on the CNT surface. Similarly, Falk *et al.*[150] linked fast water transport in narrower CNTs to smoother energy landscapes and reduced friction at the CNT surface.

Several theoretical models have been proposed to develop a generalized slip-flow framework for CNTs.[76,150,168,184,185,450,483,675] For example, Thomas *et al.*[168] suggested that continuum hydrodynamics can effectively describe simulated flow rates if both slip length and viscosity are treated as diameter-dependent parameters. An important contribution from Heiranian *et al.*[483] refined the H–P equation using simulated friction and viscosity relationships, which brought the flow enhancement ratios from $\sim 10^3$ all the way to unity and demonstrated how including physics specific to transport under confinement can resolve some of the existing controversies. However, these models had to rely on limited MD data and use linear extrapolations to estimate friction coefficients, viscosity, and slip length. More recently, Aminpour *et al.*[184] introduced a model incorporating interfacial energies to account for the significant experimental data scatter. However, this model was restricted to the continuum regime, applicable only to sufficiently long CNTs with diameters greater than 3 nm. Therefore, a comprehensive and universally applicable model for slip-flow behavior in CNTs still needs to be developed.

6.2.2 CNT ion conductance and charge regulation. Early studies on CNT membranes primarily focused on ion diffusion under pressure or concentration gradients.[5,6,115,125,141,394] However, the advent of single-CNT platforms (Fig. 4) has enabled more precise investigations into ion transport behaviors, generating a wealth of experimental data on CNT ion transport properties. As modern measurement systems allow reliable detection of very small ion currents, ion conductance, G, measurements have emerged as a central parameter for characterizing ion transport and selectivity in CNTs. The ion transport phenomena in CNTs are highly complex and influenced by factors such as CNT geometry, salt concentration, surface charges, and hydrodynamic slippage.[1,35,694] This complexity contributes to the high variability of ion conductance observed across different experiments and underscore the dominant role of CNT wall properties in governing ion transport (Fig. 11 and Table S3, ESI†).[13,64,108,112–114,121–123,126,132,133,136,137,145,146,222,401,692]

6.2.2.1 Ion conductance scaling in CNTs. If we neglect the electroosmotic effects, ionic current in a tubular channel under an applied electric field arises solely from the electrophoretic contribution, as described by the NP equation (eqn (12)). The ion conductance, G, can then be expressed as:

$$G = \kappa_b \frac{\pi d^2}{4L} \tag{26}$$

where $\kappa_b = N_A e \sum_i |z_i| \mu_i c_i$ represents the bulk conductivity of the solution. Here, z_i, c_i, and μ_i are the valence, concentration, and mobility of ions, respectively. N_A is Avogadro's constant, e is the elementary charge, d is the tube diameter, and L is the tube length. For a simple KCl solution with bulk concentration C_0, the bulk conductivity simplifies to $\kappa_b = N_A e C_0(\mu_{K^+} + \mu_{Cl^-})$.

Similarly to water transport, an additional electrical resistance arises from the tube–reservoir interface for ion transport. Hille[695] and Hall[696] analyzed this phenomenon in biological channels, modeling the access resistance as a semispherical cupola. This approach yields the following expression for CNT conductance:

$$G = \kappa_b \left(\frac{4L}{\pi d^2} + \frac{1}{d} \right)^{-1} \tag{27}$$

For CNTs with large aspect ratios ($L \gg d$), the access resistance contribution can be ignored. For uncharged CNTs with fixed geometry, the ion conductance depends linearly on the bulk conductivity (κ_b) and thus on the salt concentration (C_0), such that $G \propto \kappa_b \propto {C_0}^1$ (Fig. 11A).

When the CNT walls are charged, electrostatic interactions alter the ion concentration within the nanotube. This effect is often characterized by electrostatic length scales (Fig. 2). For tubes with $d \gg \lambda_D$ (Debye length), the ion conductance in this "thin" Debye layer regime can be expressed as the sum of bulk (G_{bulk}) and surface (G_{surf}) contributions:[697]

$$G = \kappa_b \frac{\pi d^2}{4L} + \kappa_{surf} \frac{\pi d}{L} \tag{28}$$

where, for KCl solutions in negatively charged CNTs (surface charge density σ, in C m^{-2}), the surface conductivity is $\kappa_{surf} = \kappa_b \sigma \mu_{K^+}/(2eN_A C_0)$. In the opposite "thick" Debye layer limit ($d \ll \lambda_D$), there is no distinction between surface and bulk contributions, resulting in the Debye overlap regime or surface charge-dominated transport regime. In this context, using the PB equation (eqn (10) and (11)) under the Donnan description and local electroneutrality, the conductance becomes:[1,35]

$$G = \kappa_b \frac{\pi d^2}{4L} \sqrt{1 + \left(\frac{2\sigma}{eN_A C_0 d} \right)^2} \tag{29}$$

Both equations (eqn (28) and (29)) predict conductance saturation ($G \propto \sigma$) at low salt concentrations ($C_0 \ll 2\sigma/(eN_A d)$) determined by the surface charge. This regime, characterized by the Dukhin length (eqn (6)), reflects the balance between bulk and surface contributions. For a fixed surface charge density, the conductance becomes independent of concentration (Fig. 11A). At higher ion concentrations, the conductance reverts to a linear dependence on concentration ($G \propto \kappa_b \propto {C_0}^1$).

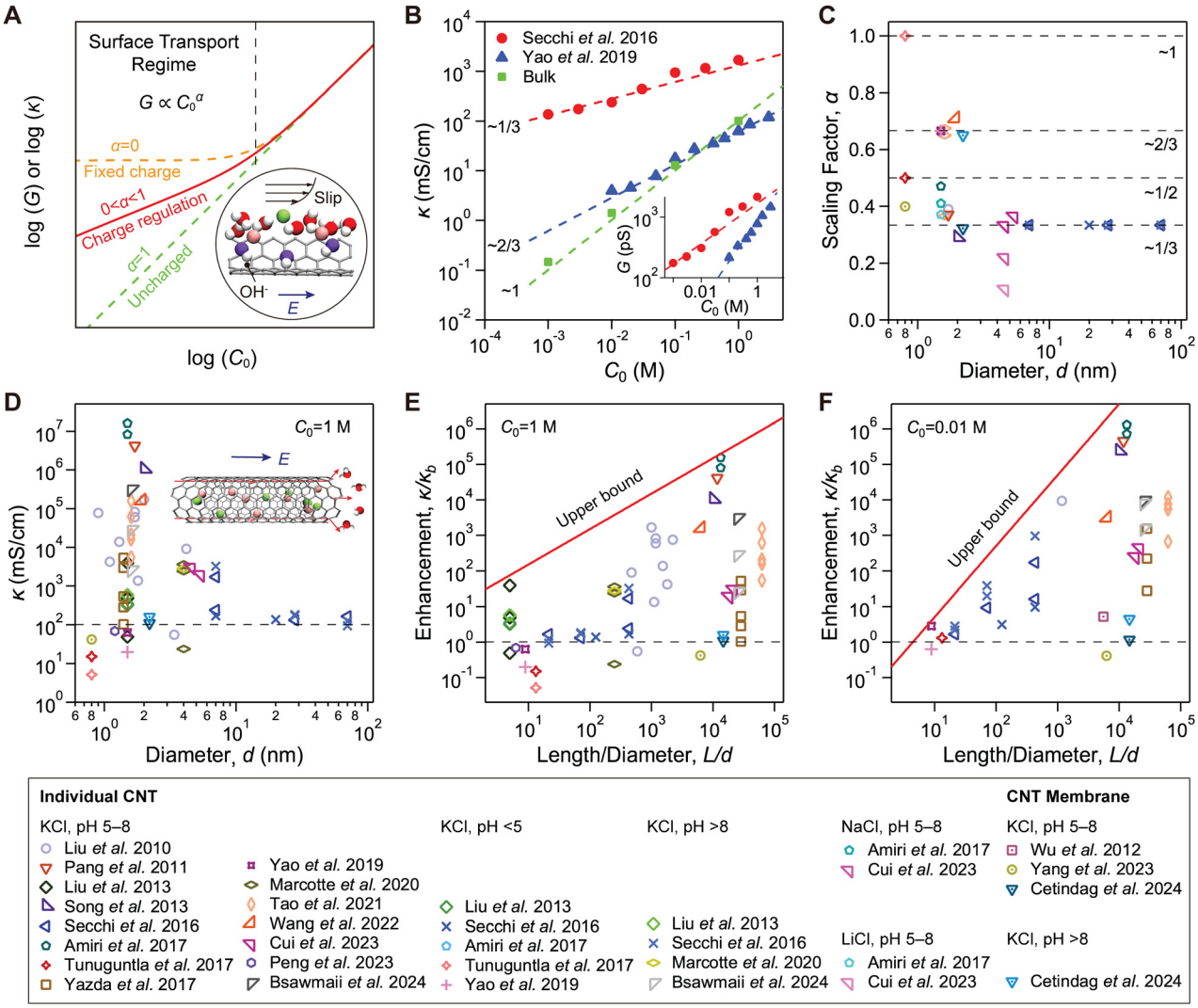

Fig. 11 Ion conductance scaling and enhancement in CNT channels. (A) Schematic representation of ion conductance scaling in CNTs at low salt concentrations. Inset: Ion transport in CNTs under an external electric field, with physisorbed OH^- groups on the surface and coupling with water transport due to hydrodynamic slippage. The inset is inspired from ref. 205 and 690. (B) Ion conductivity and conductance (inset) for 7 nm-diameter micrometer-long CNTs and 1.5 nm diameter short CNT porins. Ion conductivity was calculated from conductance using eqn (27) to account for geometric effects. Data extracted from ref. 136, 145 and 691. (C) Power-law exponent values for ion conductance scaling in CNTs of varying diameters. (D) Ion conductivity in CNTs of different diameters with 1 M KCl solutions. The dashed line corresponds to the bulk conductivity value. Inset: Ion transport in CNTs under an electric field coupled with significant water flow. (E) Ion conductivity enhancement in CNTs *versus* the length-to-diameter ratio for 1 M KCl solutions. The solid line represents the upper bound relation $\frac{\kappa}{\kappa_b} = \gamma\left(\frac{L}{D}\right)^{\beta}$, where γ = 15 and β = 1. (F) Ion conductivity enhancement in CNTs *versus* the length-to-diameter ratio for 0.01 M KCl solutions. The solid line represents the upper bound relation $\frac{\kappa}{\kappa_b} = \gamma\left(\frac{L}{D}\right)^{\beta}$, where γ = 0.05 and β = 2. Data points in panels (C)–(F) were extracted from ref. 64, 108, 114, 122, 123, 126, 132, 133, 136, 137, 141, 143, 145, 146, 401, 674, 692 and 693.

Stein *et al.*[206] observed and analyzed such behavior, where ion conductance scales with bulk concentration at high salinity, but becomes constant at low salinity, in silica nanochannels with fixed surface charges. A similar scaling pattern was later reported in many other nanochannels, including Si_3N_4 nanopores[208] and MoS_2 nanopores.[27] However, early ion conductance measurements in CNTs by the Lindsay group[122,132,137] already revealed a non-constant conductance following a power-law relation ($G \propto C_0^{\alpha}$), with a scaling factor $\alpha \sim 0.3$–0.4 for 1–2 nm diameter CNTs. Subsequent studies by Secchi *et al.*[136] confirmed a similar power-law scaling ($\alpha \sim 1/3$) at low salt concentrations (Fig. 11B), independent of CNT diameter (7–70 nm) and pH (4–10). Yao *et al.*[145] reported yet another scaling behavior in 1.5 nm diameter CNT porins, with $\alpha \sim 2/3$ (Fig. 11B), which they attributed to a combination of electrophoretic and electroosmotic transport. Further experiments revealed prevalent scaling factors for CNT conductance across a wide range of sizes and conditions, predominantly $\alpha \sim 1/3$, $\alpha \sim 1/2$, and $\alpha \sim 2/3$[64,108,114,122,132,136,137,145,146,401,674,692] (Fig. 11C). The most pronounced variations occur in sub-2

nm CNTs, where surface interactions and confinement effects play critical roles, causing fluctuations in the conductance scaling factors. While pH has minimal impact on conductance scaling, the type of salt significantly influences the scaling factor. For instance, Cui *et al.*[114] observed $\alpha \sim 1/3$ for KCl in ~4.6 nm diameter CNTs but lower values for NaCl ($\alpha \sim 1/4$) and LiCl ($\alpha \sim 1/10$). Amiri *et al.*[108] reported a similar trend, with scaling factors following the order KCl > NaCl > LiCl. Power-law conductance scaling has also been observed in other systems, including biological ion channels,[698,699] graphene slits,[700,701] MXene channels,[702] and BNNT porins,[445] although the scaling factors vary widely. Overall, power-law exponents spanning the range $0 < \alpha < 1$ have been documented across many different nanofluidic systems.[703]

6.2.2.2 Surface charge regulation and slippage coupling for ion transport in CNTs. Experimental efforts to understand ion conductance in CNTs have been accompanied by the development of various theoretical models predicting diverse scaling behaviors. Secchi *et al.*[136] proposed an empirical charge regulation model where the surface charge of CNTs depended on salt concentration and led to the scaling relationship $G \propto \sigma \propto C_0^{1/3}$ in the surface-charge-dominated regime. Charge regulation is a common phenomenon in nanoporous membranes with charged or ionizable surfaces;[704–706] however, unlike those channels, CNTs lack obvious sources of permanent charge or acid–base reactivity in water. Researchers hypothesized that surface charge in CNTs may originate intrinsically from OH^- ion adsorption, structural defects (*e.g.* the presence of COO^- groups), or may arise extrinsically through chemical or electrostatic doping from the environment (matrix material that embeds the CNTs, *etc.*). In particular, studies by the Bocquet group demonstrated that CNTs in water develop surface charge through hydroxide ion physisorption (Fig. 11A), influenced by salt concentration.[690,707,708] This process, governed by chemical or adsorption equilibria, can be modeled using the Langmuir adsorption isotherm:

$$\sigma = -e\Gamma_{\text{site}}\frac{e^{\phi_R}10^{\text{pH}-\text{p}K_a}}{1+e^{\phi_R}10^{\text{pH}-\text{p}K_a}} \tag{30}$$

where Γ_{site} is the surface density of dissociable sites, ϕ_R is the surface potential (calculated using the PB equation (eqn (10) and (11)), pH is the solution pH, and pK_a is the surfaces deprotonation reactivity. Using this framework, follow-up studies[136,662,709] identified conductance scaling regimes with exponents $\alpha \sim 1/3$ and $\alpha \sim 1/2$ and quantified transitions between these regimes.

These earlier models, however, neglected the electro-osmotic flow, which occurs when an electric field acts on the charged Debye layer, inducing fluid motion that drags other ions along. The same wall slip, which is responsible for high water transport rates in CNTs, can also enhance electro-osmotic effects, particularly in smaller diameter CNTs.[126,165,327,512] Manghi *et al.*[661] incorporated electro-osmotic effects, surface slip, and charge regulation into a unified model, yielding the following expression for ion conductance:

$$G = \kappa_b\frac{\pi d^2}{4L}\sqrt{1+\left(\frac{2\sigma}{eN_AC_0d}\right)^2} + \frac{\pi d^2}{4L}\frac{\sigma^2}{\eta}\left[\frac{1}{\sigma^*}\left(1-\frac{\ln(1+\sigma^*)}{\sigma^*}\right)+\frac{4L_s}{d}\right], \tag{31}$$

where η is water viscosity, L_s is the slip length, and σ^* is the dimensionless surface charge ($\sigma^* = \pi d\sigma L_B/2e$). The first term represents the electrophoretic contribution, while the second captures electro-osmotic effects and slip contributions. This model predicts multiple scaling regimes, including $\alpha \sim 2/3$, consistent with experimental observations.[145,674,692] Even though the surface charge densities for carbon walls extracted from models are typically low (−5 to −80 mC m^{-2}),[145,205,700] high hydrodynamic slip explains why researchers should always consider contributions from electro-osmotic flow to the transport phenomena in carbon nanotube pores.

Recent studies[703,710] introduced additional phenomena, such as electroneutrality breakdown, which could explain broader scaling exponent ranges ($0 < \alpha < 1$). While the role of electroneutrality breakdown effects in CNT nanofluidics remains a topic of the debate,[710–713] it highlights the complexity of ion transport in CNTs. Further insights may arise from considering the mobility of surface charges. Weakly physisorbed hydroxide ions on CNT walls could in principle translocate along smooth CNT walls, potentially contributing to the measured ion conductance.[205,690,708,714] This dynamic interaction between mobile charges, electro-osmotic flow, and slip-induced enhancements offers rich opportunities for nanofluidic transport modeling.[114,205]

6.2.2.3 Ion conductivity of CNT channels. Based on the concept of mobile charges on CNT walls, the electrophoretic and electro-osmotic contributions to transport, and slippage-induced enhancement of electro-osmosis, ion conductance in CNTs is expected to be significantly enhanced at low ion concentrations and converge to bulk conductance at high concentrations. However, experimental observations reveal a more complex picture. For example, neither 7 nm diameter, micrometer-long CNTs nor 1.5 nm short CNT porins (Fig. 11B) exhibit a clear concentration threshold for such scaling or ever transition to bulk-like conductance behavior at experimentally accessible ion concentration range. Instead, even at 1 M KCl, where the Debye length is ~0.3 nm, ion conductance deviates significantly from bulk conductance. Furthermore, different ion conductance values have been reported for CNTs of similar diameters.[122,123,126,401] For instance, Liu *et al.*[122] reported that ion conductance in individual 1–2 nm diameter CNTs varied over nearly four orders of magnitude. Similarly, Marcotte *et al.*[126] measured three individual 4 nm diameter CNTs from the same batch, reporting conductance values of 0.03 nS, 4.5 nS, and 3 nS, respectively.

We have compiled ion conductance data from various studies, presenting them as ion conductivity to eliminate channel geometry effects (Fig. 11D–F). Enhanced ion transport has been consistently observed across experiments using CNTs

of different lengths and diameters, though the degree of enhancement varied significantly. For sub-1 nm CNTs, ion transport is hindered by confinement effects and ion dehydration barriers. CNTs with diameters of 1–2 nm show the largest fluctuations in the ion conductivity distribution. For CNTs larger than 2 nm, conductance contributions from surface transport become less significant. Just as with the data on water transport of CNTs, a general trend emerges: CNTs with high length-to-diameter ratios exhibit the greatest ion conductivity enhancements, both at 1 M KCl and 0.01 M KCl (Fig. 11E and F). Notably, the conductivity enhancement demonstrates an upper bound, with no data points appearing in the upper-left region of the plot (*i.e.*, no CNTs with small aspect ratios show high conductivity enhancements). This empirical boundary line provides a rough cap on the observed data and highlights a pattern that has not been widely discussed in the literature. At this point it is hard to assign a definitive physical explanation to this phenomenon. We do note that this effect likely originates from using the macroscale channel conductance formalism to evaluate ion conductivity, which does not take into account surface transport, reduced friction at the CNT walls and enhanced electroosmotic coupling. All these processes should drive the length scaling of the channel conductance to a sub-linear behavior, causing the calculated conductivity to display a general trend similar to those in Fig. 11E and F. These data also point to an existing knowledge gap in our understanding of ion conductance scaling with the channel length, with the current measurement platforms providing access to either ultrashort (<10 nm) or macroscopically-long (>1 μm) CNTs, and hardly any measurements addressing the channel lengths in the ~100 nm intermediate length range.

6.2.3 CNT chirality and ion and water transport properties. In earlier sections, we discussed the role of wall slip and surface charges of CNTs in transport processes; however we have not addressed the role of the electronic properties of the CNT walls. Different CNT chiralities (Fig. 3) could in principle lead to distinctive variations in the polarization interactions of water molecules and ions with the channel walls, which could then influence water and ion transport.[69,71,73,552,553] Indeed, this idea is reinforced by the observation that polarization interactions between a narrow CNT wall and small K^+ ions can produce extraordinary stabilization that enables those ions to enter the extremely narrow CNTs (Fig. 6C).[69,553] However, because of the experimental difficulties associated with obtaining pure chirality-defined CNT channels, existing literature on the impact of CNT electronic properties on water and ion transport is sparse and often presents conflicting findings.[113,122,123,176] Surprisingly, even the simulations literature contains some conflicting findings regarding the role of CNT wall electronic properties.[170,485,554,594,715] In this section, we take a closer look at the concept of electronic polarization in CNTs and review some studies that have begun to uncover how chirality influences ion and water transport at the nanoscale.

6.2.3.1 Electronic polarization effects at CNT walls. Electronic polarization effects describe the deformation of the electronic clouds induced by the presence of nearby charged ions and polar molecules.[551,716] Notably, confinement in nanofluidic channels can enhance these interactions by removing layers of water molecules that would ordinarily screen the electric fields. For instance, the polarizable force field model developed by Misra and Blankschtein illustrates how partially dehydrated ions and water molecules inside narrow CNT pores can induce strong polarization in the CNT electronic structure (Fig. 12A).[69,176,717] A more complex AIMD simulation also reveals similar effects for protons placed in CNT pores[176,718] (Fig. 12A). Interestingly, these simulations suggest that

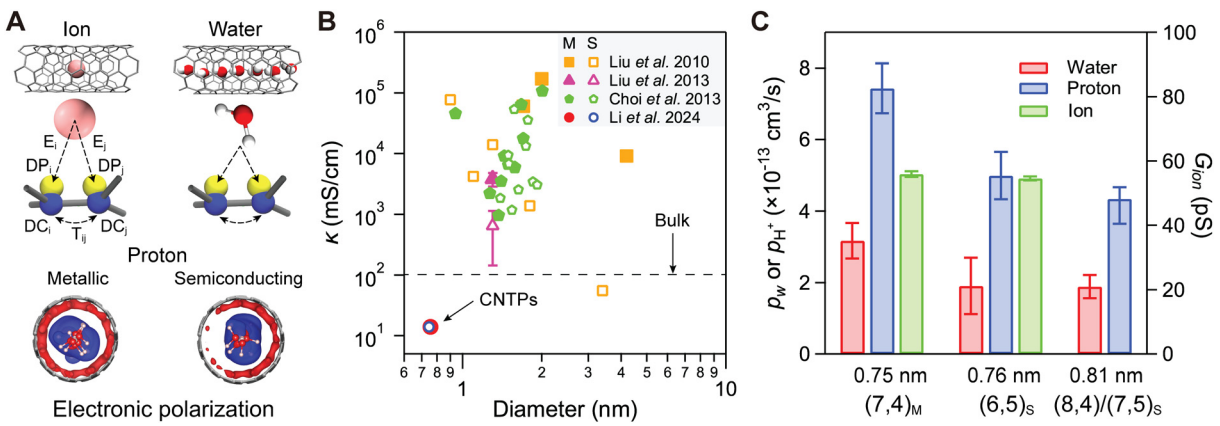

Fig. 12 Electronic properties of CNTs and their influence on molecular transport. (A) Top: Schematic representation of electronic polarization in CNTs induced by water or ions. The induced dipole moment on carbon atoms is modeled using a pair comprising a Drude particle (DP, representing the carbon electron cloud) and a Drude core (DC, representing the carbon nucleus). DCs and DPs interact electrostatically *via* the dipole field tensor T_{ij}. Bottom: Electronic polarization maps for a water wire containing an excess proton inside a CNT. Adapted from ref. 176 with permission from Springer Nature Limited, copyright 2024. (B) KCl (1 M) conductivity of CNTs with varying chirality and diameters. Ion conductivity was calculated from conductance using eqn (27). Data were extracted from ref. 113, 122, 123 and 176. For ref. 113, ion conductivity was estimated based on K^+ ion mobility derived from the dwell times of ion translocation, assuming continuous ion flow through CNTs with this mobility. (C) Water and proton permeability, as well as ion transport, in single-file, chirality-pure CNT porins. Data were extracted from ref. 176.

polarization is weaker in semiconducting CNTs, where a non-symmetrical charge distribution causes protons to gravitate closer to the CNT wall, while metallic CNTs exhibit stronger polarization with a more symmetrical distribution. These examples also point to the increasing importance of using self-consistent electric field models for water, ions, and protons for realistic simulations of nanofluidic transport.

The physical picture is also complicated by the highly anisotropic polarizability characteristics of CNTs:[719] radial polarizability scales with the CNT radius, whereas axial polarizability is inversely related to the bandgap, making metallic CNTs more axially polarizable than semiconducting ones.[719–721] The axial component is generally larger in metallic tubes, while the radial component remains independent of the bandgap.

Finally, we note that CNTs can also polarize confined molecules, influencing the electronic properties of water and other confined liquids.[69,71,73,176,554] DFT calculations[485] show that CNTs with varying chiralities have distinct partial charges at their ends, resulting in different orientations of water dipoles. Simulations indicate that water molecules confined within CNTs have reduced dipole moments: while dipoles near the center retain bulk-like values, those close to the CNT wall show lower values due to disrupted hydrogen bonding.[722,723] These effects, coupled with the general reduction of dielectric screening in very thin water layers lead to lowering of the local dielectric constant at the CNT interface compared to bulk water.[7,61,564,576,724–726] The vibrational properties of confined water also shift at the CNT–water interface, influenced by fluctuations in electronic charge density.[727,728]

6.2.3.2 Molecular transport enhancement in metallic CNTs. Several earlier MD simulations provided some insights into these behaviors, suggesting that water diffuses more readily in metallic CNTs than in semiconducting ones,[485,594] while CNT chirality has minimal impact on ion transport.[594] However, other MD studies show higher ion transport in metallic CNTs,[715] while others predict faster water transport in semiconducting CNTs.[170] Two early experimental studies[122,123] reported significantly higher ion conductance in metallic CNTs (Fig. 12B and Table S3, ESI†) without fully explaining the underlying mechanisms or specifying CNT chiralities. Lindsay and co-workers measured ion transport in micron-long CNTs using a horizontal single-CNT platform under applied voltages, observing that metallic CNTs exhibit ion conductance over an order of magnitude higher than semiconducting CNTs, the effect that they attributed to electroosmotic flows from trapped CNT charges.[122] Wu and co-workers studied ultrashort CNTs (5–10 nm in length and 1–2 nm in diameter) on a BLM-supported CNT platform and reported up to an order of magnitude higher ion conductivity in metallic CNTs.[123] In contrast, other experiments on micrometer long CNTs of 1–3 nm diameter have shown no clear correlation between chirality and transport efficiency.[113,692]

Noy and co-workers recently reported a systematic examination of the impact of electronic properties on single-file CNT transport efficiency using the CNT porin platform.[176] These researchers isolated metallic nanotubes (7,4) with a 0.76 nm diameter and semiconducting nanotubes ((6,5) and a (7,5)/(8,4) mix) with diameters of 0.75 and 0.81 nm *via* aqueous two-phase separation,[21,174,175,243,729] which allowed them to synthesize CNT porins with identical diameters but different metallicity. Under these highly controlled experimental conditions metallic CNT porins showed nearly 70% higher water permeability than semiconducting ones (Fig. 12C). At the same time, measured ion permeabilities of metallic and semioconducting CNTs were statistically indistinguishable. Control experiments also showed nearly identical water permeability for the larger (0.81 nm) and smaller (0.75 nm) semiconducting CNT porins (Fig. 12C), suggesting that it was the bandgap, rather than diameter, that was responsible for the differences in water permeability. Metallic nanotubes also showed a 50% increase in proton conductivity over semiconducting ones of similar size, with diameter variations playing a similarly minor role. In close agreement with experiments, polarizable force field-based MD simulations indicated that water molecules are more stabilized by tube polarization in metallic CNT porins, while ion polarization was less affected by electronic properties.[176] These simulations showed that charge screening for ions depends on radial polarizability, while dipole screening for water involved both components. For proton transport, AIMD simulations suggested that asymmetrical polarization in semiconducting CNTs pulls protons closer to the wall, creating a more complex path, whereas metallic CNTs provide a straighter, more efficient route.[176] These results also firmly establish the channel wall electronic properties as one of the important control parameters for nanofluidic transport.

6.3 Transport phenomena dominated by CNT entrances

Another critical barrier that determines the transport properties of CNTs is the entrance region, where the transition from a bulk reservoir to a nanoconfined interior occurs. This transition introduces additional resistances, such as pressure losses in hydrodynamic flow[730,731] and access resistance in ion conductance,[696,732] which can significantly affect transport efficiency. Functional groups at the CNT entrances can further shape transport behavior by mediating molecular interactions. Hydrophilic or hydrophobic functionalization can either enhance or impede flow,[64,124,125,667,685] while charged groups generate electrostatic potentials that selectively attract or repel ions facilitating ion selectivity.[64,115,127,133,394,401] In CNTs with very small diameters, entrance regions play a prominent role because of the molecular rearrangement processes that occur there. Water molecules must reorganize their hydrogen-bonding networks to fit within the CNT,[80,164] while ions must partially shed their hydration shells to enter the channel.[81] The energy barriers associated with this dehydration process vary among ions, enabling selective ion transport based on factors such as size, charge, and hydration energy. The entrance region thus serves as a critical gatekeeper, sometimes dictating the efficiency and selectivity of nanofluidic transport.

6.3.1 Entrance effects and water transport in CNTs. Entrance effects influence the efficiency of water transport through CNTs,[35,64,75,76,124,125,164,171,184,388,450,482,483,540,541,667,675,685,733–735] and become increasingly pronounced for smaller CNTs.[64,164,171,176] Some general strategies to mitigate these entrance and exit losses include optimizing the structure of CNT openings to facilitate smoother transitions,[482] for example, by mimicking the hourglass-shaped pore entrance found in AQPs.[736] Another approach, functionalization of CNT ends with chemical groups can introduce additional complexity,[64,124,125,388,667,685,734] and can, generally, influence the transport efficiency both ways depending on the nature of the functional groups.

6.3.1.1 Entrance and exit losses for water transport through CNTs. The H–P relations (eqn (18)–(20)) assume $L \ll d$, implicitly neglecting the effect of CNT entrances on the flow rate. Even in a continuum representation the transition from a macroscopic reservoir to a CNT introduces additional viscous dissipation, as streamlines must bend for the fluid to enter the CNT. These entrance effects can be modeled by considering the flow through an infinitely thin nanopore. The problem was addressed by Sampson[730] and later by Weissberg[731] who obtained the expression for the flow rate through a nanopore with vanishing length as:

$$Q_e = \frac{(d/2)^3}{C\eta\Delta P} \tag{32}$$

where C is a numerical prefactor ($C = 3$ in Sampson expression for very short tubes). As tube length increases, C may vary.[25,171,675,679,731,736] In the no-slip scenario, the entry flow profile resembles a combination of the parabolic profile of Poiseuille flow and the elliptic profile from Sampson's solution,[730] transitioning smoothly to a parabolic profile inside the channel with minimal energy loss. With perfect slip, despite similar entry profiles, the transition to a plug profile inside the tube necessitates substantial streamline reorganization (Fig. 2D), introducing additional dissipation and increasing the value of the parameter C. For instance, reports[25] indicate that C can rise to $\sim$3.6 for CNTs of $\sim$0.5–1 μm in length and $\sim$30–100 nm in diameter, showing that transitioning from no slip to perfect slip significantly boosts entrance resistance.

To estimate the flow rate through a CNT by accounting for entrance effects, we may add the hydrodynamic resistances of the entrance regions and the middle part of the CNT, giving us the "Hagen–Poiseuille–Weissberg" (H–P–W) equation with slip:

$$\Delta P = \frac{\eta C Q}{(d/2)^3} + \frac{8\eta L Q}{\pi[(d/2)^4 + 4(d/2)^3 L_s]} \tag{33}$$

The flow rate enhancement ratio (eqn (21)) is then expressed as a simple function of the dimensions of the CNT, the slip length, and the pressure entry/exit losses:

$$\frac{1}{\varepsilon} = \frac{1}{1 + \frac{8L_s}{d}} + \frac{C\pi}{16}\frac{d}{L} \tag{34}$$

The enhancement factor, ε, can thus be divided into two contributing terms: surface slippage (first term) and entrance/exit effects (second term). The first term is independent of CNT length, suggesting that slippage will increasingly dominate the enhancement value in longer CNTs. If water transport is primarily influenced by the entrance/exit losses and the slip flow effects are negligible, ε should show a positive correlation with L/d:

$$\varepsilon = \frac{16}{C\pi}\frac{L}{d} \tag{35}$$

Interestingly, when we plot the enhancement factor values (ε) against the aspect ratios (L/d) of CNTs (Fig. 10D), they indeed exhibit a positive correlation with L/d for most reported CNTs, suggesting that the second term (entrance effects) dominates over the first term even in micron-long CNT.

Entrance losses are also often overlooked when calculating apparent friction coefficients (λ) using eqn (23). Experimental data show a linear decrease in the logarithm of apparent λ values with the CNT length, L (Fig. 10E). Clearly, the true value of λ, which depends solely on the nature of the water–carbon interface, cannot vary by more than seven orders of magnitude; therefore, the observed decline in λ must reflect the diminishing influence of the entrance/exit effects on the overall transport. If we attribute the CNT water flow resistance entirely to the entrance/exit losses and combine eqn (35) with eqn (23), the apparent friction coefficient λ can be written as

$$\lambda \approx \frac{\pi\eta C}{2L} \tag{36}$$

This form is consistent with the data shown in Fig. 10E (dashed lines). Notably, the lowest λ value ($\sim$1 Pa s m^{-1}) still represents an upper limit for the water transport in CNTs, as we do not see the data reaching a plateau even in centimeter-long CNTs, leading to the astonishing conclusion that the intrinsic water–carbon friction in CNT pores may be so low that the entrance effects may still remain significant even at the macroscopic scale.

As described in the prior sections, in sub-1 nm nanotubes water molecules arrange in a single-file chain, losing approximately two hydrogen bonds compared to their configuration in bulk water. Several factors compensate for the energy cost of this loss:[164,589] stronger remaining hydrogen bonds, favorable vdW interactions with the CNT walls, and the rotational entropy of the unbound OH bond. Indeed, experiments and simulation studies reveal a surprisingly low activation energy of $\sim$4–6 kcal mol^{-1} for water transport through these CNTs (Fig. 7A).[80] For very short length ($\sim$10 nm) of single-file CNT porins, where most dissipation occurs at the entrances, classical hydrodynamic predictions of entrance/exit losses (eqn (32) and (33)),[730,731] which state that water permeability scales with the cube of the CNT diameter, break down. Complex structural rearrangements of water inside small CNTs, as well as the dependence of water permeability on the electronic nature of the CNT pores (Fig. 12C), are partially responsible for water–carbon friction no longer being governed solely by fluid viscosity in CNTs pores.

6.3.1.2 Water transport and CNT pore chemical functionality. For relatively larger CNTs, MD simulations[667,685,734] predict that functional groups at the CNT entrances can significantly reduce the water flow rate. This reduction arises from several aspects. First, steric blockages caused by the functional groups reduce the effective cross-sectional area available for water molecules to pass through. Second, stronger and more localized electrostatic interactions between water molecules and charged or polar functional groups at the entrance slow down water transport. Unlike the weak vdW interactions with uncharged carbon atoms inside the CNT, these interactions cause water molecules to temporarily reside in energetically favorable positions near the functional groups, slowing the overall transport.[734] In the more extreme cases, functionalization inside the CNT pore can increase the channel surface roughness, disrupt the wall slip and even cause a transition to a parabolic flow profile.[200]

Interestingly, experimental studies report varying observations regarding the effects of CNT functionalization. Majumder *et al.*[125,667] presented an elegant experiment where functionalizing 7 nm diameter CNTs with hydrophilic polypeptide linkages containing negatively charged SO_3^{2-} groups reduced the flow enhancement from $\sim 10^4$ to $\sim 10^2$. In contrast, Lokesh *et al.*[124] reported that functionalizing 2.2 nm diameter CNTs with octadecylphosphonic acid increased water permeability by a factor of 3. One explanation for this discrepancy could be that Lokesh *et al.*'s modifications were made on the CNT membrane surface rather than directly inside the CNT channels.

Typically, open CNT pores contain COO^- groups at their entrances. For 7 nm diameter CNTs, these COO^- groups impart sufficient hydrophilicity to facilitate water entry into the CNT core without significantly hindering rapid flow.[125] However, Tunuguntla *et al.*[64] showed that protonating these COO^- groups by lowering the pH from neutral to pH 3 further increased water permeability by a factor of five (Fig. 7B). This observation agrees with the predictions from MD simulations,[667,685,734] again highlighting the important role that entrance chemistry can play in modulating water transport in small-diameter CNTs.

6.3.2 Donnan selectivity in larger CNTs. Ion selectivity in nanochannels generally arises from two primary mechanisms: electrostatic interactions (stemming from surface charges within the channel or at the membrane interface) and steric repulsion (governed mainly by ion dehydration energies) (Fig. 2). In relatively large channels where dehydration effects are minimal, Donnan exclusion represents the dominant mode of ion selectivity.[1,15,44,46,737,738] For CNTs, the intrinsic surface charge tends to be weak,[136,661,662,708] allowing the COO^- groups at the pore mouth to play the central role[108,115,394,739] at neutral pH or higher pH (Fig. 13A).[64,108,125,133,143,145,674] Relatively high chemical reactivity of these COOH groups should also allow researchers to tune CNT selectivity by functionalizing these groups;[151,154,396,685,740–742] however, such strategies remain largely confined to simulations, with only limited experimental validation reported to date.[5,124,327,331,743] It is also suggested that entrance charge functionalization generally enhances both ion conductance and selectivity in CNTs,[24,64,108,133,136,141,145,401,674] unless excessive crowding or overscreening occurs.[64,108,401,744] Therefore, careful optimization of functionalization is necessary to tune CNT transport performance.

Researchers used several experimental approaches to quantify ion selectivity of CNT pores.[46,745] Ion rejection measurements under pressure-driven flow experiments[24,115,119,127,386,394] reveal salt-specific exclusion behavior. Reversal potential experiments[64,108,114,133,143,145,674] provide insight into the selectivity between anions and cations. Single-channel conductance measurements,[108,113,121] where one ion species is held constant and the other is varied, also enable the ion selectivity quantification. Likewise, single-ion diffusion experiments[5,81,125,325] under concentration gradients also can track the permeability of specific ions under controlled conditions.

6.3.2.1 Salt rejection in CNTs. When CNT membranes are used in pressure-driven nanofiltration experiments, the salt rejection coefficient, R_c, represents a key metric for evaluating both filtration performance and ion selectivity. R_c is defined as:

$$R_c = 1 - \frac{C_p}{C_f} \tag{37}$$

where C_f is the feed-side salt concentration and C_p is the permeate-side concentration. Fornasiero *et al.*[115] demonstrated that selective transport in sub-2 nm CNT membranes arises primarily through a Donnan-type exclusion mechanism based on electrostatic interactions with COO^- groups at the CNT entrances. According to Donnan theory, when a charged membrane contacts an ionic solution, co-ions are partially excluded. This charge-based partitioning enriches counterions in the membrane phase while depleting co-ions, creating a Donnan potential at the solution/membrane interface. Under a pressure gradient, the Donnan potential repels co-ions; yet, because of electroneutrality requirements, the counterions bound to those co-ions must also be rejected, thus enabling the membrane to reject salt.

For a single-salt solution, Donnan theory gives the rejection coefficient as:[115,746]

$$R_c = 1 - \frac{c_i^m}{c_i} = 1 - \left(\frac{|z_i|c_i}{|z_i|c_i^m + c_x^m}\right)^{|z_i/z_j|} \tag{38}$$

where c_i and c_i^m are the concentrations of the co-ion in the bulk solution and within the membrane, c_x^m is the fixed-charge concentration of the membrane, and z_i and z_j are the valences of the co- and counterions, respectively. This model also reflects the dependence of ion exclusion on the Debye length (λ_D), recalling $c_i \sim \lambda_D^{-2}$. When λ_D is substantially larger than the CNT diameter, co-ions are strongly repelled. Another prediction is that ion valence and charge profoundly affect Donnan exclusion: for a negatively-charged membrane highly-charged anions are more effectively rejected, whereas high-valence cations screen those membrane charges more efficiently and thus facilitate anion permeation.

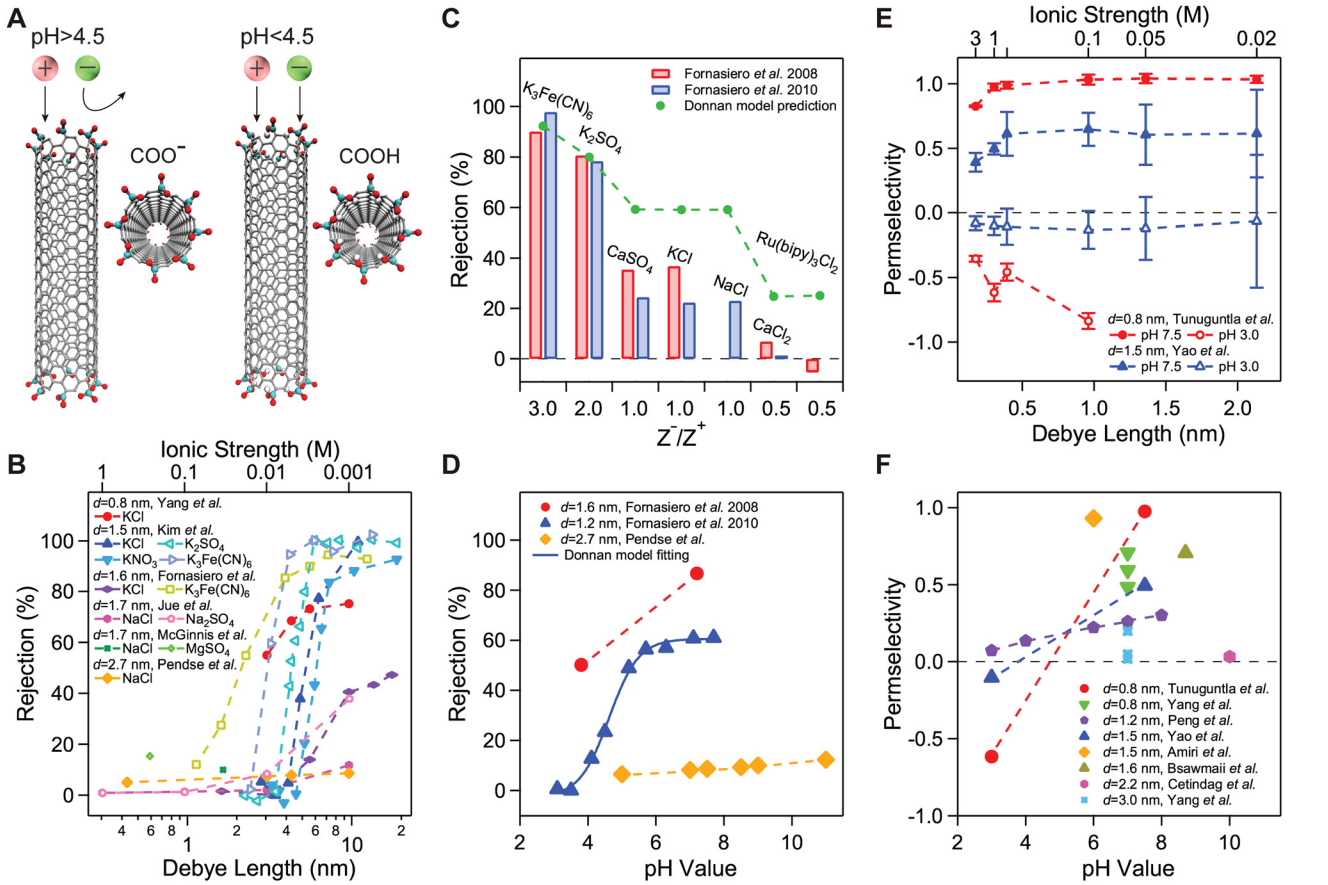

Fig. 13 CNT entrance charges and CNT ion selectivity. (A) Schematic of pH-switchable ion selectivity in CNTs with COO^- groups at the entrances. Above the pK_a (~4.5), the COO^- groups remain negatively charged, and below the pK_a they protonate, becoming uncharged COOH groups. (B) Salt rejection by CNTs as a function of Debye length and salt ionic strength in pressure-driven filtration experiments. Ionic strength (I) is given by $I = \frac{1}{2}\sum_i C_i z_i^2$, where C_i is the ion's molar concentration and z_i its valence. Data were extracted from ref. 24, 115, 119, 127, 143 and 386. (C) Rejection coefficients (bars) for salt solutions of the same equivalent concentration but differing ion valence. Filled circles represent rejections calculated using the Donnan theory (eqn (38)). Salt concentrations were 0.5 mM for all solutions, except for KCl (1.0 mM) and $K_3Fe(CN)_6$ (0.3 mM). Data were extracted from ref. 115 and 394. (D) Effect of pH on salt rejection by CNT membranes. Dashed lines are visual guides. The blue solid line is a fit to experimental data using the Donnan model (eqn (38) and (39)), yielding a pK_a of 4.8 for the charged groups. Data were extracted from ref. 24, 115 and 394. (E) Ion permselectivity in 0.8 nm and 1.5 nm diameter CNT porins as a function of Debye length and solution ionic strength in reversal potential measurements (high concentration side). Dashed lines are visual guides. Data were extracted from ref. 64 and 145. (F) K^+/Cl^- ion permselectivity of CNTs with varying diameters in solutions of differing pH. The high concentration side in reversal potential measurements was 1 M KCl. Dashed lines are visual guides. Data were extracted from ref. 64, 108, 133, 143, 145, 674 and 693.

Experimental findings from CNT membrane studies corroborate the Donnan exclusion-based predictions (Fig. 13B and C), demonstrating that ion permeation can be regulated by modifying the ionic strength, ion valence, or CNT diameter, all of which affect the electrostatic screening of CNT surface charges. Sub-1.5 nm CNT membranes, for instance, can achieve nearly 100% salt rejection at very low ionic strengths (<10 mM)[115,119,143,386] (Fig. 13B). However, once the Debye length λ_D becomes smaller than the CNT diameter, electrostatic exclusion drops rapidly, reducing rejection to only a few percent. Accordingly, CNTs wider than 2 nm usually exhibit below 20% rejection at salt concentrations of 1 mM,[24] and even sub-1.5 nm CNT membranes lose their high rejection performance when the salt concentration reaches 100 mM.[115,119,127,143,386] Moreover, experimental measurements reveal that increasing the ratio $|z^-/z^+|$ further enhances rejection[24,115,394] (Fig. 13C), again showing that larger anion valences intensify electrostatic repulsion at the negatively charged CNT entrance, while cation valences mediate screening and reduce this repulsion.

An additional key prediction of the Donnan model is the dependence of salt rejection on solution pH that arises from the pH-dependent ionization of COOH groups at the CNT entrance (Fig. 13A and D).[24,115,394] Above the pK_a of these groups, more carboxyl sites become deprotonated (COO^-), thus amplifying electrostatic exclusion. Fornasiero *et al.*,[115,394] for example, observed notably high salt rejection at pH values above 5 (Fig. 13D). The membrane's fixed charge concentration can be described by the standard titration relationship:

$$c_x^m = c_{x,0}^m \frac{10^{-pK_a}}{10^{-pK_a} + 10^{-pH}} \quad (39)$$

where $c_{x,0}^m$ is the fully ionized charge density. Applying eqn (38)

and (39), the resulting best-fit pK_a ≈ 4.8, is in excellent agreement with the known pK_a ∼ 4.5 of carboxylic acid,[747,748] which strongly indicates that, for CNTs, the negative charges responsible for ion exclusion indeed arise from ionized COO^- groups at the CNT entrances.

Although Donnan equilibrium theory successfully describes general trends, experimental salt-rejection data sometimes deviate from its predictions (Fig. 13B–D). For instance, Donnan theory neglects the effects of applied pressure, which can increase salt rejection by driving a higher water flux relative to ion flux or decrease the salt rejection due to ionic concentration polarization at high water fluxes.[24,386] Moreover, it does not account for negative rejections observed experimentally (Fig. 13C),[23,115,119,394] where elevated salt concentrations reduce rejection *via* increased osmotic pressure and enhanced water diffusion.

6.3.2.2 Ion selectivity in CNTs. In addition to pressure-driven experiments that quantify the overall salt rejection of CNTs, reversal potential measurements,[48,745] where the two sides of CNTs are exposed to different salt concentrations, provide more granular insights into CNT ion selectivity (whether they favor cations or anions). In these experiments, the concentration gradient drives both cations and anions from the high-concentration side to the low-concentration side. For transport in CNTs, negatively charged COO^- groups at the CNT entrance are expected to promote cation selectivity at neutral or higher pH (Fig. 13A). The reversal potential, V_{rev}, which is defined as the voltage at which the net ion current across the CNTs is zero after accounting for the redox potential of the electrodes, is governed by the Goldman–Hodgkin–Katz (GHK) equation,

$$V_{rev} = (2t_+ - 1)\frac{RT}{F}\ln\left(\frac{\gamma_h C_h}{\gamma_l C_l}\right) \quad (40)$$

where R is the gas constant, T is the absolute temperature, F is the Faraday constant, C_h and C_l are the salt concentrations on each side of the CNT, and γ_h and γ_l represent the salt activity coefficients.[691] The parameter t_+ is the cation transference number, *i.e.*, the fraction of total ion flux carried by cations. Hence, $t_+ = 1$ corresponds to completely cation-selective behavior, while $t_+ = 0$ corresponds to purely anion-selective behavior. The cation/anion selectivity ratio, SR, can be calculated as

$$SR = \frac{t_+}{1 - t_+}. \quad (41)$$

Additionally, the ion permselectivity P_s, which normalizes the selectivity in CNTs against that in the bulk, is given by

$$P_s = \frac{t_+ - t_{+bulk}}{1 - t_{+bulk}}, \quad (42)$$

where $t_{+bulk} \approx 0.49$ for the commonly used KCl electrolyte.

In general, strong ion selectivity arises when the screened surface-charge length scale (the Debye length, see eqn (4)) is comparable to the physical dimensions of the CNT, and it increases with higher charge density on the CNT walls. Hence, CNT ion selectivity is predominantly determined by the pH, the CNT diameter, and the salt concentration (which in turn affects the Debye length). When the pH is above 5, COO^- groups at the CNT entrance present negative charges. If the Debye length exceeds the CNT diameter, overlapping EDLs near the CNT entrance can effectively block anion transport. Conversely, if the Debye length is smaller than the CNT diameter, electrostatic interactions decay more quickly, leading to reduced ion selectivity. Overall, higher pH (increasing negative charge at the CNT entrance), smaller CNT diameter, and lower salt concentrations (leading to thicker EDLs) collectively enhance cation selectivity[64,108,133,143,145,674] (Fig. 13D and E).

Yao *et al.*[145] studied 1.5 nm-diameter CNT porins and observed weak K^+ selectivity over Cl^-, with a permselectivity of ∼0.5. This selectivity decreased slightly when the KCl concentration exceeded 0.6 M, since the entrance COO^- groups became strongly screened. At pH 3.0, these wider CNT porins lost their selectivity (*i.e.*, permselectivity approached zero). Notably, these 1.5 nm CNT porins exhibited strong pH dependence, confirming that the COO^- groups at the pore rim were chiefly responsible for selectivity at neutral pH. This conclusion was further supported by measurements on ∼1.2 nm-diameter CNTs at multiple pH levels[133] (Fig. 13F). The selectivity difference between the 0.8 nm and 1.5 nm CNT porins at the same pH can be attributed to the Debye length relative to CNT diameter. At a given concentration, as the CNT diameter increases, the extent of EDL overlap diminishes, reducing cation selectivity. Yang *et al.*[143] recently reported similar observations: 0.8 nm CNT membranes exhibit much higher ion selectivity than membranes with 3 nm CNTs where selectivity becomes extremely weak in 3 nm CNTs at pH 7.[143] Furthermore, 2.2 nm CNTs were found to exhibit essentially no selectivity at pH 10,[674] even though the CNT entrance under such alkaline conditions is expected to be highly charged.

6.3.3 Dehydration-dominated and polarization-dominated selectivity in smaller CNTs. Tunuguntla *et al.*[64] demonstrated that 0.8 nm CNT porins at pH 7.5 conduct K^+ almost exclusively, achieving ∼0.99 permselectivity over Cl^- (corresponding to a K^+/Cl^- selectivity ratio SR of ∼200). Crucially, narrow CNT porins retain this high selectivity at very high salinities up to 1 M (where the Debye length is only 0.3 nm) (Fig. 13D). In this case, unlike the Donnan exclusion-driven selectivity of the larger CNT pores, the selectivity is largely driven by the combination of ion dehydration barriers and the compensating polarization interaction of the partially dehydrated ions with the CNT walls.[69,81]

Unlike the larger diameter CNTs, the selectivity of CNTs with inner diameters below 1 nm, which are smaller than the typical hydrated ion diameter, is strongly influenced by ion dehydration barriers (Fig. 14A), an energetically demanding process. Since CNTs lack the sophisticated functional group arrangements found in biological ion channels that can assist in dehydration,[154,158] the activation energy associated with this process is expected to closely track the intrinsic strength of the ions hydration shell. Because different ion species have distinct hydration radii and coordination preferences, these mechanisms can result in pronounced ion selectivity.[81–84,158,167]

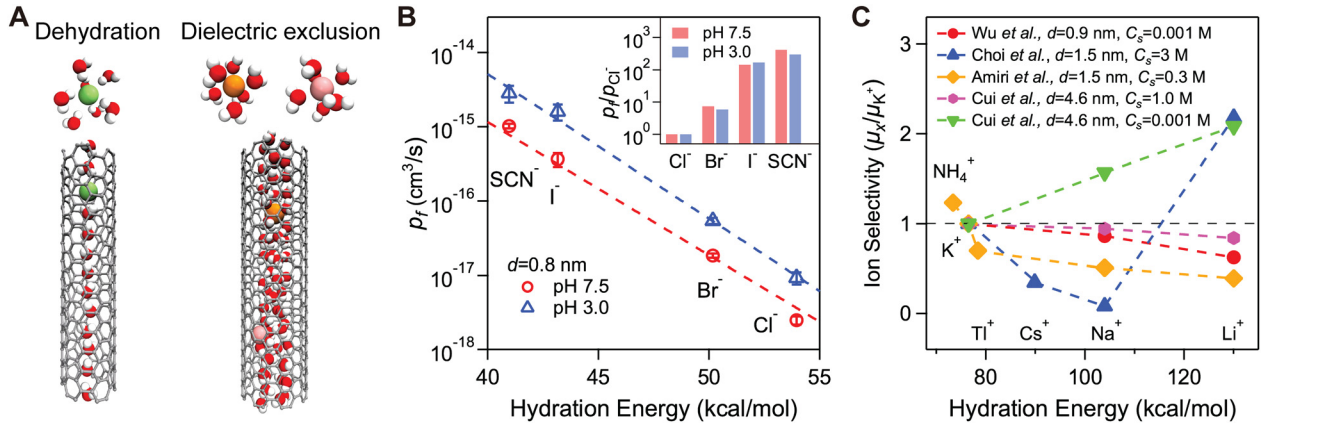

Fig. 14 Dehydration effects on ion selectivity in small-diameter CNTs. (A) Schematic representation of ion hydration during transport through small CNTs (single-file or sub-2 nm). The energy barrier for ion transport may arise from dehydration, dielectric exclusion, or differing hydration states within CNTs. (B) Measured anion permeabilities in 0.8 nm diameter CNT porins as a function of first solvation shell hydration energies, calculated from first-principles simulations. Dashed lines represent exponential fits. Inset: Ion selectivity of various anions relative to Cl^-. Adapted from ref. 81 with permission from American Chemical Society, copyright 2020. (C) Cation selectivity relative to K^+ ions in small-diameter CNTs (calculated based on single CNT conductance or ion mobility). Dashed lines are visual guides. Data were extracted from ref. 108, 113, 114, 141 and 752.

Li *et al.*[81] investigated the diffusion of monovalent halide anions through single-file CNT porins under concentration gradients (Fig. 14B). They observed strong ion selectivity, with permeabilities differing by up to two orders of magnitude for Cl^-, Br^-, I^-, and SCN^- ($SCN^- > I^- > Br^- > Cl^-$). Notably, SCN^- diffused ~300 times faster than Cl^-. Lowering the solution pH from 7.5 to 3.0 (thereby removing the negative charge at the CNT entrance) led to a three- to four-fold increase in anion permeability but did not alter the overall selectivity trend, suggesting that electrostatic repulsion plays a relatively minor role. Moreover, the measured permeability correlates strongly with the ion hydration energy[84,554] and follows an Arrhenius-like dependence, indicating that dehydration energy is the dominant contribution to the energy barrier for anion entry into the CNT porins. Additional AIMD simulations by Neklyudov *et al.*[554] further revealed that the transport of anions in single-file CNTs cannot be fully compensated by the polarizable CNT walls; instead, dehydration energy overwhelmingly governs selectivity, in contrast to cation transport in single-file CNTs.[69,176]

For CNTs that are comparable to or only marginally larger than the hydrated ion, the situation is even more subtle. Although ions may not necessarily need to shed parts of their hydration shells in these intermediate regimes, the layered structure of water inside the CNT, confinement-induced modifications to the solvation shell configuration, vdW and polarization interactions from the CNT walls as well as the dielectric energy barrier associated with the decreased dielectric constant inside CNTs (Fig. 14A) all can still drive significant selectivity.[44,83,108,113,114,141,447,468,514,749–751] Ions with favorable interaction potentials or with optimally rearranged hydration shells can therefore permeate more readily. For example, Wu *et al.*[141] measured the ion conductance in ~0.9 nm-diameter CNT membranes and noted slightly higher conductance for salts whose cations have lower hydration energies (Fig. 14C). Amiri *et al.*[108] observed similar cation selectivity in individual 1.5 nm-diameter CNTs. In larger 4.6 nm-diameter CNTs, Cui *et al.*[114] likewise observed the same correlation between cation hydration energy and ion conductance at concentrations above 0.02 M. Interestingly, at lower ion concentrations (<0.02 M), this trend was reversed, which they attributed to wall charge effects. Choi *et al.*[113] similarly found that in ~1.5 nm-diameter CNTs, ions with lower hydration energies generally transport faster, with the notable exception of Li^+ ions, which has the smallest ionic diameter among these ions.

7 Conclusion and outlook

While significant progress has been made in CNT nanofluidics, many challenges remain. Precise measurement, visualization, and control of nanofluidic transport in CNTs are still limited by the complexities of creating and probing nanoscale confinement. Additionally, our acquisition of fundamental insights has far outpaced their translation into specific applications. This section explores some of these challenges and outlines potential pathways to advance CNT nanofluidics.

7.1 Remaining knowledge gaps in CNT nanofluidics

The study of transport phenomena in CNTs has advanced significantly over the past two decades, yet precise measurements still remain challenging. One of the remaining knowledge gaps is how to control the structural heterogeneity of CNTs. Key parameters such as diameter, chirality, length, and defect density vary widely across samples, contributing to inconsistencies in reported water and ion transport rates (Fig. 10 and 11). The recently confirmed sensitivity of transport to the electronic properties of CNTs[113,122,123,170,176,485] (Fig. 12) further complicates the picture.

One of the knowledge gaps lies in the potential for switching transport mechanisms as the CNT pores become longer. For example, the predominant ion transport mechanism in ultrashort CNTs is based on the formation of ion–water clusters,[69] and thus should become much less efficient or energetically-favorable as the CNT length increases. As the CNT length increases to very large and nearly macroscopic values, there is a possibility of ion transport being subsumed by proton transport along the water molecules aligned in the nanotube.[121] These examples illustrate the need for further research on the scaling of ion transport over a large range of CNT lengths.

Yet another virtually unexplored knowledge gap in CNT nanofluidics is the effect of individual defects on the CNT walls. Given the small cross-sections of CNT channels, any defect is expected to significantly impact the transport efficiency, especially in the single-file CNT channels. It is conceivable that defects may act as pinning sites that could slow down or even completely stop the movement of water and ions through the CNT channels. The example of AQPs shows how a strategic arrangement of just a few charges (*e.g.*, defects) along the channel walls can lead to complete cessation of proton conduction;[191] it is likely that defects on the CNT wall can be configured to provide similar functionality. It is also unclear whether larger diameter CNTs can tolerate a higher density of defects without suffering a drastic reduction in transport efficiency.

Finally, a major challenge in advancing CNT nanofluidics is the absence of standardized protocols for CNT synthesis, purification, and structural characterization. Variations in chirality and surface chemistry can significantly affect transport behavior, complicating cross-platform comparisons and contributing to the wide variability observed in reported water and ion transport rates (Fig. 10 and 11). Even subtle structural differences can result in substantial variations in transport properties. For example, water transport in metallic CNTs can be ~70% higher than that in semiconducting CNTs of the same diameter.[176] Earlier CNT membrane studies (Fig. 4) reported data that were inherently averaged over diverse CNT populations.[6,60,115,141,394,665] In contrast, single-CNT studies provided more precise structural control,[25,64,113,121–123,134] but remained technically challenging and sometimes yielded transport rates inconsistent with membrane-based measurements. For instance, in sub-nanometer CNTs, water transport often falls below detectable levels, requiring multi-CNT systems to achieve measurable signals.[64] Recent progress in chirality sorting has enabled isolation of species-pure CNTs[21,175,238,244,266,350,753] (Fig. 3), but these methods remain complex and are not yet widely adopted. Additionally, reliance on indirect measurements, such as estimating surface charge through conductance changes with salt concentration and then modulating the latter through pH to infer slip lengths,[114] compounds uncertainties and limits the precision of transport measurements. To move the field forward and accelerate the development of reliable CNT nanofluidic systems, adoption of reproducible fabrication workflows, standardized transport measurement protocols, and direct structural characterization techniques remain essential.

7.2 Nanoscale imaging of nanofluidic transport in CNT channels

Direct visualization of nanoscale transport processes remains a major technical obstacle to gaining more information about nanofluidic transport. Direct observation of transport phenomena in CNTs would provide invaluable insights into the fundamental mechanisms governing fluid transport and molecular interactions in confined spaces. For example, phenomena such as dielectric contrast and solvation shell deformation can lead to substantial deviations in local ion concentrations inside CNTs over the bulk concentration.[638] Imaging should also be an invaluable tool for characterizing local non-equilibrium conductance states that can arise in nanoscale channels under dynamic voltage gating. High-resolution techniques such as transmission electron microscopy (HR-TEM), cryo-electron microscopy (cryo-EM), tip-enhanced Raman spectroscopy (TERS), and nanoscale vibrational spectroscopy (NVS) have shown promise for resolving fluidic structures in individual CNTs.[107,369,370,754–756] Several other techniques also show promise for visualizing nanotube transport. Optical methods have been used for measuring flow rates in individual systems. Secchi *et al.*[25] utilized optical microscopy to observe the deflection of flow lines near CNT exits using polystyrene tracer particles to quantify CNT water flow and slip lengths in the CNT channels (Fig. 4). However, this method is generally limited to high flow rates, with the smallest measurable CNT diameter being 30 nm. Researchers have also used fluorescence-based techniques to track molecular transport in real time for other nanofluidic systems. For instance, researchers have imaged single-proton diffusion on defective boron nitride surfaces.[757] A similar approach was later used to image molecular diffusion within a nanofluidic slit with a height of 1–2 nm.[758]

7.3 Controlling nanofluidic transport in CNTs

In biological channels, gating relies on tunable energy landscapes that regulate water and ion transport.[410,759] The same principle applies to the active control of fluid transport in CNTs. Researchers have been exploring approaches for controlling water and ion flow in CNTs using MD simulations since as early as 2005. Among the proposed approaches were deforming CNTs under external forces[473,760–762] and inducing vibrations in CNTs.[763–765] Other proposed approaches involve introducing stationary charges[152,160,419,486,590,591,680,762,766] or electrodes[767–769] to the CNTs. Another category of approaches seeks to utilize external stimuli such as light,[597,600] pressure,[126,770] temperature gradients,[513,516,771,772] electric fields,[159,515,597,598,773–782] magnetic fields,[600,783,784] or their combinations to enable long-range modulation of nanofluidic transport. One possible mechanism for controlling water flow involves perturbing the water structure and hydrogen bonding network within CNTs.[515,597,598,600,770,773,774,776–780,785] Another mechanism is to manipulate the motion of the water

contact line, driven by internal volumetric forces arising from thermal gradients, ionic charges, or magnetic nanoparticles.[513,516,771,772,781–784] In addition, although the current work mainly focuses on fluid transport in the inner channel of single-walled CNTs, recent MD studies[786,787] have suggested that the fluid structure and transport can also be effectively tuned within the interstitial region between the inner and outer walls of double-walled or multiple-walled CNTs. However, experimental validation of these modulation methods still remains scarce.

Recent experimental progress highlights some promising approaches. For example, Wang *et al.*[139] developed a CNT-based membrane system with dynamic curvature control, enabling curvature-tunable, asymmetric, and reversible ion transport. Furthermore, the unique electronic properties of CNT walls offer another avenue for fluid control. Rabinowitz *et al.*[74] demonstrated the use of a source–drain potential difference and electronic currents along CNT walls to pump ions *via* Coulomb drag effects. Cetindag *et al.*[674] enhanced ion selectivity and altered hydrodynamic properties in 2.2 nm CNTs by coating CNTs with hexagonal boron nitride (h-BN). This approach increased K^+ ion selectivity over Cl^- by ninefold and reduced hydrodynamic slip lengths by over an order of magnitude, suggesting the inner CNT wall may be transparent to charge-regulation and hydrodynamic-slip effects arising from the external h-BN layers.

7.4 Practical applications in CNT nanofluidics

The unique efficiency of nanofluidic transport in CNTs highlights a number of potential applications. One promising avenue for CNT nanofluidics could be the use of CNTs as nanopore sensors,[39,40,788] where their nanoscopic dimensions provide a highly sensitive platform for analyzing individual molecules. Ionic current blockades induced by the transport of polystyrene particles through single CNTs were observed in early 2000s.[371,381] Subsequent simulations[172,426,789] and experiments[13,122,123,137,692,790,791] explored the possibility of CNTs in detecting small analytes and DNA nucleotides. Wang *et al.*[692] identified four types of single nucleotides using $\sim$2 nm diameter CNTs and Peng *et al.*[133] further demonstrated the ability to differentiate amino acids using $\sim$1.2 nm diameter CNTs. Despite this encouraging progress, understanding ionic current signals associated with molecular translocation through CNTs remains an unfulfilled knowledge gap. For instance, the ionic current spikes observed in micrometer-long CNTs[122,692,790] differ significantly from the conventional current blockades seen in ultrashort CNTs[13,123,133] or other solid-state nanopores.[39] CNTs have also shown promise in developing smart ionic devices, such as ionic diodes and transistors.[14,79,139,328,743,792] These devices leverage the dynamics of ion transport in CNTs to enable innovative signal processing and computing functions, positioning CNTs as building blocks for hybrid electronic-fluidic systems. Achieving precise functionalization and ensuring operational stability, as well as better understanding of ion dynamics in CNT pores would be crucial for the further development of these devices.

One of the primary reasons CNTs have garnered significant attention is their ultrahigh water transport efficiency, which is particularly relevant to water–energy nexus applications. CNT membranes are, *in principle*, expected to offer unparalleled transport rates coupled with molecular-level selectivity, making them highly attractive for high-throughput separation systems.[15,80,109,115,386,388,397,666,687,688,734,793–803] In the reverse osmosis regime, CNTs with inner diameters of 0.5–0.6 nm achieve separation performance comparable to that of commercial thin-film composite membranes.[80] If such narrow CNTs were integrated into membranes at a feasible pore density of 2.5×10^{11} tubes per cm^2, the resulting water permeability could be four to six times higher than that of current commercial membranes. Due to this promise, both MD simulations[396,471,516,685,734,796,798,799,803,804] and experimental studies[80,109,115,127,142,331,386,388,397,664,666,673,794,797,801] have extensively explored the application of CNT membranes in water purification and desalination. However, we note that successful commercial development of CNT membranes for desalination will require pushing their performance beyond that of TFC membranes (in particular, selectivity enhancements), coupled with fabrication processes that provide comparable manufacturing costs.

CNT membranes have also been proposed for osmotic power harvesting, leveraging their strong ion selectivity and diffusio-osmotic transport efficiency.[51,663] For instance, Cui *et al.*[114] experimentally demonstrated an osmotic power density of up to 22.5 kW m^{-2} using individual CNTs with diameters of 4.6 nm. However, this value corresponds to a single-tube measurement; researchers still need to evaluate the performance of CNT membranes under practical conditions, particularly in light of realistic CNT pore densities. In addition, quantum mechanical studies have suggested that due to the tunable electronic properties of CNT walls, fluid flow in CNT pores can be converted into electric energy *via* two distinct mechanisms: the ionic Coulomb drag effect[74,805,806] and the hydroelectronic drag effect.[15,73,807–809] In the ionic Coulomb drag effect, flowing ions interact with conduction electrons in the CNT walls *via* Coulomb forces, whereas in the hydroelectronic drag effect, water molecules induce electron motion through hydrodynamic friction and phonon-mediated coupling. Simulations predicted power densities of up to 8 kW m^{-2} for the ionic Coulomb drag effect,[805] and up to 10 kW m^{-2} for the hydroelectronic drag effect.[73] However, recent experimental results by Jiang *et al.*[806] showed a significantly lower power density of only $\sim$7 W m^{-2} for CNT membranes composed of tubes with diameters in the range of 100-–250 nm and densities of 10^{11}–10^{12} tubes per cm^2. These discrepancies may stem from the relatively large CNT diameters that reduce energy conversion efficiency.

Despite the encouraging performance estimates of CNT nanofluidics for water purification and energy harvesting, several critical challenges must be addressed before scalable, practical applications of CNT membranes can be realized. Commercialization efforts face hurdles ranging from fabrication scale-up to the development of cohesive and integrated

processes. The viability of CNT membranes for industrial applications should be assessed only after detailed technoeconomic analyses that account for permeability–selectivity tradeoffs.[683,802,810] One particularly difficult challenge is achieving effective rejection of uncharged species, organic molecules, and micropollutants.

Another major obstacle lies in developing cost-effective methods to scale up CNT assemblies for water transport at volumes relevant to industrial water treatment. While CNTs themselves are not inherently expensive, the synthesis of aligned CNT arrays typically requires high temperatures, low-pressure environments, and costly thin-film vacuum deposition techniques for catalyst preparation. Bulk CNT synthesis is relatively more cost-effective, but it demands efficient approaches for generating open-ended CNT channels and assembling them into functional membrane structures. Although these challenges are significant and must not be underestimated, it is important to reiterate the intrinsic advantages of CNT nanofluidics. CNTs support exceptionally fast water transport, exhibit inherent resistance to fouling, and offer precise control over pore size and selectivity. Therefore, the transformative potential of CNT nanofluidics in membrane separations and energy harvesting should not be overlooked.

Finally, as CNT nanofluidics progress toward real-world applications, it is critical to assess their potential environmental and health impacts.[811–813] By 2030, an estimated 20–40 tons of CNTs may be released annually into soil, potentially reaching concentrations up to 3 μg kg^{-1}.[814–816] Surface waters and sediments may reach concentrations of 5 μg L^{-1} and 970 mg kg^{-1}, respectively.[817,818] In addition to environmental accumulation, pulmonary exposure to long CNTs, particularly at high doses, has been shown to cause lung damage and trigger oxidative stress, inflammation, DNA damage, and mutations.[819–822] For example, CNTs exceeding 15–20 μm in length can induce ''frustrated'' phagocytosis, wherein immune cells are unable to fully engulf or degrade the nanotubes, resulting in potential toxicity.[823–825] Moreover, CNT stiffness significantly influences their interaction with biological systems; rigid CNTs can disrupt lysosomes and are associated with both acute and chronic inflammatory responses.[826] In contrast, short or tangled CNTs exhibit substantially reduced toxicity.[821,827] Soluble, short CNTs have demonstrated no toxicity in primates[828] and can be safe for biomedical nanofluidic applications (*e.g.*, CNT porins).[440,442–444] Chemical functionalization can further mitigate toxicity by shortening, debundling, or softening CNTs.[829,830] Researchers also reported CNT biodegradation by immune cells,[831–834] although rates vary with material properties. Overall, CNT toxicity is governed by a combination of length, diameter, rigidity, and functionalization. Establishing standardized experimental protocols and uniform characterization methods will be essential to ensure global consistency in CNT toxicity assessment. Future research should aim not only to improve the production efficiency and cost-effectiveness of CNTs but also to advance our understanding of, and ability to mitigate, their potential environmental and health risks.

7.5 Concluding remarks

CNT nanofluidics has made remarkable advances in the past 25 years. These efforts have established CNT channels as an unparalleled platform for exploring nanoscale transport phenomena. This review has traced the development of nanofluidics in CNTs, from its origins to its breakthroughs, elucidating fundamental mechanisms and envisioning future potentials. A central theme of this review has been the interplay between confinement effects, surface interactions, entrance effects, and their couplings, which collectively govern the exceptional transport properties of CNTs. Cutting-edge molecular simulations and advanced experimental protocols, often used in tandem, have uncovered the intricate mechanisms underlying water, ion, and proton transport at the nanoscale.

The future of CNT nanofluidics lies in interdisciplinary innovation. Advances in materials science will expand the functionality and precision of CNT platforms. Enhanced characterization tools will provide a window and deeper insights into dynamics of transport processes. Simulations, turbocharged by machine learning based approaches will accelerate the discovery of optimized CNT designs and reveal fundamental transport mechanisms. Beyond these fundamental insights, CNT nanofluidics could offer transformative applications across diverse fields ranging from precision separations to sensing to ionic computing. As CNT nanofluidics advances further, it is also poised to contribute technological solutions to critical societal challenges such as sustainable energy technologies, clean water access, and advanced health care technologies.

Author contributions

All authors contributed to the writing of the manuscript. All authors approved the final version of the manuscript.

Conflicts of interest

There are no conflicts to declare.

Data availability

This article is a review of published literature and does not contain original data.

Acknowledgements

This work was supported as part of the Center for Enhanced Nanofluidic Transport (CENT), an Energy Frontier Research Center funded by the U.S. Department of Energy, Office of Science, Basic Energy Sciences under Award DE-SC0019112. Work at Lawrence Livermore National Laboratory was performed under the auspices of the US DOE under contract DE-AC52-07NA27344.

References

1 L. Bocquet and E. Charlaix, *Chem. Soc. Rev.*, 2010, **39**, 1073–1095.
2 J. C. Eijkel and A. V. D. Berg, *Microfluid. Nanofluid.*, 2005, (1), 249–267.
3 R. B. Schoch, J. Han and P. Renaud, *Rev. Mod. Phys.*, 2008, **80**, 839–883.
4 G. Hummer, J. C. Rasaiah and J. P. Noworyta, *Nature*, 2001, **414**, 188–190.
5 B. J. Hinds, N. Chopra, T. Rantell, R. Andrews, V. Gavalas and L. G. Bachas, *Science*, 2004, **303**, 62–65.
6 J. K. Holt, H. G. Park, Y. Wang, M. Stadermann, A. B. Artyukhin, C. P. Grigoropoulos, A. Noy and O. Bakajin, *Science*, 2006, **312**, 1034–1037.
7 L. Fumagalli, A. Esfandiar, R. Fabregas, S. Hu, P. Ares, A. Janardanan, Q. Yang, B. Radha, T. Taniguchi, K. Watanabe, G. Gomila, K. S. Novoselov and A. K. Geim, *Science*, 2018, **360**, 1339–1342.
8 L. Li, G. Meller and H. Kosina, *J. Appl. Phys.*, 2009, **106**, 013714.
9 N. R. Aluru, F. Aydin, M. Z. Bazant, D. Blankschtein, A. H. Brozena, J. P. de Souza, M. Elimelech, S. Faucher, J. T. Fourkas, V. B. Koman, M. Kuehne, H. J. Kulik, H. K. Li, Y. Li, Z. Li, A. Majumdar, J. Martis, R. P. Misra, A. Noy, T. A. Pham, H. Qu, A. Rayabharam, M. A. Reed, C. L. Ritt, E. Schwegler, Z. Siwy, M. S. Strano, Y. Wang, Y. C. Yao, C. Zhan and Z. Zhang, *Chem. Rev.*, 2023, **123**, 2737–2831.
10 L. Bocquet, *Nat. Mater.*, 2020, **19**, 254–256.
11 T. Emmerich, N. Ronceray, K. V. Agrawal, S. Garaj, M. Kumar, A. Noy and A. Radenovic, *Nat. Rev. Methods Primers*, 2024, **4**, 69.
12 J. P. Fried, J. L. Swett, B. P. Nadappuram, J. A. Mol, J. B. Edel, A. P. Ivanov and J. R. Yates, *Chem. Soc. Rev.*, 2021, **50**, 4974–4992.
13 J. Geng, K. Kim, J. Zhang, A. Escalada, R. Tunuguntla, L. R. Comolli, F. I. Allen, A. V. Shnyrova, K. R. Cho, D. Munoz, Y. M. Wang, C. P. Grigoropoulos, C. M. Ajo-Franklin, V. A. Frolov and A. Noy, *Nature*, 2014, **514**, 612–615.
14 Y. Fan, Y. Q. Hou, M. Wang, J. Zheng and X. Hou, *Mater. Adv.*, 2022, **3**, 3070–3088.
15 H. G. Park and Y. Jung, *Chem. Soc. Rev.*, 2014, **43**, 565–576.
16 A. Bhardwaj, M. V. Surmani Martins, Y. You, R. Sajja, M. Rimmer, S. Goutham, R. Qi, S. Abbas Dar, B. Radha and A. Keerthi, *Nat. Protoc.*, 2024, **19**, 240–280.
17 S. Sahu and M. Zwolak, *Rev. Mod. Phys.*, 2019, **91**, 021004.
18 S. Wang, L. Yang, G. He, B. Shi, Y. Li, H. Wu, R. Zhang, S. Nunes and Z. Jiang, *Chem. Soc. Rev.*, 2020, **49**, 1071–1089.
19 Y. Yang, M. Wang, Q. He, P. Zhai, P. Zhang and Y. Gong, *Small*, 2024, e2310681.
20 M. F. De Volder, S. H. Tawfick, R. H. Baughman and A. J. Hart, *Science*, 2013, **339**, 535–539.
21 F. Yang, M. Wang, D. Zhang, J. Yang, M. Zheng and Y. Li, *Chem. Rev.*, 2020, **120**, 2693–2758.
22 Y. You, A. Ismail, G.-H. Nam, S. Goutham, A. Keerthi and B. Radha, *Annu. Rev. Mater. Res.*, 2022, **52**, 189–218.
23 A. Pendse, S. Cetindag, P. Rehak, S. Behura, H. Gao, N. H. L. Nguyen, T. Wang, V. Berry, P. Král, J. Shan and S. Kim, *Adv. Funct. Mater.*, 2021, **31**, 2009586.
24 A. Pendse, S. Cetindag, K. Wang, D. Li, R. J. Castellano, D.-C. Yang, T. Wang, J. W. Shan and S. Kim, *Mater. Today*, 2022, **60**, 79–90.
25 E. Secchi, S. Marbach, A. Nigues, D. Stein, A. Siria and L. Bocquet, *Nature*, 2016, **537**, 210–213.
26 A. Siria, P. Poncharal, A. L. Biance, R. Fulcrand, X. Blase, S. T. Purcell and L. Bocquet, *Nature*, 2013, **494**, 455–458.
27 J. Feng, M. Graf, K. Liu, D. Ovchinnikov, D. Dumcenco, M. Heiranian, V. Nandigana, N. R. Aluru, A. Kis and A. Radenovic, *Nature*, 2016, **536**, 197–200.
28 J. Feng, K. Liu, R. D. Bulushev, S. Khlybov, D. Dumcenco, A. Kis and A. Radenovic, *Nat. Nanotechnol.*, 2015, **10**, 1070–1076.
29 M. Graf, M. Lihter, M. Thakur, V. Georgiou, J. Topolancik, B. R. Ilic, K. Liu, J. Feng, Y. Astier and A. Radenovic, *Nat. Protoc.*, 2019, **14**, 1130–1168.
30 F. Traversi, C. Raillon, S. M. Benameur, K. Liu, S. Khlybov, M. Tosun, D. Krasnozhon, A. Kis and A. Radenovic, *Nat. Nanotechnol.*, 2013, **8**, 939–945.
31 J. Shen, A. Aljarb, Y. Cai, X. Liu, J. Min, Y. Wang, Q. Wang, C. Zhang, C. Chen, M. Hakami, J.-H. Fu, H. Zhang, G. Li, X. Wang, Z. Chen, J. Li, X. Dong, K. Shih, K.-W. Huang, V. Tung, G. Shi, I. Pinnau, L.-J. Li and Y. Han, *Science*, 2025, **387**, 776–782.
32 S. Hong, G. Zou, H. Kim, D. Huang, P. Wang and H. N. Alshareef, *ACS Nano*, 2020, **14**, 9042–9049.
33 J. Wang, Z. Zhang, J. Zhu, M. Tian, S. Zheng, F. Wang, X. Wang and L. Wang, *Nat. Commun.*, 2020, **11**, 3540.
34 Y. Wang, H. Zhang, Y. Kang, Y. Zhu, G. P. Simon and H. Wang, *ACS Nano*, 2019, **13**, 11793–11799.
35 N. Kavokine, R. R. Netz and L. Bocquet, *Annu. Rev. Fluid Mech.*, 2021, **53**, 377–410.
36 D. Munoz-Santiburcio and D. Marx, *Chem. Rev.*, 2021, **121**, 6293–6320.
37 H. Qiu, W. Zhou and W. Guo, *ACS Nano*, 2021, **15**, 18848–18864.
38 W. Tang, J. P. Fried, R. D. Tilley and J. J. Gooding, *Chem. Soc. Rev.*, 2022, **51**, 5757–5776.
39 Y. Wu and J. J. Gooding, *Chem. Soc. Rev.*, 2022, **51**, 3862–3885.
40 J. Xu, X. Jiang and N. Yang, *Chem. Commun.*, 2023, **59**, 4838–4851.
41 L. Xue, H. Yamazaki, R. Ren, M. Wanunu, A. P. Ivanov and J. B. Edel, *Nat. Rev. Mater.*, 2020, **5**, 931–951.
42 Y.-L. Ying, Z.-L. Hu, S. Zhang, Y. Qing, A. Fragasso, G. Maglia, A. Meller, H. Bayley, C. Dekker and Y.-T. Long, *Nat. Nanotechnol.*, 2022, **17**, 1136–1146.
43 R. M. DuChanois, C. J. Porter, C. Violet, R. Verduzco and M. Elimelech, *Adv. Mater.*, 2021, **33**, e2101312.
44 R. Epsztein, R. M. DuChanois, C. L. Ritt, A. Noy and M. Elimelech, *Nat. Nanotechnol.*, 2020, **15**, 426–436.

45 J. Shen, G. Liu, Y. Han and W. Jin, *Nat. Rev. Mater.*, 2021, **6**, 294–312.
46 H. Zhang, X. Li, J. Hou, L. Jiang and H. Wang, *Chem. Soc. Rev.*, 2022, **51**, 2224–2254.
47 X. Ma, M. Neek-Amal and C. Sun, *ACS Nano*, 2024, **18**, 12610–12638.
48 M. Macha, S. Marion, V. V. R. Nandigana and A. Radenovic, *Nat. Rev. Mater.*, 2019, **4**, 588–605.
49 X. Tong, S. Liu, J. Crittenden and Y. Chen, *ACS Nano*, 2021, **15**, 5838–5860.
50 K. Xiao, L. Jiang and M. Antonietti, *Joule*, 2019, **3**, 2364–2380.
51 Z. Zhang, L. Wen and L. Jiang, *Nat. Rev. Mater.*, 2021, **6**, 622–639.
52 T. Emmerich, Y. Teng, N. Ronceray, E. Lopriore, R. Chiesa, A. Chernev, V. Artemov, M. Di Ventra, A. Kis and A. Radenovic, *Nat. Electron.*, 2024, **7**, 271–278.
53 T. M. Li and K. Xiao, *Adv. Mater. Technol.*, 2022, **7**, 2200205.
54 T. Mei, W. Liu, G. Xu, Y. Chen, M. Wu, L. Wang and K. Xiao, *ACS Nano*, 2024, **18**, 4624–4650.
55 T. Mei, H. Zhang and K. Xiao, *ACS Nano*, 2022, **16**, 13323–13338.
56 P. Robin, T. Emmerich, A. Ismail, A. Niguès, Y. You, G.-H. Nam, A. Keerthi, A. Siria, A. K. Geim, B. Radha and L. Bocquet, *Science*, 2023, **379**, 161–167.
57 T. Xiong, C. Li, X. He, B. Xie, J. Zong, Y. Jiang, W. Ma, F. Wu, J. Fei, P. Yu and L. Mao, *Science*, 2023, **379**, 156–161.
58 J. Zhang, W. Liu, J. Dai and K. Xiao, *Adv. Sci.*, 2022, **9**, e2200534.
59 D. Wang, Y. Tian and L. Jiang, *Small*, 2021, **17**, e2100788.
60 M. Majumder, N. Chopra, R. Andrews and B. J. Hinds, *Nature*, 2005, **438**, 44.
61 A. Schlaich, E. W. Knapp and R. R. Netz, *Phys. Rev. Lett.*, 2016, **117**, 048001.
62 D. Munoz-Santiburcio and D. Marx, *Phys. Rev. Lett.*, 2017, **119**, 056002.
63 D. Wu, Z. Zhao, B. Lin, Y. Song, J. Qi, J. Jiang, Z. Yuan, B. Cheng, M. Zhao, Y. Tian, Z. Wang, M. Wu, K. Bian, K.-H. Liu, L.-M. Xu, X. C. Zeng, E.-G. Wang and Y. Jiang, *Science*, 2024, **384**, 1254–1259.
64 R. H. Tunuguntla, R. Y. Henley, Y. C. Yao, T. A. Pham, M. Wanunu and A. Noy, *Science*, 2017, **357**, 792–796.
65 K. Gopinadhan, S. Hu, A. Esfandiar, M. Lozada-Hidalgo, F. C. Wang, Q. Yang, A. V. Tyurnina, A. Keerthi, B. Radha and A. K. Geim, *Science*, 2019, **363**, 145–148.
66 Q. Yang, P. Z. Sun, L. Fumagalli, Y. V. Stebunov, S. J. Haigh, Z. W. Zhou, I. V. Grigorieva, F. C. Wang and A. K. Geim, *Nature*, 2020, **588**, 250–253.
67 A. Keerthi, A. K. Geim, A. Janardanan, A. P. Rooney, A. Esfandiar, S. Hu, S. A. Dar, I. V. Grigorieva, S. J. Haigh, F. C. Wang and B. Radha, *Nature*, 2018, **558**, 420–424.
68 A. W. C. Lau and J. B. Sokoloff, *Phys. Rev. Lett.*, 2024, **132**, 194001.
69 Z. Li, R. P. Misra, Y. Li, Y. C. Yao, S. Zhao, Y. Zhang, Y. Chen, D. Blankschtein and A. Noy, *Nat. Nanotechnol.*, 2023, **18**, 177–183.
70 T. Mouterde, A. Keerthi, A. R. Poggioli, S. A. Dar, A. Siria, A. K. Geim, L. Bocquet and B. Radha, *Nature*, 2019, **567**, 87–90.
71 N. Kavokine, M.-L. Bocquet and L. Bocquet, *Nature*, 2022, **602**, 84–90.
72 G. D. Mahan, *Many-Particle Physics*, Springer, 2000, pp. 295–374.
73 B. Coquinot, L. Bocquet and N. Kavokine, *Proc. Natl. Acad. Sci. U. S. A.*, 2024, **121**, e2411613121.
74 J. Rabinowitz, C. Cohen and K. L. Shepard, *Nano Lett.*, 2020, **20**, 1148–1153.
75 M. E. Suk and N. R. Aluru, *Nanoscale Microscale Thermophys. Eng.*, 2017, **21**, 247–262.
76 J. H. Walther, K. Ritos, E. R. Cruz-Chu, C. M. Megaridis and P. Koumoutsakos, *Nano Lett.*, 2013, **13**, 1910–1914.
77 L. Cao, Q. Wen, Y. Feng, D. Ji, H. Li, N. Li, L. Jiang and W. Guo, *Adv. Funct. Mater.*, 2018, **28**, 1804189.
78 Y. Dai, Y. Zhang, Q. Ma, M. Lin, X. Zhang and F. Xia, *Anal. Chem.*, 2022, **94**, 17343–17348.
79 R. Peng, Y. Pan, B. Liu, Z. Li, P. Pan, S. Zhang, Z. Qin, A. R. Wheeler, X. S. Tang and X. Liu, *Small*, 2021, **17**, e2100383.
80 Y. Li, Z. Li, F. Aydin, J. Quan, X. Chen, Y. C. Yao, C. Zhan, Y. Chen, T. A. Pham and A. Noy, *Sci. Adv.*, 2020, **6**, eaba9966.
81 Z. Li, Y. Li, Y.-C. Yao, F. Aydin, C. Zhan, Y. Chen, M. Elimelech, T. A. Pham and A. Noy, *ACS Nano*, 2020, **14**, 6269–6275.
82 L. A. Richards, A. I. Schafer, B. S. Richards and B. Corry, *Small*, 2012, **8**, 1701–1709.
83 C. Song and B. Corry, *J. Phys. Chem. B*, 2009, **113**, 7642–7649.
84 L. A. Richards, A. I. Schafer, B. S. Richards and B. Corry, *Phys. Chem. Chem. Phys.*, 2012, **14**, 11633–11638.
85 J. Hou, C. Zhao and H. Zhang, *Small Methods*, 2024, **8**, e2300278.
86 Y. J. Lim, K. Goh and R. Wang, *Chem. Soc. Rev.*, 2022, **51**, 4537–4582.
87 C. I. Lynch, S. Rao and M. S. P. Sansom, *Chem. Rev.*, 2020, **120**, 10298–10335.
88 P. Agre, L. S. King, M. Yasui, W. B. Guggino, O. P. Ottersen, Y. Fujiyoshi, A. Engel and S. Nielsen, *J. Physiol.*, 2002, **542**, 3–16.
89 U. Kosinska Eriksson, G. Fischer, R. Friemann, G. Enkavi, E. Tajkhorshid and R. Neutze, *Science*, 2013, **340**, 1346–1349.
90 T. Walz, T. Hirai, K. Murata, J. B. Heymann, K. Mitsuoka, Y. Fujiyoshi, B. L. Smith, P. Agre and A. Engel, *Nature*, 1997, **387**, 624–627.
91 M. Barboiu, *Angew. Chem., Int. Ed.*, 2012, **51**, 11674–11676.
92 Y.-x Shen, W. Si, M. Erbakan, K. Decker, R. De Zorzi, P. O. Saboe, Y. J. Kang, S. Majd, P. J. Butler, T. Walz, A. Aksimentiev, J.-l Hou and M. Kumar, *Proc. Natl. Acad. Sci. U. S. A.*, 2015, **112**, 9810–9815.
93 J. Li, M. Gershow, D. Stein, E. Brandin and J. A. Golovchenko, *Nat. Mater.*, 2003, **2**, 611–615.

94 J. Li, D. Stein, C. McMullan, D. Branton, M. J. Aziz and J. A. Golovchenko, *Nature*, 2001, **412**, 166–169.
95 A. J. Storm, J. H. Chen, X. S. Ling, H. W. Zandbergen and C. Dekker, *Nat. Mater.*, 2003, **2**, 537–540.
96 K. Celebi, J. Buchheim, R. M. Wyss, A. Droudian, P. Gasser, I. Shorubalko, J. I. Kye, C. Lee and H. G. Park, *Science*, 2014, **344**, 289–292.
97 S. Garaj, W. Hubbard, A. Reina, J. Kong, D. Branton and J. A. Golovchenko, *Nature*, 2010, **467**, 190–193.
98 T. Jain, B. C. Rasera, R. J. Guerrero, M. S. Boutilier, S. C. O'Hern, J. C. Idrobo and R. Karnik, *Nat. Nanotechnol.*, 2015, **10**, 1053–1057.
99 M. I. Walker, K. Ubych, V. Saraswat, E. A. Chalklen, P. Braeuninger-Weimer, S. Caneva, R. S. Weatherup, S. Hofmann and U. F. Keyser, *ACS Nano*, 2017, **11**, 1340–1346.
100 J. Wang, C. Cheng, X. Zheng, J. C. Idrobo, A.-Y. Lu, J.-H. Park, B. G. Shin, S. J. Jung, T. Zhang, H. Wang, G. Gao, B. Shin, X. Jin, L. Ju, Y. Han, L.-J. Li, R. Karnik and J. Kong, *Nature*, 2023, **623**, 956–963.
101 Y. Yang, X. Yang, L. Liang, Y. Gao, H. Cheng, X. Li, M. Zou, R. Ma, Q. Yuan and X. Duan, *Science*, 2019, **364**, 1057–1062.
102 T. Ma, J. Janot and S. Balme, *Small Methods*, 2020, **4**, 2000366.
103 M. R. Powell, L. Cleary, M. Davenport, K. J. Shea and Z. S. Siwy, *Nat. Nanotechnol.*, 2011, **6**, 798–802.
104 K. Xiao, G. Xie, Z. Zhang, X. Y. Kong, Q. Liu, P. Li, L. Wen and L. Jiang, *Adv. Mater.*, 2016, **28**, 3345–3350.
105 W. Li, N. A. Bell, S. Hernandez-Ainsa, V. V. Thacker, A. M. Thackray, R. Bujdoso and U. F. Keyser, *ACS Nano*, 2013, **7**, 4129–4134.
106 Z. Siwy and F. Fornasiero, *Science*, 2017, **357**, 753.
107 K. V. Agrawal, S. Shimizu, L. W. Drahushuk, D. Kilcoyne and M. S. Strano, *Nat. Nanotechnol.*, 2017, **12**, 267–273.
108 H. Amiri, K. L. Shepard, C. Nuckolls and R. Hernandez Sanchez, *Nano Lett.*, 2017, **17**, 1204–1211.
109 N. Bui, E. R. Meshot, S. Kim, J. Peña, P. W. Gibson, K. J. Wu and F. Fornasiero, *Adv. Mater.*, 2016, **28**, 5871–5877.
110 S. Cambre, B. Schoeters, S. Luyckx, E. Goovaerts and W. Wenseleers, *Phys. Rev. Lett.*, 2010, **104**, 207401.
111 Q. Chen, J. L. Herberg, G. Mogilevsky, H.-J. Wang, M. Stadermann, J. K. Holt and Y. Wu, *Nano Lett.*, 2008, **8**, 1902–1905.
112 W. Choi, C. Y. Lee, M. H. Ham, S. Shimizu and M. S. Strano, *J. Am. Chem. Soc.*, 2011, **133**, 203–205.
113 W. Choi, Z. W. Ulissi, S. F. Shimizu, D. O. Bellisario, M. D. Ellison and M. S. Strano, *Nat. Commun.*, 2013, **4**, 2397.
114 G. Cui, Z. Xu, H. Li, S. Zhang, L. Xu, A. Siria and M. Ma, *Nat. Commun.*, 2023, **14**, 2295.
115 F. Fornasiero, H. G. Park, J. K. Holt, M. Stadermann, C. P. Grigoropoulos, A. Noy and O. Bakajin, *Proc. Natl. Acad. Sci. U. S. A.*, 2008, **105**, 17250–17255.
116 S. Ghosh, A. Sood and N. Kumar, *Science*, 2003, **299**, 1042–1044.
117 J. K. Holt, A. Noy, T. Huser, D. Eaglesham and O. Bakajin, *Nano Lett.*, 2004, **4**, 2245–2250.
118 S. C. Huang, A. B. Artyukhin, N. Misra, J. A. Martinez, P. A. Stroeve, C. P. Grigoropoulos, J. W. Ju and A. Noy, *Nano Lett.*, 2010, **10**, 1812–1816.
119 K. Kim, J. Geng, R. Tunuguntla, L. R. Comolli, C. P. Grigoropoulos, C. M. Ajo-Franklin and A. Noy, *Nano Lett.*, 2014, **14**, 7051–7056.
120 Y. T. Kim, H. Min, M. S. Strano, J. H. Han and C. Y. Lee, *Nano Lett.*, 2020, **20**, 812–819.
121 C. Y. Lee, W. Choi, J. H. Han and M. S. Strano, *Science*, 2010, **329**, 1320–1324.
122 H. Liu, J. He, J. Tang, H. Liu, P. Pang, D. Cao, P. Krstic, S. Joseph, S. Lindsay and C. Nuckolls, *Science*, 2010, **327**, 64–67.
123 L. Liu, C. Yang, K. Zhao, J. Li and H. C. Wu, *Nat. Commun.*, 2013, **4**, 2989.
124 M. Lokesh, S. K. Youn and H. G. Park, *Nano Lett.*, 2018, **18**, 6679–6685.
125 M. Majumder, N. Chopra and B. J. Hinds, *ACS Nano*, 2011, **5**, 3867–3877.
126 A. Marcotte, T. Mouterde, A. Nigues, A. Siria and L. Bocquet, *Nat. Mater.*, 2020, **19**, 1057–1061.
127 R. L. McGinnis, K. Reimund, J. Ren, L. Xia, M. R. Chowdhury, X. Sun, M. Abril, J. D. Moon, M. M. Merrick, J. Park, K. A. Stevens, J. R. McCutcheon and B. D. Freeman, *Sci. Adv.*, 2018, **4**, e1700938.
128 H. Min, Y. Kim, S. M. Moon, J. Han, K. Yum and C. Y. Lee, *Adv. Funct. Mater.*, 2019, **29**, 1900421.
129 N. Naguib, H. Ye, Y. Gogotsi, A. G. Yazicioglu, C. M. Megaridis and M. Yoshimura, *Nano Lett.*, 2004, **4**, 2237–2243.
130 T. Ohba, *Angew. Chem., Int. Ed.*, 2014, **53**, 8032–8036.
131 E. Paineau, P.-A. Albouy, S. Rouzière, A. Orecchini, S. Rols and P. Launois, *Nano Lett.*, 2013, **13**, 1751–1756.
132 P. Pang, J. He, J. H. Park, P. S. Krstic and S. Lindsay, *ACS Nano*, 2011, **5**, 7277–7283.
133 W. Peng, S. Yan, K. Zhou, H.-C. Wu, L. Liu and Y. Zhao, *Nat. Commun.*, 2023, **14**, 2662.
134 X. Qin, Q. Yuan, Y. Zhao, S. Xie and Z. Liu, *Nano Lett.*, 2011, **11**, 2173–2177.
135 C. Rust, P. Shapturenka, M. Spari, Q. Jin, H. Li, A. Bacher, M. Guttmann, M. Zheng, T. Adel, A. R. H. Walker, J. A. Fagan and B. S. Flavel, *Small*, 2023, **19**, e2206774.
136 E. Secchi, A. Nigues, L. Jubin, A. Siria and L. Bocquet, *Phys. Rev. Lett.*, 2016, **116**, 154501.
137 W. Song, P. Pang, J. He and S. Lindsay, *ACS Nano*, 2013, **7**, 689–694.
138 Y. Tomo, A. Askounis, T. Ikuta, Y. Takata, K. Sefiane and K. Takahashi, *Nano Lett.*, 2018, **18**, 1869–1874.
139 M. Wang, H. Meng, D. Wang, Y. Yin, P. Stroeve, Y. Zhang, Z. Sheng, B. Chen, K. Zhan and X. Hou, *Adv. Mater.*, 2019, **31**, 1805130.
140 M. Whitby, L. Cagnon, M. Thanou and N. Quirke, *Nano Lett.*, 2008, **8**, 2632–2637.
141 J. Wu, K. Gerstandt, H. Zhang, J. Liu and B. J. Hinds, *Nat. Nanotechnol.*, 2012, **7**, 133–139.

142 D. Yang, D. Tian, C. Xue, F. Gao, Y. Liu, H. Li, Y. Bao, J. Liang, Z. Zhao and J. Qiu, *Nano Lett*, 2018, **18**, 6150–6156.
143 D. C. Yang, R. J. Castellano, R. P. Silvy, S. K. Lageshetty, R. F. Praino, F. Fornasiero and J. W. Shan, *Nano Lett.*, 2023, **23**, 4956–4964.
144 Y. Yang, P. Dementyev, N. Biere, D. Emmrich, P. Stohmann, R. Korzetz, X. Zhang, A. Beyer, S. Koch, D. Anselmetti and A. Golzhauser, *ACS Nano*, 2018, **12**, 4695–4701.
145 Y. C. Yao, A. Taqieddin, M. A. Alibakhshi, M. Wanunu, N. R. Aluru and A. Noy, *ACS Nano*, 2019, **13**, 12851–12859.
146 K. Yazda, S. Tahir, T. Michel, B. Loubet, M. Manghi, J. Bentin, F. Picaud, J. Palmeri, F. Henn and V. Jourdain, *Nanoscale*, 2017, **9**, 11976–11986.
147 A. Alexiadis and S. Kassinos, *Chem. Rev.*, 2008, **108**, 5014–5034.
148 A. Berezhkovskii and G. Hummer, *Phys. Rev. Lett.*, 2002, **89**, 064503.
149 Q. Chen, L. Meng, Q. Li, D. Wang, W. Guo, Z. Shuai and L. Jiang, *Small*, 2011, **7**, 2225–2231.
150 K. Falk, F. Sedlmeier, L. Joly, R. R. Netz and L. Bocquet, *Nano Lett.*, 2010, **10**, 4067–4073.
151 R. Garcia-Fandino and M. S. Sansom, *Proc. Natl. Acad. Sci. U. S. A.*, 2012, **109**, 6939–6944.
152 X. Gong, J. Li, H. Lu, R. Wan, J. Li, J. Hu and H. Fang, *Nat. Nanotechnol.*, 2007, **2**, 709–712.
153 X. Gong, J. Li, H. Zhang, R. Wan, H. Lu, S. Wang and H. Fang, *Phys. Rev. Lett.*, 2008, **101**, 257801.
154 X. Gong, J. Li, K. Xu, J. Wang and H. Yang, *J. Am. Chem. Soc.*, 2010, **132**, 1873–1877.
155 S. Joseph and N. R. Aluru, *Nano Lett.*, 2008, **8**, 452–458.
156 S. Joseph, R. J. Mashl, E. Jakobsson and N. R. Aluru, *Nano Lett.*, 2003, **3**, 1399–1403.
157 A. Kalra, S. Garde and G. Hummer, *Proc. Natl. Acad. Sci. U. S. A.*, 2003, **100**, 10175–10180.
158 H. Li, J. S. Francisco and X. C. Zeng, *Proc. Natl. Acad. Sci. U. S. A.*, 2015, **112**, 10851–10856.
159 Z. Li and Q. Han, *Carbon*, 2023, **212**, 118164.
160 Z. Li, Q. Han, Y. Qiu and D. Wang, *Carbon*, 2023, **202**, 83–92.
161 J. Liu, G. Shi, P. Guo, J. Yang and H. Fang, *Phys. Rev. Lett.*, 2015, **115**, 164502.
162 R. Liu, Z. Liu, Y. Zhao, P. Cui and H. Wu, *Nano Lett.*, 2024, **24**, 3484–3489.
163 M. Ma, F. Grey, L. Shen, M. Urbakh, S. Wu, J. Z. Liu, Y. Liu and Q. Zheng, *Nat. Nanotechnol.*, 2015, **10**, 692–695.
164 T. A. Pascal, W. A. Goddard and Y. Jung, *Proc. Natl. Acad. Sci. U. S. A.*, 2011, **108**, 11794–11798.
165 R. Qiao and N. R. Aluru, *Nano Lett.*, 2003, **3**, 1013–1017.
166 M. Sahimi and F. Ebrahimi, *Phys. Rev. Lett.*, 2019, **122**, 214506.
167 Q. Shao, J. Zhou, L. Lu, X. Lu, Y. Zhu and S. Jiang, *Nano Lett.*, 2009, **9**, 989–994.
168 J. A. Thomas and A. J. McGaughey, *Nano Lett.*, 2008, **8**, 2788–2793.
169 J. A. Thomas and A. J. McGaughey, *Phys. Rev. Lett.*, 2009, **102**, 184502.
170 S. Velioglu, H. E. Karahan, K. Goh, T. H. Bae, Y. Chen and J. W. Chew, *Small*, 2020, **16**, e1907575.
171 Z. Wan, Y. Gao, X. Chen, X. C. Zeng, J. S. Francisco and C. Zhu, *Proc. Natl. Acad. Sci. U. S. A.*, 2022, **119**, e2211348119.
172 I. C. Yeh and G. Hummer, *Proc. Natl. Acad. Sci. U. S. A.*, 2004, **101**, 12177–12182.
173 F. Zhu, E. Tajkhorshid and K. Schulten, *Phys. Rev. Lett.*, 2004, **93**, 224501.
174 J. A. Fagan, *Nanoscale Adv.*, 2019, **1**, 3307–3324.
175 X. Wei, S. Li, W. Wang, X. Zhang, W. Zhou, S. Xie and H. Liu, *Adv. Sci.*, 2022, **9**, e2200054.
176 Y. Li, Z. Li, R. P. Misra, C. Liang, A. J. Gillen, S. Zhao, J. Abdullah, T. Laurence, J. A. Fagan, N. Aluru, D. Blankschtein and A. Noy, *Nat. Mater.*, 2024, **23**, 1123–1130.
177 N. Karousis, N. Tagmatarchis and D. Tasis, *Chem. Rev.*, 2010, **110**, 5366–5397.
178 L. Liu, J. Xie, T. Li and H. C. Wu, *Nat. Protoc.*, 2015, **10**, 1670–1678.
179 R. H. Tunuguntla, A. Escalada, A. Frolov and V. A. Noy, *Nat. Protoc.*, 2016, **11**, 2029–2047.
180 R. H. Tunuguntla, F. I. Allen, K. Kim, A. Belliveau and A. Noy, *Nat. Nanotechnol.*, 2016, **11**, 639–644.
181 J. Gao, Y. Feng, W. Guo and L. Jiang, *Chem. Soc. Rev.*, 2017, **46**, 5400–5424.
182 Y. Xu, *Adv. Mater.*, 2018, **30**, 1702419.
183 X. Yu and W. Ren, *Adv. Funct. Mater.*, 2024, **34**, 2313968.
184 M. Aminpour, S. A. Galindo Torres, A. Scheuermann and L. Li, *Phys. Rev. Appl.*, 2021, **15**, 054051.
185 K. Wu, Z. Chen, J. Li, X. Li, J. Xu and X. Dong, *Proc. Natl. Acad. Sci. U. S. A.*, 2017, **114**, 3358–3363.
186 S. Faucher, N. Aluru, M. Z. Bazant, D. Blankschtein, A. H. Brozena, J. Cumings, J. Pedro de Souza, M. Elimelech, R. Epsztein, J. T. Fourkas, A. G. Rajan, H. J. Kulik, A. Levy, A. Majumdar, C. Martin, M. McEldrew, R. P. Misra, A. Noy, T. A. Pham, M. Reed, E. Schwegler, Z. Siwy, Y. Wang and M. Strano, *J. Phys. Chem. C*, 2019, **123**, 21309–21326.
187 V. Kapil, C. Schran, A. Zen, J. Chen, C. J. Pickard and A. Michaelides, *Nature*, 2022, **609**, 512–516.
188 J. C. Rasaiah, S. Garde and G. Hummer, *Annu. Rev. Phys. Chem.*, 2008, **59**, 713–740.
189 D. G. Levitt, *Phys. Rev. A*, 1973, **8**, 3050–3054.
190 Y. Xue, Y. Xia, S. Yang, Y. Alsaid, K. Y. Fong, Y. Wang and X. Zhang, *Science*, 2021, **372**, 501–503.
191 K. Murata, K. Mitsuoka, T. Hirai, T. Walz, P. Agre, J. B. Heymann, A. Engel and Y. Fujiyoshi, *Nature*, 2000, **407**, 599–605.
192 R. MacKinnon, *Biosci. Rep.*, 2004, **24**, 75–100.
193 J. Wu, A. H. Lewis and J. Grandl, *Trends Biochem. Sci.*, 2017, **42**, 57–71.
194 J. Israelachvili, *Acc. Chem. Res.*, 1987, **20**, 415–421.
195 F. Ding, Z. Hu, Q. Zhong, K. Manfred, R. R. Gattass, M. R. Brindza, J. T. Fourkas, R. A. Walker and J. D. Weeks, *J. Phys. Chem. C*, 2010, **114**, 17651–17659.

196 T. Becker and F. Mugele, *Phys. Rev. Lett.*, 2003, **91**, 166104.
197 A. Maali, T. Cohen-Bouhacina, G. Couturier and J.-P. Aimé, *Phys. Rev. Lett.*, 2006, **96**, 086105.
198 L. Bocquet and J.-L. Barrat, *Soft Matter*, 2007, **3**, 685–693.
199 D. M. Huang, C. Sendner, D. Horinek, R. R. Netz and L. Bocquet, *Phys. Rev. Lett.*, 2008, **101**, 226101.
200 P. Joseph, C. Cottin-Bizonne, J.-M. Benoit, C. Ybert, C. Journet, P. Tabeling and L. Bocquet, *Phys. Rev. Lett.*, 2006, **97**, 156104.
201 C. Lee, C.-H. Choi and C.-J. C. Kim, *Phys. Rev. Lett.*, 2008, **101**, 064501.
202 W. Sparreboom, A. van den Berg and J. C. Eijkel, *New J. Phys.*, 2010, **12**, 015004.
203 I. Vlassiouk and Z. S. Siwy, *Nano Lett.*, 2007, **7**, 552–556.
204 P. Robin, N. Kavokine and L. Bocquet, *Science*, 2021, **373**, 687–691.
205 T. Emmerich, K. S. Vasu, A. Nigues, A. Keerthi, B. Radha, A. Siria and L. Bocquet, *Nat. Mater.*, 2022, **21**, 696–702.
206 D. Stein, M. Kruithof and C. Dekker, *Phys. Rev. Lett.*, 2004, **93**, 035901.
207 R. Karnik, K. Castelino, R. Fan, P. Yang and A. Majumdar, *Nano Lett.*, 2005, **5**, 1638–1642.
208 C. Lee, L. Joly, A. Siria, A. L. Biance, R. Fulcrand and L. Bocquet, *Nano Lett.*, 2012, **12**, 4037–4044.
209 A. Parsegian, *Nature*, 1969, **221**, 844–846.
210 N. Kavokine, S. Marbach, A. Siria and L. Bocquet, *Nat. Nanotechnol.*, 2019, **14**, 573–578.
211 D. Marx, *ChemPhysChem*, 2006, **7**, 1848–1870.
212 J. Köfinger, G. Hummer and C. Dellago, *Proc. Natl. Acad. Sci. U. S. A.*, 2008, **105**, 13218–13222.
213 A. Noy, *J. Phys. Chem. C*, 2013, **117**, 7656–7660.
214 J. W. G. Wilder, L. C. Venema, A. G. Rinzler, R. E. Smalley and C. Dekker, *Nature*, 1998, **391**, 59–62.
215 S. Zhang, L. Kang, X. Wang, L. Tong, L. Yang, Z. Wang, K. Qi, S. Deng, Q. Li, X. Bai, F. Ding and J. Zhang, *Nature*, 2017, **543**, 234–238.
216 S. Iijima, *Nature*, 1991, **354**, 56–58.
217 S. Iijima and T. Ichihashi, *Nature*, 1993, **363**, 603–605.
218 D. S. Bethune, C. H. Kiang, M. De Vries, G. Gorman, R. Savoy, J. Vazquez and R. Beyers, *Nature*, 1993, **363**, 605–607.
219 C. Allard, L. Alvarez, J. L. Bantignies, N. Bendiab, S. Cambre, S. Campidelli, J. A. Fagan, E. Flahaut, B. Flavel, F. Fossard, E. Gaufres, S. Heeg, J. S. Lauret, A. Loiseau, J. B. Marceau, R. Martel, L. Marty, T. Pichler, C. Voisin, S. Reich, A. Setaro, L. Shi and W. Wenseleers, *Chem. Soc. Rev.*, 2024, **53**, 8457–8512.
220 J. L. Blackburn, A. J. Ferguson, C. Cho and J. C. Grunlan, *Adv. Mater.*, 2018, **30**, 1704386.
221 H. Dai, *Surf. Sci*, 2002, **500**, 218–241.
222 S. Guo, E. R. Meshot, T. Kuykendall, S. Cabrini and F. Fornasiero, *Adv. Mater.*, 2015, **27**, 5726–5737.
223 A. T. Krasley, E. Li, J. M. Galeana, C. Bulumulla, A. G. Beyene and G. S. Demirer, *Chem. Rev.*, 2024, **124**, 3085–3185.
224 V. Schroeder, S. Savagatrup, M. He, S. Lin and T. M. Swager, *Chem. Rev.*, 2019, **119**, 599–663.
225 L. Yu, C. Shearer and J. Shapter, *Chem. Rev.*, 2016, **116**, 13413–13453.
226 A. Eatemadi, H. Daraee, H. Karimkhanloo, M. Kouhi, N. Zarghami, A. Akbarzadeh, M. Abasi, Y. Hanifehpour and S. W. Joo, *Nanoscale Res. Lett.*, 2014, **9**, 1–13.
227 N. Saifuddin, A. Raziah and A. Junizah, *J. Chem.*, 2013, 676815.
228 J.-C. Charlier, *Acc. Chem. Res.*, 2002, **35**, 1063–1069.
229 Y. Fan, B. R. Goldsmith and P. G. Collins, *Nat. Mater.*, 2005, **4**, 906–911.
230 M. C. Hersam, *Nat. Nanotechnol.*, 2008, **3**, 387–394.
231 A. Peigney, C. Laurent, E. Flahaut, R. Bacsa and A. Rousset, *Carbon*, 2001, **39**, 507–514.
232 J.-P. Salvetat, G. A. D. Briggs, J.-M. Bonard, R. R. Bacsa, A. J. Kulik, T. Stöckli, N. A. Burnham and L. Forró, *Phys. Rev. Lett.*, 1999, **82**, 944.
233 M.-F. Yu, B. S. Files, S. Arepalli and R. S. Ruoff, *Phys. Rev. Lett.*, 2000, **84**, 5552.
234 M. Endo, K. Takeuchi, S. Igarashi, K. Kobori, M. Shiraishi and H. W. Kroto, *J. Phys. Chem. Solids*, 1993, **54**, 1841–1848.
235 J. Tersoff and R. Ruoff, *Phys. Rev. Lett.*, 1994, **73**, 676.
236 J. Mintmire and C. White, *Carbon*, 1995, **33**, 893–902.
237 B. I. Yakobson, C. Brabec and J. Bernholc, *Phys. Rev. Lett.*, 1996, **76**, 2511.
238 M. He, S. Zhang and J. Zhang, *Chem. Rev.*, 2020, **120**, 12592–12684.
239 D. Jariwala, V. K. Sangwan, L. J. Lauhon, T. J. Marks and M. C. Hersam, *Chem. Soc. Rev.*, 2013, **42**, 2824–2860.
240 J. Ko and Y. Joo, *Adv. Mater. Interfaces*, 2021, **8**, 2002106.
241 S. Ling, X. Wei, X. Luo, X. Li, S. Li, F. Xiong, W. Zhou, S. Xie and H. Liu, *Small*, 2024, **20**, 2400303.
242 K. E. Moore, D. D. Tune and B. S. Flavel, *Adv. Mater.*, 2015, **27**, 3105–3137.
243 S. Qiu, K. Wu, B. Gao, L. Li, H. Jin and Q. Li, *Adv. Mater.*, 2019, **31**, 1800750.
244 R. Zhang, Y. Zhang and F. Wei, *Chem. Soc. Rev.*, 2017, **46**, 3661–3715.
245 C. Gao, M. Guo, Y. Liu, D. Zhang, F. Gao, L. Sun, J. Li, X. Chen, M. Terrones and Y. Wang, *Carbon*, 2023, 118133.
246 G. Hong, S. Diao, A. L. Antaris and H. Dai, *Chem. Rev.*, 2015, **115**, 10816–10906.
247 R. Niayler, J. Ackermann, C. Ma and S. Kruss, *Anal. Chem.*, 2022, **94**, 9941–9951.
248 M. Dresselhaus, G. Dresselhaus and A. Jorio, *Annu. Rev. Mater. Res.*, 2004, **34**, 247–278.
249 M. Dresselhaus, G. Dresselhaus and R. Saito, *Carbon*, 1995, **33**, 883–891.
250 T. W. Odom, J.-L. Huang, P. Kim and C. M. Lieber, *Nature*, 1998, **391**, 62–64.
251 M. Dresselhaus, G. Dresselhaus, J.-C. Charlier and E. Hernandez, *Philos. Trans. R. Soc., A*, 2004, **362**, 2065–2098.
252 T. Ando, *NPG Asia Mater.*, 2009, **1**, 17–21.
253 C. Dekker, *Phys. Today*, 1999, **52**, 22–28.
254 B. Chandra, J. Bhattacharjee, M. Purewal, Y.-W. Son, Y. Wu, M. Huang, H. Yan, T. F. Heinz, P. Kim and J. B. Neaton, *Nano Lett.*, 2009, **9**, 1544–1548.

255 H. Dai, E. W. Wong and C. M. Lieber, *Science*, 1996, **272**, 523–526.
256 A. Javey, J. Guo, Q. Wang, M. Lundstrom and H. Dai, *Nature*, 2003, **424**, 654–657.
257 A. Jorio, R. Saito, J. Hafner, C. Lieber, D. Hunter, T. McClure, G. Dresselhaus and M. Dresselhaus, *Phys. Rev. Lett.*, 2001, **86**, 1118.
258 M. J. O'connell, S. M. Bachilo, C. B. Huffman, V. C. Moore, M. S. Strano, E. H. Haroz, K. L. Rialon, P. J. Boul, W. H. Noon and C. Kittrell, *Science*, 2002, **297**, 593–596.
259 S. J. Tans, A. R. Verschueren and C. Dekker, *Nature*, 1998, **393**, 49–52.
260 L. Venema, J. Janssen, M. Buitelaar, J. Wildöer, S. Lemay, L. Kouwenhoven and C. Dekker, *Phys. Rev. B*, 2000, **62**, 5238.
261 T. M. Alharbi, K. Vimalanathan, W. D. Lawrance and C. L. Raston, *Carbon*, 2018, **140**, 428–432.
262 J. L. Blackburn, T. M. Barnes, M. C. Beard, Y.-H. Kim, R. C. Tenent, T. J. McDonald, B. To, T. J. Coutts and M. J. Heben, *ACS Nano*, 2008, **2**, 1266–1274.
263 L. Liu, X. Wei, Z. Yao, X. Li, W. Wang, Y. Wang, W. Zhou, F. Xiong, H. Kataura and S. Xie, *J. Phys. Chem. C*, 2022, **126**, 3787–3795.
264 P. Avouris, M. Freitag and V. Perebeinos, *Nat. Photonics*, 2008, **2**, 341–350.
265 P. Avouris and R. Martel, *MRS Bull.*, 2010, **35**, 306–313.
266 A. S. Bati, L. Yu, M. Batmunkh and J. G. Shapter, *Adv. Funct. Mater.*, 2019, **29**, 1902273.
267 A. D. Franklin, *Science*, 2015, **349**, aab2750.
268 X. He, H. Htoon, S. Doorn, W. Pernice, F. Pyatkov, R. Krupke, A. Jeantet, Y. Chassagneux and C. Voisin, *Nat. Mater.*, 2018, **17**, 663–670.
269 I. Jeon, Y. Matsuo and S. Maruyama, in *Single-Walled Carbon Nanotubes in Solar Cells*, ed. Y. Li and S. Maruyama, Springer International Publishing, Cham, 2019, pp. 271–298.
270 R. Rao, C. L. Pint, A. E. Islam, R. S. Weatherup, S. Hofmann, E. R. Meshot, F. Wu, C. Zhou, N. Dee and P. B. Amama, *ACS Nano*, 2018, **12**, 11756–11784.
271 B. Coquinot and N. Kavokine, *Nat. Mater.*, 2024, **23**, 1021–1022.
272 M. S. Dresselhaus, G. Dresselhaus, R. Saito and A. Jorio, *Phys. Rep.*, 2005, **409**, 47–99.
273 M. Ouyang, J.-L. Huang, C. L. Cheung and C. M. Lieber, *Science*, 2001, **292**, 702–705.
274 M. Anantram and F. Leonard, *Rep. Prog. Phys.*, 2006, **69**, 507.
275 T. Hasegawa, D. J. Arenas and H. Kohno, *Fullerenes, Nanotubes Carbon Nanostruct.*, 2015, **23**, 687–690.
276 M. Baibarac, A. Matea, M. Ilie, I. Baltog and A. Magrez, *Anal. Methods*, 2015, **7**, 6225–6230.
277 J. Chrzanowska, J. Hoffman, A. Ma olepszy, M. Mazurkiewicz, T. A. Kowalewski, Z. Szymanski and L. Stobinski, *Phys. Status Solidi B*, 2015, **252**, 1860–1867.
278 L. Kang, S. Zhang, Q. Li and J. Zhang, *J. Am. Chem. Soc.*, 2016, **138**, 6727–6730.
279 Y. M. Manawi, Ihsanullah, A. Samara, T. Al-Ansari and M. A. Atieh, *Materials*, 2018, **11**, 822.
280 N. Mohammadian, S. M. Ghoreishi, S. Hafeziyeh, S. Saeidi and D. D. Dionysiou, *Nanomaterials*, 2018, **8**, 316.
281 A. Pattanshetti, N. Pradeep, V. Chaitra and V. Uma, *SN Appl. Sci.*, 2020, **2**, 1–7.
282 A. H. Sari, A. Khazali and S. S. Parhizgar, *Int. Nano Lett.*, 2018, **8**, 19–23.
283 R. M. Wyss, J. E. Klare, H. G. Park, A. Noy, O. Bakajin and V. Lulevich, *ACS Appl. Mater. Interfaces*, 2014, **6**, 21019–21025.
284 A. Thess, R. Lee, P. Nikolaev, H. Dai, P. Petit, J. Robert, C. Xu, Y. H. Lee, S. G. Kim and A. G. Rinzler, *Science*, 1996, **273**, 483–487.
285 H. Cheng, F. Li, X. Sun, S. Brown, M. Pimenta, A. Marucci, G. Dresselhaus and M. Dresselhaus, *Chem. Phys. Lett.*, 1998, **289**, 602–610.
286 M. Joséâ-Yacamán, M. Miki-Yoshida, L. Rendón and J. G. Santiesteban, *Appl. Phys. Lett.*, 1993, **62**, 202–204.
287 W. Li, S. Xie, L. X. Qian, B. Chang, B. Zou, W. Zhou, R. Zhao and G. Wang, *Science*, 1996, **274**, 1701–1703.
288 J.-F. Colomer, C. Stephan, S. Lefrant, G. Van Tendeloo, I. Willems, Z. Konya, A. Fonseca, C. Laurent and J. B. Nagy, *Chem. Phys. Lett.*, 2000, **317**, 83–89.
289 H. Dai, *Nanotube Growth and Characterization*, Springer, 2001, pp. 29–53.
290 J. H. Hafner, M. J. Bronikowski, B. R. Azamian, P. Nikolaev, A. G. Rinzler, D. T. Colbert, K. A. Smith and R. E. Smalley, *Chem. Phys. Lett.*, 1998, **296**, 195–202.
291 C. Journet, W. K. Maser, P. Bernier, A. Loiseau, M. L. de La Chapelle, D. S. Lefrant, P. Deniard, R. Lee and J. E. Fischer, *Nature*, 1997, **388**, 756–758.
292 J. Kong, H. T. Soh, A. M. Cassell, C. F. Quate and H. Dai, *Nature*, 1998, **395**, 878–881.
293 P. Nikolaev, M. J. Bronikowski, R. K. Bradley, F. Rohmund, D. T. Colbert, K. Smith and R. E. Smalley, *Chem. Phys. Lett.*, 1999, **313**, 91–97.
294 B. Satishkumar, A. Govindaraj, R. Sen and C. Rao, *Chem. Phys. Lett.*, 1998, **293**, 47–52.
295 M. Su, B. Zheng and J. Liu, *Chem. Phys. Lett.*, 2000, **322**, 321–326.
296 Z. Zhang, Y. Chen, P. Shen, J. Chen, S. Wang, B. Wang, S. Ma, B. Lyu, X. Zhou, S. Lou, Z. Wu, Y. Xie, C. Zhang, L. Wang, K. Xu, H. Li, G. Wang, K. Watanabe, T. Taniguchi, D. Qian, J. Jia, Q. Liang, X. Wang, W. Yang, G. Zhang, C. Jin, W. Ouyang and Z. Shi, *Science*, 2025, **387**, 1310–1316.
297 S. M. Bachilo, L. Balzano, J. E. Herrera, F. Pompeo, D. E. Resasco and R. B. Weisman, *J. Am. Chem. Soc.*, 2003, **125**, 11186–11187.
298 Y. Che, C. Wang, J. Liu, B. Liu, X. Lin, J. Parker, C. Beasley, H.-S. P. Wong and C. Zhou, *ACS Nano*, 2012, **6**, 7454–7462.
299 L. Ding, A. Tselev, J. Wang, D. Yuan, H. Chu, T. P. McNicholas, Y. Li and J. Liu, *Nano Lett.*, 2009, **9**, 800–805.
300 G. Hong, B. Zhang, B. Peng, J. Zhang, W. M. Choi, J.-Y. Choi, J. M. Kim and Z. Liu, *J. Am. Chem. Soc.*, 2009, **131**, 14642–14643.

301 I. Ibrahim, J. Kalbacova, V. Engemaier, J. Pang, R. D. Rodriguez, D. Grimm, T. Gemming, D. R. Zahn, O. G. Schmidt and J. Eckert, *Chem. Mater.*, 2015, **27**, 5964–5973.
302 Y. Li, D. Mann, M. Rolandi, W. Kim, A. Ural, S. Hung, A. Javey, J. Cao, D. Wang and E. Yenilmez, *Nano Lett.*, 2004, **4**, 317–321.
303 X. Qin, F. Peng, F. Yang, X. He, H. Huang, D. Luo, J. Yang, S. Wang, H. Liu and L. Peng, *Nano Lett.*, 2014, **14**, 512–517.
304 S. Shiina, T. Murohashi, K. Ishibashi, X. He, T. Koretsune, Z. Liu, W. Terashima, Y. K. Kato, K. Inoue, M. Saito, Y. Ikuhara and T. Kato, *ACS Nano*, 2024, **18**, 23979–23990.
305 J. Wang, X. Jin, Z. Liu, G. Yu, Q. Ji, H. Wei, J. Zhang, K. Zhang, D. Li and Z. Yuan, *Nat. Catal.*, 2018, **1**, 326–331.
306 B. Yu, C. Liu, P.-X. Hou, Y. Tian, S. Li, B. Liu, F. Li, E. I. Kauppinen and H.-M. Cheng, *J. Am. Chem. Soc.*, 2011, **133**, 5232–5235.
307 W. Zhou, S. Zhan, L. Ding and J. Liu, *J. Am. Chem. Soc.*, 2012, **134**, 14019–14026.
308 H. Dai, A. G. Rinzler, P. Nikolaev, A. Thess, D. T. Colbert and R. E. Smalley, *Chem. Phys. Lett.*, 1996, **260**, 471–475.
309 A. Grüneis, M. Rümmeli, C. Kramberger, A. Barreiro, T. Pichler, R. Pfeiffer, H. Kuzmany, T. Gemming and B. Büchner, *Carbon*, 2006, **44**, 3177–3182.
310 J. Wei, L. Ci, B. Jiang, Y. Li, X. Zhang, H. Zhu, C. Xu and D. Wu, *J. Mater. Chem.*, 2003, **13**, 1340–1344.
311 R. Krupke, F. Hennrich, H. V. Loihneysen and M. M. Kappes, *Science*, 2003, **301**, 344–347.
312 M. S. Strano, C. A. Dyke, M. L. Usrey, P. W. Barone, M. J. Allen, H. Shan, C. Kittrell, R. H. Hauge, J. M. Tour and R. E. Smalley, *Science*, 2003, **301**, 1519–1522.
313 M. S. Arnold, A. A. Green, J. F. Hulvat, S. I. Stupp and M. C. Hersam, *Nat. Nanotechnol.*, 2006, **1**, 60–65.
314 S. Ghosh, S. M. Bachilo and R. B. Weisman, *Nat. Nanotechnol.*, 2010, **5**, 443–450.
315 X. Tu, S. Manohar, A. Jagota and M. Zheng, *Nature*, 2009, **460**, 250–253.
316 T. Tanaka, H. Jin, Y. Miyata, S. Fujii, H. Suga, Y. Naitoh, T. Minari, T. Miyadera, K. Tsukagoshi and H. Kataura, *Nano Lett.*, 2009, **9**, 1497–1500.
317 C. Y. Khripin, J. A. Fagan and M. Zheng, *J. Am. Chem. Soc.*, 2013, **135**, 6822–6825.
318 W. Yang, P. Thordarson, J. J. Gooding, S. P. Ringer and F. Braet, *Nanotechnology*, 2007, **18**, 412001.
319 Z. Jin, X. Sun, G. Xu, S. H. Goh and W. Ji, *Chem. Phys. Lett.*, 2000, **318**, 505–510.
320 K. M. El-Say, *J. Appl. Pharm. Sci.*, 2011, **1**, 29–39.
321 H. Hu, B. Zhao, M. A. Hamon, K. Kamaras, M. E. Itkis and R. C. Haddon, *J. Am. Chem. Soc.*, 2003, **125**, 14893–14900.
322 S. Rathinavel, K. Priyadharshini and D. Panda, *Mater. Sci. Eng., B*, 2021, **268**, 115095.
323 L. Bao, O. Martin, T. Wei, M. E. Pérez-Ojeda, F. Hauke and A. Hirsch, *Carbon*, 2021, **171**, 768–776.
324 D. Tasis, N. Tagmatarchis, A. Bianco and M. Prato, *Chem. Rev.*, 2006, **106**, 1105–1136.
325 M. Majumder, N. Chopra and B. J. Hinds, *J. Am. Chem. Soc.*, 2005, **127**, 9062–9070.
326 M. Majumder, X. Zhan, R. Andrews and B. J. Hinds, *Langmuir*, 2007, **23**, 8624–8631.
327 J. Wu, K. Gerstandt, M. Majumder, X. Zhan and B. J. Hinds, *Nanoscale*, 2011, **3**, 3321–3328.
328 J. Wu, X. Zhan and B. J. Hinds, *Chem. Commun.*, 2012, **48**, 7979–7981.
329 P. Nednoor, N. Chopra, V. Gavalas, L. Bachas and B. Hinds, *Chem. Mater.*, 2005, **17**, 3595–3599.
330 P. Nednoor, V. G. Gavalas, N. Chopra, B. J. Hinds and L. G. Bachas, *J. Mater. Chem.*, 2007, **17**, 1755–1757.
331 S.-M. Park, J. Jung, S. Lee, Y. Baek, J. Yoon, D. K. Seo and Y. H. Kim, *Desalination*, 2014, **343**, 180–186.
332 W. Zhang, Z. Zhang and Y. Zhang, *Nanoscale Res. Lett.*, 2011, **6**, 555.
333 J. N. Coleman, *Adv. Funct. Mater.*, 2009, **19**, 3680–3695.
334 A. J. Gillen and A. A. Boghossian, *Front. Chem.*, 2019, **7**, 612.
335 S. Kruss, M. P. Landry, E. Vander Ende, B. M. Lima, N. F. Reuel, J. Zhang, J. Nelson, B. Mu, A. Hilmer and M. Strano, *J. Am. Chem. Soc.*, 2014, **136**, 713–724.
336 G. R. Dieckmann, A. B. Dalton, P. A. Johnson, J. Razal, J. Chen, G. M. Giordano, E. Muñoz, I. H. Musselman, R. H. Baughman and R. K. Draper, *J. Am. Chem. Soc.*, 2003, **125**, 1770–1777.
337 M. Dinarvand, E. Neubert, D. Meyer, G. Selvaggio, F. A. Mann, L. Erpenbeck and S. Kruss, *Nano Lett.*, 2019, **19**, 6604–6611.
338 S. Wang, E. S. Humphreys, S.-Y. Chung, D. F. Delduco, S. R. Lustig, H. Wang, K. N. Parker, N. W. Rizzo, S. Subramoney and Y.-M. Chiang, *Nat. Mater.*, 2003, **2**, 196–200.
339 V. Zorbas, A. Ortiz-Acevedo, A. B. Dalton, M. M. Yoshida, G. R. Dieckmann, R. K. Draper, R. H. Baughman, M. Jose-Yacaman and I. H. Musselman, *J. Am. Chem. Soc.*, 2004, **126**, 7222–7227.
340 A. Antonucci, J. Kupis-Rozmyslowicz and A. A. Boghossian, *ACS Appl. Mater. Interfaces*, 2017, **9**, 11321–11331.
341 T. Fujigaya and N. Nakashima, *Sci. Technol. Adv. Mater.*, 2015, **16**, 024802.
342 S. S. Karajanagi, H. Yang, P. Asuri, E. Sellitto, J. S. Dordick and R. S. Kane, *Langmuir*, 2006, **22**, 1392–1395.
343 E. Polo and S. Kruss, *J. Phys. Chem. C*, 2016, **120**, 3061–3070.
344 D. Zhang, J. Yang and Y. Li, *Small*, 2013, **9**, 1284–1304.
345 A. Hashimoto, K. Suenaga, A. Gloter, K. Urita and S. Iijima, *Nature*, 2004, **430**, 870–873.
346 L. Qin, *J. Mater. Res.*, 1994, **9**, 2450–2456.
347 L.-C. Qin, *Rep. Prog. Phys.*, 2006, **69**, 2761.
348 K. Liu, X. Hong, Q. Zhou, C. Jin, J. Li, W. Zhou, J. Liu, E. Wang, A. Zettl and F. Wang, *Nat. Nanotechnol.*, 2013, **8**, 917–922.
349 W. Wu, J. Yue, X. Lin, D. Li, F. Zhu, X. Yin, J. Zhu, J. Wang, J. Zhang and Y. Chen, *Nano Res.*, 2015, **8**, 2721–2732.

350 F. Yang, X. Wang, D. Zhang, J. Yang, D. Luo, Z. Xu, J. Wei, J.-Q. Wang, Z. Xu and F. Peng, *Nature*, 2014, **510**, 522–524.
351 F. Zhang, P.-X. Hou, C. Liu, B.-W. Wang, H. Jiang, M.-L. Chen, D.-M. Sun, J.-C. Li, H.-T. Cong and E. I. Kauppinen, *Nat. Commun.*, 2016, **7**, 11160.
352 D. Mattia and Y. Gogotsi, *Microfluid. Nanofluid.*, 2008, **5**, 289–305.
353 Y. Gogotsi, J. A. Libera, A. Güvenç-Yazicioglu and C. M. Megaridis, *Appl. Phys. Lett.*, 2001, **79**, 1021–1023.
354 Y. Maniwa, H. Kataura, M. Abe, S. Suzuki, Y. Achiba, H. Kira and K. Matsuda, *J. Phys. Soc. Jpn.*, 2002, **71**, 2863–2866.
355 Y. Maniwa, H. Kataura, M. Abe, A. Udaka, S. Suzuki, Y. Achiba, H. Kira, K. Matsuda, H. Kadowaki and Y. Okabe, *Chem. Phys. Lett.*, 2005, **401**, 534–538.
356 I. C. Tran, R. H. Tunuguntla, K. Kim, J. R. Lee, T. M. Willey, T. M. Weiss, A. Noy and T. van Buuren, *Nano Lett.*, 2016, **16**, 4019–4024.
357 N. R. de Souza, A. I. Kolesnikov, C. J. Burnham and C. K. Loong, *J. Phys.:Condens. Matter*, 2006, **18**, S2321.
358 A. I. Kolesnikov, J.-M. Zanotti, C.-K. Loong, P. Thiyagarajan, A. P. Moravsky, R. O. Loutfy and C. J. Burnham, *Phys. Rev. Lett.*, 2004, **93**, 035503.
359 S. Ghosh, K. V. Ramanathan and A. K. Sood, *Europhys. Lett.*, 2004, **65**, 678.
360 K. Matsuda, T. Hibi, H. Kadowaki, H. Kataura and Y. Maniwa, *Phys. Rev. B*, 2006, **74**, 073415.
361 W. Sekhaneh, M. Kotecha, U. Dettlaff-Weglikowska and W. S. Veeman, *Chem. Phys. Lett.*, 2006, **428**, 143–147.
362 H.-J. Wang, X.-K. Xi, A. Kleinhammes and Y. Wu, *Science*, 2008, **322**, 80–83.
363 O. Byl, J.-C. Liu, Y. Wang, W.-L. Yim, J. K. Johnson and J. T. Yates, *J. Am. Chem. Soc.*, 2006, **128**, 12090–12097.
364 X. Ma, S. Cambré, W. Wenseleers, S. K. Doorn and H. Htoon, *Phys. Rev. Lett.*, 2017, **118**, 027402.
365 S. C. Sharma, D. Singh and Y. Li, *J. Raman Spectrosc.*, 2005, **36**, 755–761.
366 M. J. Longhurst and N. Quirke, *J. Chem. Phys*, 2006, **125**, 184705.
367 J. K. Holt, *Microfluid. Nanofluid.*, 2008, **5**, 425–442.
368 W. Wenseleers, S. Cambré, J. Culin, A. Bouwen and E. Goovaerts, *Adv. Mater.*, 2007, **19**, 2274–2278.
369 S. Faucher, M. Kuehne, V. B. Koman, N. Northrup, D. Kozawa, Z. Yuan, S. X. Li, Y. Zeng, T. Ichihara, R. P. Misra, N. Aluru, D. Blankschtein and M. S. Strano, *ACS Nano*, 2021, **15**, 2778–2790.
370 Y.-M. Tu, M. Kuehne, R. P. Misra, C. L. Ritt, H. Oliaei, S. Faucher, H. Li, X. Xu, A. Penn, S. Yang, J. F. Yang, K. Sendgikoski, J. Chakraverty, J. Cumings, A. Majumdar, N. R. Aluru, J. A. Hachtel, D. Blankschtein and M. S. Strano, *Nat. Commun.*, 2024, **15**, 5605.
371 L. Sun and R. M. Crooks, *J. Am. Chem. Soc.*, 2000, **122**, 12340–12345.
372 S. Kim, J. R. Jinschek, H. Chen, D. S. Sholl and E. Marand, *Nano Lett.*, 2007, **7**, 2806–2811.
373 P. M. Ajayan, T. W. Ebbesen, T. Ichihashi, S. Iijima, K. Tanigaki and H. Hiura, *Nature*, 1993, **362**, 522–525.
374 P. M. Ajayan and S. lijima, *Nature*, 1993, **361**, 333–334.
375 E. Dujardin, T. Ebbesen, H. Hiura and K. Tanigaki, *Science*, 1994, **265**, 1850–1852.
376 M. R. Pederson and J. Q. Broughton, *Phys. Rev. Lett.*, 1992, **69**, 2689–2692.
377 S. C. Tsang, Y. K. Chen, P. J. F. Harris and M. L. H. Green, *Nature*, 1994, **372**, 159–162.
378 S. C. Tsang, P. J. F. Harris and M. L. H. Green, *Nature*, 1993, **362**, 520–522.
379 D. Ugarte, A. Chatelain and W. De Heer, *Science*, 1996, **274**, 1897–1899.
380 E. Mamontov, C. J. Burnham, S. H. Chen, A. P. Moravsky, C. K. Loong, N. R. de Souza and A. I. Kolesnikov, *J. Chem. Phys*, 2006, **124**, 194703.
381 T. Ito, L. Sun and R. M. Crooks, *Anal. Chem.*, 2003, **75**, 2399–2406.
382 R. R. Henriquez, T. Ito, L. Sun and R. M. Crooks, *Analyst*, 2004, **129**, 478–482.
383 C. Dellago, M. M. Naor and G. Hummer, *Phys. Rev. Lett.*, 2003, **90**, 105902.
384 F. Zhu and K. Schulten, *Biophys. J.*, 2003, **85**, 236–244.
385 D. J. Mann and M. D. Halls, *Phys. Rev. Lett.*, 2003, **90**, 195503.
386 M. L. Jue, S. F. Buchsbaum, C. Chen, S. J. Park, E. R. Meshot, K. J. J. Wu and F. Fornasiero, *Adv. Sci.*, 2020, **7**, 2001670.
387 S. Kim, F. Fornasiero, H. G. Park, J. B. In, E. Meshot, G. Giraldo, M. Stadermann, M. Fireman, J. Shan, C. P. Grigoropoulos and O. Bakajin, *J. Membr. Sci.*, 2014, **460**, 91–98.
388 Y. Li, C. Chen, E. R. Meshot, S. F. Buchsbaum, M. Herbert, R. Zhu, O. Kulikov, B. McDonald, N. T. N. Bui, M. L. Jue, S. J. Park, C. A. Valdez, S. Hok, Q. He, C. J. Doona, K. J. Wu, T. M. Swager and F. Fornasiero, *Adv. Funct. Mater.*, 2020, **30**, 2000258.
389 E. R. Meshot, S. J. Park, S. F. Buchsbaum, M. L. Jue, T. R. Kuykendall, E. Schaible, L. B. Bayu Aji, S. O. Kucheyev, K. J. J. Wu and F. Fornasiero, *Carbon*, 2020, **159**, 236–246.
390 S. F. Buchsbaum, M. L. Jue, A. M. Sawvel, C. Chen, E. R. Meshot, S. J. Park, M. Wood, K. J. Wu, C. L. Bilodeau, F. Aydin, T. A. Pham, E. Y. Lau and F. Fornasiero, *Adv. Sci.*, 2021, **8**, 2001802.
391 M. S. Mauter, M. Elimelech and C. O. Osuji, *ACS Nano*, 2010, **4**, 6651–6658.
392 R. J. Castellano, C. Akin, G. Giraldo, S. Kim, F. Fornasiero and J. W. Shan, *J. Appl. Phys*, 2015, **117**, 214306.
393 R. J. Castellano, R. F. Praino, E. R. Meshot, C. Chen, F. Fornasiero and J. W. Shan, *Carbon*, 2020, **157**, 208–216.
394 F. Fornasiero, J. B. In, S. Kim, H. G. Park, Y. Wang, C. P. Grigoropoulos, A. Noy and O. Bakajin, *Langmuir*, 2010, **26**, 14848–14853.
395 P. Krishnakumar, P. Tiwari, S. Staples, T. Luo, Y. Darici, J. He and S. Lindsay, *Nanotechnology*, 2012, **23**, 455101.

396 W. F. Chan, H. Y. Chen, A. Surapathi, M. G. Taylor, X. Shao, E. Marand and J. K. Johnson, *ACS Nano*, 2013, **7**, 5308–5319.
397 X. Song, S. Li, W. Zhang, H. Liu, J. Jiang and C. Zhang, *J. Membr. Sci.*, 2022, 121029.
398 J. Wu, K. S. Paudel, C. Strasinger, D. Hammell, A. L. Stinchcomb and B. J. Hinds, *Proc. Natl. Acad. Sci. U. S. A.*, 2010, **107**, 11698–11702.
399 T. Ito, L. Sun, R. R. Henriquez and R. M. Crooks, *Acc. Chem. Res.*, 2004, **37**, 937–945.
400 D. Cao, P. Pang, J. He, T. Luo, J. H. Park, P. Krstic, C. Nuckolls, J. Tang and S. Lindsay, *ACS Nano*, 2011, **5**, 3113–3119.
401 R. Tao, X. Gao, D. Lin, Y. Chen, Y. Jin, X. Chen, S. Yao, P. Huang, J. Zhang and Z. Li, *Phys. Fluids*, 2021, **33**, 012015.
402 K. Yazda, S. Roman, S. Tahir, F. Henn and V. Jourdain, *MRS Adv.*, 2016, **1**, 2085–2090.
403 S. K. Burley, R. Bhatt, C. Bhikadiya, C. Bi, A. Biester, P. Biswas, S. Bittrich, S. Blaumann, R. Brown, H. Chao, V. R. Chithari, P. A. Craig, G. V. Crichlow, J. M. Duarte, S. Dutta, Z. Feng, J. W. Flatt, S. Ghosh, D. S. Goodsell, R. K. Green, V. Guranovic, J. Henry, B. P. Hudson, M. Joy, J. T. Kaelber, I. Khokhriakov, J.-S. Lai, C. L. Lawson, Y. Liang, D. Myers-Turnbull, E. Peisach, I. Persikova, D. W. Piehl, A. Pingale, Y. Rose, J. Sagendorf, A. Sali, J. Segura, M. Sekharan, C. Shao, J. Smith, M. Trumbull, B. Vallat, M. Voigt, B. Webb, S. Whetstone, A. Wu-Wu, T. Xing, J. Y. Young, A. Zalevsky and C. Zardecki, *Nucleic Acids Res.*, 2024, **53**, D564–D574.
404 W. Humphrey, A. Dalke and K. Schulten, *J. Mol. Graphics*, 1996, **14**, 33–38.
405 W. Xin, L. Jiang and L. Wen, *Angew. Chem., Int. Ed.*, 2022, **61**, e202207369.
406 S. P. Zheng, L. B. Huang, Z. Sun and M. Barboiu, *Angew. Chem., Int. Ed.*, 2021, **60**, 566–597.
407 B. L. de Groot and H. Grubmüller, *Science*, 2001, **294**, 2353–2357.
408 D. A. Kopfer, C. Song, T. Gruene, G. M. Sheldrick, U. Zachariae and B. L. de Groot, *Science*, 2014, **346**, 352–355.
409 D. A. Doyle, J. Morais Cabral, R. A. Pfuetzner, A. Kuo, J. M. Gulbis, S. L. Cohen, B. T. Chait and R. MacKinnon, *Science*, 1998, **280**, 69–77.
410 E. Flood, C. Boiteux, B. Lev, I. Vorobyov and T. W. Allen, *Chem. Rev.*, 2019, **119**, 7737–7832.
411 W. Kopec, D. A. Köpfer, O. N. Vickery, A. S. Bondarenko, T. L. C. Jansen, B. L. de Groot and U. Zachariae, *Nat. Chem.*, 2018, **10**, 813–820.
412 M. Akeson and D. W. Deamer, *Biophys. J.*, 1991, **60**, 101–109.
413 S. Braun-Sand, A. Burykin, Z. T. Chu and A. Warshel, *J. Phys. Chem. B*, 2005, **109**, 583–592.
414 R. Pomes and B. Roux, *Biophys. J.*, 1996, **71**, 19–39.
415 R. Pomes and B. Roux, *Biophys. J.*, 2002, **82**, 2304–2316.
416 G. Portella, P. Pohl and B. L. de Groot, *Biophys. J.*, 2007, **92**, 3930–3937.
417 D. E. Sagnella and G. A. Voth, *Biophys. J.*, 1996, **70**, 2043–2051.
418 M. Dutt, M. J. Nayhouse, O. Kuksenok, S. R. Little and A. C. Balazs, *Curr. Nanosci.*, 2011, **7**, 699–715.
419 B. Liu, X. Li, B. Li, B. Xu and Y. Zhao, *Nano Lett.*, 2009, **9**, 1386–1394.
420 C. F. Lopez, S. O. Nielsen, P. B. Moore and M. L. Klein, *Proc. Natl. Acad. Sci. U. S. A.*, 2004, **101**, 4431–4434.
421 C. Shen, G. Zou, W. Guo and H. Gao, *Carbon*, 2020, **164**, 391–397.
422 M. Vogele, J. Kofinger and G. Hummer, *Faraday Discuss.*, 2018, **209**, 341–358.
423 R. Garcia-Fandiño, n Piñeiro, J. L. Trick and M. S. P. Sansom, *ACS Nano*, 2016, **10**, 3693–3701.
424 J. A. Garate, N. J. English and J. M. D. MacElroy, *Mol. Simul.*, 2009, **35**, 3–12.
425 S. Zeng, J. Chen, X. Wang, G. Zhou, L. Chen and C. Dai, *J. Phys. Chem. C*, 2018, **122**, 27681–27688.
426 U. Zimmerli and P. Koumoutsakos, *Biophys. J.*, 2008, **94**, 2546–2557.
427 A. Yadav, P. Kelich, N. Kallmyer, N. F. Reuel and L. Vukovic, *ACS Appl. Mater. Interfaces*, 2023, **15**, 24084–24096.
428 N. W. S. Kam, M. O'Connell, J. A. Wisdom and H. Dai, *Proc. Natl. Acad. Sci. U. S. A.*, 2005, **102**, 11600–11605.
429 L. Lacerda, H. Ali-Boucetta, S. Kraszewski, M. Tarek, M. Prato, C. Ramseyer, K. Kostarelos and A. Bianco, *Nanoscale*, 2013, **5**, 10242–10250.
430 X. Sun, S. Zaric, D. Daranciang, K. Welsher, Y. Lu, X. Li and H. Dai, *J. Am. Chem. Soc.*, 2008, **130**, 6551–6555.
431 R. H. Tunuguntla, X. Chen, A. Belliveau, F. I. Allen and A. Noy, *J. Phys. Chem. C*, 2017, **121**, 3117–3125.
432 Y. Zhang, R. H. Tunuguntla, P. O. Choi and A. Noy, *Philos. Trans. R Soc. Lond. B Biol. Sci.*, 2017, **372**, 20160226.
433 J. R. Sanborn, X. Chen, Y. C. Yao, J. A. Hammons, R. H. Tunuguntla, Y. Zhang, C. C. Newcomb, J. A. Soltis, J. J. De Yoreo, A. Van Buuren, A. N. Parikh and A. Noy, *Adv. Mater.*, 2018, **30**, e1803355.
434 S. Zhang, J. J. Hettige, Y. Li, T. Jian, W. Yang, Y. Yao, R. Zheng, Z. Lin, J. Tao and J. J. De Yoreo, *Small*, 2023, **19**, 2206810.
435 S. Zhao, A. J. Gillen, Y. Li and A. Noy, *J. Phys. Chem. Lett.*, 2023, **14**, 9372–9376.
436 R. H. Tunuguntla, A. Y. Hu, Y. Zhang and A. Noy, *Faraday Discuss.*, 2018, **209**, 359–369.
437 J. M. Hicks, Y.-C. Yao, S. Barber, N. Neate, J. A. Watts, A. Noy and F. J. Rawson, *Small*, 2021, **17**, 2102517.
438 X. Chen, H. Zhang, R. H. Tunuguntla and A. Noy, *Nano Lett.*, 2019, **19**, 629–634.
439 Z. Hemmatian, R. H. Tunuguntla, A. Noy and M. Rolandi, *PLoS One*, 2019, **14**, e0212197.
440 X. Shen, Q. Lu, T. Peng, Y. Zhang, W. Tan, Y. Yang, J. Tan and Q. Yuan, *J. Am. Chem. Soc.*, 2024, **146**, 19896–19908.
441 Q. Wang, J. Sun, W. Xue, G. Zhao, W. Ding, K. Zhang, S. Wang and Y. Li, *Desalination*, 2023, **546**, 116216.
442 N. T. Ho, M. Siggel, K. V. Camacho, R. M. Bhaskara, J. M. Hicks, Y.-C. Yao, Y. Zhang, J. Köfinger, G. Hummer

and A. Noy, *Proc. Natl. Acad. Sci. U. S. A.*, 2021, **118**, e2016974118.
443 R. M. Bhaskara, S. M. Linker, M. Vogele, J. Kofinger and G. Hummer, *ACS Nano*, 2017, **11**, 1273–1280.
444 J. Wu, X. Zeng, L. Wang, J. Zhang, S. Cui, Z. Ma, R. Pan, C. Liu, D. Kong, J. Song, L. Liu, C. Feng, W. Shen, X. Suo, Z. Lin, H. K. Lee and S. Tang, *Adv. Mater.*, 2025, **37**, 2418271.
445 Z. Li, A. T. Hall, Y. Wang, Y. Li, D. O. Byrne, L. R. Scammell, R. R. Whitney, F. I. Allen, J. Cumings and A. Noy, *Sci. Adv.*, 2024, **10**, eado8081.
446 T. Gutsmann, T. Heimburg, U. Keyser, K. R. Mahendran and M. Winterhalter, *Nat. Protoc.*, 2015, **10**, 188–198.
447 T. A. Pham, S. M. G. Mortuza, B. C. Wood, E. Y. Lau, T. Ogitsu, S. F. Buchsbaum, Z. S. Siwy, F. Fornasiero and E. Schwegler, *J. Phys. Chem. C*, 2016, **120**, 7332–7338.
448 K. Koga, G. T. Gao, H. Tanaka and X. C. Zeng, *Nature*, 2001, **412**, 802–805.
449 C. Xie and H. Li, *Wiley Interdiscip. Rev.:Comput. Mol. Sci.*, 2023, **13**, e1661.
450 M. K. Borg, D. A. Lockerby, K. Ritos and J. M. Reese, *J. Membr. Sci.*, 2018, **567**, 115–126.
451 R. M. Kumar, M. Elango, R. Parthasarathi and V. Subramanian, *J. Phys. Chem. A*, 2011, **115**, 12841–12851.
452 T. Kurita, S. Okada and A. Oshiyama, *Phys. Rev. B*, 2007, **75**, 205424.
453 D. Lu, Y. Li, U. Ravaioli and K. Schulten, *J. Phys. Chem. B*, 2005, **109**, 11461–11467.
454 L. Wang, J. Zhao, F. Li, H. Fang and J. P. Lu, *J. Phys. Chem. C*, 2009, **113**, 5368–5375.
455 Y. J. Wang and L. Y. Wang, *Int. J. Quantum Chem.*, 2011, **111**, 4465–4471.
456 M. K. Tripathy, N. K. Jena, A. K. Samanta, S. K. Ghosh and K. R. S. Chandrakumar, *Theor. Chem. Acc.*, 2014, **133**, 1576.
457 K. Laasonen, M. Sprik, M. Parrinello and R. Car, *J. Chem. Phys*, 1993, **99**, 9080–9089.
458 A. Omranpour, P. Montero De Hijes, J. Behler and C. Dellago, *J. Chem. Phys*, 2024, **160**, 170901.
459 J. Chen, G. Schusteritsch, C. J. Pickard, C. G. Salzmann and A. Michaelides, *Phys. Rev. Lett.*, 2016, **116**, 025501.
460 P. L. Geissler, C. Dellago, D. Chandler, J. Hutter and M. Parrinello, *Science*, 2001, **291**, 2121–2124.
461 M. J. Gillan, D. Alfe and A. Michaelides, *J. Chem. Phys*, 2016, **144**, 130901.
462 J. Hermann, J. DiStasio, A. Robert and A. Tkatchenko, *Chem. Rev.*, 2017, **117**, 4714–4758.
463 M. E. Tuckerman, K. Laasonen, M. Sprik and M. Parrinello, *J. Phys.:Condens. Matter*, 1994, **6**, A93.
464 F. Zipoli, R. Car, M. H. Cohen and A. Selloni, *J. Am. Chem. Soc.*, 2010, **132**, 8593–8601.
465 J. K. Clark II and S. J. Paddison, *Phys. Chem. Chem. Phys.*, 2014, **16**, 17756–17769.
466 D. Liu, J. Li, J. Wu and D. Lu, *ACS Omega*, 2022, **7**, 40466–40479.
467 F. L. Thiemann, C. Schran, P. Rowe, E. A. Muller and A. Michaelides, *ACS Nano*, 2022, **16**, 10775–10782.
468 F. Aydin, A. Moradzadeh, C. L. Bilodeau, E. Y. Lau, E. Schwegler, N. R. Aluru and T. A. Pham, *J. Chem. Theory Comput.*, 2021, **17**, 1596–1605.
469 A. Bankura and A. Chandra, *J. Phys. Chem. B*, 2012, **116**, 9744–9757.
470 J. Chen, X. Z. Li, Q. Zhang, A. Michaelides and E. Wang, *Phys. Chem. Chem. Phys.*, 2013, **15**, 6344–6349.
471 B. Corry, *J. Phys. Chem. B*, 2008, **112**, 1427–1434.
472 S. K. Kannam, B. D. Todd, J. S. Hansen and P. J. Daivis, *J. Chem. Phys*, 2013, **138**, 094701.
473 R. Wan, J. Li, H. Lu and H. Fang, *J. Am. Chem. Soc.*, 2005, **127**, 7166–7170.
474 T. Werder, J. H. Walther, R. L. Jaffe, T. Halicioglu, F. Noca and P. Koumoutsakos, *Nano Lett.*, 2001, **1**, 697–702.
475 J. Zou, B. Ji, X.-Q. Feng and H. Gao, *Nano Lett.*, 2006, **6**, 430–434.
476 J. Cobeña-Reyes and M. Sahimi, *J. Phys. Chem. C*, 2020, **125**, 946–956.
477 J.-w Feng, H.-m Ding, C.-l Ren and Y.-q Ma, *Nanoscale*, 2014, **6**, 13606–13612.
478 S. H. Ganjiani and A. Hossein Nezhad, *Phys. Chem. Chem. Phys.*, 2018, **20**, 5140–5148.
479 V. Vijayaraghavan and C. H. Wong, *Nano-Micro Lett.*, 2014, **6**, 268–279.
480 H. A. Zambrano, J. H. Walther, P. Koumoutsakos and I. F. Sbalzarini, *Nano Lett.*, 2009, **9**, 66–71.
481 M. Manghi, J. Palmeri, F. Henn, A. Noury, F. Picaud, G. Herlem and V. Jourdain, *J. Phys. Chem. C*, 2021, **125**, 22943–22950.
482 X. Zhang, W. Zhou, F. Xu, M. Wei and Y. Wang, *Nanoscale*, 2018, **10**, 13242–13249.
483 M. Heiranian and N. R. Aluru, *ACS Nano*, 2020, **14**, 272–281.
484 X. Wei and T. Luo, *J. Phys. Chem. C*, 2018, **122**, 5131–5140.
485 C. Y. Won, S. Joseph and N. R. Aluru, *J. Chem. Phys*, 2006, **125**, 114701.
486 G. Zuo, R. Shen, S. Ma and W. Guo, *ACS Nano*, 2010, **4**, 205–210.
487 R. L. Jaffe, P. Gonnet, T. Werder, J. H. Walther and P. Koumoutsakos, *Mol. Simul.*, 2004, **30**, 205–216.
488 T. Werder, J. H. Walther, R. Jaffe, T. Halicioglu and P. Koumoutsakos, *J. Phys. Chem. B*, 2003, **107**, 1345–1352.
489 J. S. Rowlinson, *Trans. Faraday Soc.*, 1951, **47**, 120–129.
490 F. H. Stillinger and A. Rahman, *J. Chem. Phys*, 1974, **60**, 1545–1557.
491 J. L. Abascal, E. Sanz, R. Garcia Fernandez and C. Vega, *J. Chem. Phys*, 2005, **122**, 234511.
492 G. A. Cisneros, K. T. Wikfeldt, L. Ojamäe, J. Lu, Y. Xu, H. Torabifard, A. P. Bartók, G. Csányi, V. Molinero and F. Paesani, *Chem. Rev.*, 2016, **116**, 7501–7528.
493 I. Gartner, E. Thomas, K. M. Hunter, E. Lambros, A. Caruso, M. Riera, G. R. Medders, A. Z. Panagiotopoulos, P. G. Debenedetti and F. Paesani, *J. Phys. Chem. Lett.*, 2022, **13**, 3652–3658.
494 B. Guillot, *J. Mol. Liq.*, 2002, **101**, 219–260.

495 A. V. Onufriev and S. Izadi, *Wiley Interdiscip. Rev.:Comput. Mol. Sci*, 2018, **8**, e1347.
496 C. Vega, J. L. F. Abascal, M. M. Conde and J. L. Aragones, *Faraday Discuss.*, 2009, **141**, 251–276.
497 C. Vega and J. L. F. Abascal, *Phys. Chem. Chem. Phys.*, 2011, **13**, 19663–19688.
498 J. L. Abascal and C. Vega, *J. Chem. Phys*, 2005, **123**, 234505.
499 H. Berendsen, J. Grigera and T. Straatsma, *J. Phys. Chem.*, 1987, **91**, 6269–6271.
500 W. L. Jorgensen, J. Chandrasekhar, J. D. Madura, R. W. Impey and M. L. Klein, *J. Chem. Phys*, 1983, **79**, 926–935.
501 M. W. Mahoney and W. L. Jorgensen, *J. Chem. Phys*, 2000, **112**, 8910–8922.
502 H. W. Horn, W. C. Swope, J. W. Pitera, J. D. Madura, T. J. Dick, G. L. Hura and T. Head-Gordon, *J. Chem. Phys*, 2004, **120**, 9665–9678.
503 S. K. Kannam, B. D. Todd, J. S. Hansen and P. J. Daivis, *J. Chem. Phys*, 2012, **136**, 024705.
504 J. Losey, S. K. Kannam, B. D. Todd and R. J. Sadus, *J. Chem. Phys.*, 2019, **150**, 194501.
505 B. H. S. Mendonça, E. E. de Moraes, R. J. C. Batista, A. B. de Oliveira, M. C. Barbosa and H. Chacham, *J. Phys. Chem. C*, 2023, **127**, 9769–9778.
506 L. Liu and G. N. Patey, *J. Chem. Phys.*, 2014, **141**, 18C518.
507 A. Mejri, K. Mazouzi, G. Herlem, F. Picaud, T. Hennequin, J. Palmeri and M. Manghi, *J. Mol. Liq.*, 2022, **351**, 118575.
508 H. Qiu and W. Guo, *Phys. Rev. Lett.*, 2013, **110**, 195701.
509 H. Qiu, X. C. Zeng and W. Guo, *ACS Nano*, 2015, **9**, 9877–9884.
510 Y. Zhu, F. Wang, J. Bai, X. C. Zeng and H. Wu, *ACS Nano*, 2015, **9**, 12197–12204.
511 H. Gao, J. Wang, Y. Liu, Y. Xie, P. Král and R. Lu, *J. Chem. Phys*, 2021, **154**, 104707.
512 X. Gao, T. Zhao and Z. Li, *Phys. Fluids*, 2017, **29**, 092003.
513 E. Oyarzua, J. H. Walther, C. M. Megaridis, P. Koumoutsakos and H. A. Zambrano, *ACS Nano*, 2017, **11**, 9997–10002.
514 J. J. Sardroodi, J. Azamat, A. Rastkar and N. R. Yousefnia, *Chem. Phys.*, 2012, **403**, 105–112.
515 J. Su and H. Guo, *ACS Nano*, 2011, **5**, 351–359.
516 K. Zhao and H. Wu, *Nano Lett.*, 2015, **15**, 3664–3668.
517 K. Zhao and H. Wu, *Phys. Chem. Chem. Phys.*, 2017, **19**, 28496–28501.
518 M. D. Ma, L. Shen, J. Sheridan, J. Z. Liu, C. Chen and Q. Zheng, *Phys. Rev. E*, 2011, **83**, 036316.
519 W. Cao, L. Huang, M. Ma, L. Lu and X. Lu, *J. Phys. Chem. C*, 2018, **122**, 19124–19132.
520 X. Gao, T. Zhao and Z. Li, *J. Appl. Phys*, 2014, **116**, 054311.
521 L. Jin, D. Zhang, Y. Zhu, X. Yang, Y. Gao and Z. Wang, *J. Phys. Chem. Lett.*, 2020, 350–354.
522 M. H. Köhler and J. R. Bordin, *J. Phys. Chem. C*, 2018, **122**, 6684–6690.
523 M. Shaat, *Langmuir*, 2017, **33**, 12814–12819.
524 L. Bocquet and J.-L. Barrat, *Phys. Rev. E*, 1994, **49**, 3079.
525 S. Chen, H. Wang, T. Qian and P. Sheng, *Phys. Rev. E*, 2015, **92**, 043007.
526 M. Groombridge, M. Schneemilch and N. Quirke, *Mol. Simul.*, 2011, **37**, 1023–1030.
527 J. S. Hansen, B. Todd and P. J. Daivis, *Phys. Rev. E:Stat., Nonlinear, Soft Matter Phys.*, 2011, **84**, 016313.
528 K. Huang and I. Szlufarska, *Phys. Rev. E*, 2014, **89**, 032119.
529 S. K. Kannam, B. D. Todd, J. S. Hansen and P. J. Daivis, *J. Chem. Phys.*, 2011, **135**, 144701.
530 H. Oga, Y. Yamaguchi, T. Omori, S. Merabia and L. Joly, *J. Chem. Phys.*, 2019, **151**, 054502.
531 J. Petravic and P. Harrowell, *J. Chem. Phys*, 2007, **127**, 174706.
532 V. P. Sokhan and N. Quirke, *Phys. Rev. E*, 2008, **78**, 015301.
533 V. P. Sokhan, D. Nicholson and N. Quirke, *J. Chem. Phys*, 2002, **117**, 8531–8539.
534 V. Sokhan, D. Nicholson and N. Quirke, *J. Chem. Phys*, 2001, **115**, 3878–3887.
535 V. Sokhan and N. Quirke, *Mol. Simul.*, 2004, **30**, 217–224.
536 A. T. Bui and S. J. Cox, *J. Chem. Phys*, 2024, **161**, 201102.
537 B. J. Bucior, G. V. Kolmakov, J. M. Male, J. Liu, D. L. Chen, P. Kumar and J. K. Johnson, *Langmuir*, 2017, **33**, 11834–11844.
538 A. Striolo, *Nano Lett.*, 2006, **6**, 633–639.
539 S. Vaitheeswaran, J. C. Rasaiah and G. Hummer, *J. Chem. Phys*, 2004, **121**, 7955–7965.
540 L. Joly, *J. Chem. Phys*, 2011, **135**, 214705.
541 T. B. Sisan and S. Lichter, *Microfluid. Nanofluid.*, 2011, **11**, 787–791.
542 T. J. Day, A. V. Soudackov, M. Cuma, U. W. Schmitt and G. A. Voth, *J. Chem. Phys*, 2002, **117**, 5839–5849.
543 T. Lazaridis and G. Hummer, *J. Chem. Inf. Model.*, 2017, **57**, 2833–2845.
544 Z. Qin, H. L. Tepper and G. A. Voth, *J. Phys. Chem. B*, 2007, **111**, 9931–9939.
545 U. W. Schmitt and G. A. Voth, *J. Chem. Phys*, 1999, **111**, 9361–9381.
546 G. A. Voth, *Acc. Chem. Res.*, 2006, **39**, 143–150.
547 M. L. Brewer, U. W. Schmitt and G. A. Voth, *Biophys. J.*, 2001, **80**, 1691–1702.
548 Z. Cao, Y. Peng, T. Yan, S. Li, A. Li and G. A. Voth, *J. Am. Chem. Soc.*, 2010, **132**, 11395–11397.
549 C. Dellago and G. Hummer, *Phys. Rev. Lett.*, 2006, **97**, 245901.
550 Y. Wu, H. Chen, F. Wang, F. Paesani and G. A. Voth, *J. Phys. Chem. B*, 2008, **112**, 467–482.
551 A. Stone, *The Theory of Intermolecular Forces*, Oxford University Press, 2013.
552 B. Coquinot, A. T. Bui, D. Toquer, A. Michaelides, N. Kavokine, S. J. Cox and L. Bocquet, *Nat. Nanotechnol.*, 2025, **20**, 397–403.
553 R. P. Misra and D. Blankschtein, *J. Phys. Chem. C*, 2017, **121**, 28166–28179.
554 V. Neklyudov and V. Freger, *Small*, 2024, **20**, e2402327.
555 J. Behler, *Angew. Chem., Int. Ed.*, 2017, **56**, 12828–12840.
556 V. L. Deringer, M. A. Caro and G. Csányi, *Adv. Mater.*, 2019, **31**, 1902765.

557 H. Ghorbanfekr, J. Behler and F. M. Peeters, *J. Phys. Chem. Lett.*, 2020, **11**, 7363–7370.
558 L. Zhang, H. Wang, R. Car and W. E, *Phys. Rev. Lett.*, 2021, **126**, 236001.
559 W. Zhao, H. Qiu and W. Guo, *J. Phys. Chem. C*, 2022, **126**, 10546–10553.
560 P. Sharma, S. Thomas, M. Nair and A. Govind Rajan, *J. Am. Chem. Soc.*, 2024, **146**, 30126–30138.
561 T. Morawietz, A. Singraber, C. Dellago and J. Behler, *Proc. Natl. Acad. Sci. U. S. A.*, 2016, **113**, 8368–8373.
562 H. Wang, L. Zhang, J. Han and W. E, *Comput. Phys. Commun.*, 2018, **228**, 178–184.
563 H. Wu, C. Liang, J. Jeong and N. R. Aluru, *J. Chem. Phys*, 2023, **159**, 184108.
564 M. F. Calegari Andrade, N. R. Aluru and T. A. Pham, *J. Phys. Chem. Lett.*, 2024, **15**, 6872–6879.
565 M. S. Kilic, M. Z. Bazant and A. Ajdari, *Phys. Rev. E*, 2007, **75**, 021502.
566 A. A. Kornyshev, *J. Phys. Chem. B*, 2007, **111**, 5545–5557.
567 P. M. Biesheuvel and M. Z. Bazant, *Phys. Rev. E*, 2016, **94**, 050601.
568 I. Vlassiouk, S. Smirnov and Z. Siwy, *ACS Nano*, 2008, **2**, 1589–1602.
569 M. Z. Bazant, M. S. Kilic, B. D. Storey and A. Ajdari, *Adv. Colloid Interface Sci.*, 2009, **152**, 48–88.
570 D. J. Bonthuis and R. R. Netz, *J. Phys. Chem. B*, 2013, **117**, 11397–11413.
571 J. Koplik and J. R. Banavar, *Annu. Rev. Fluid Mech.*, 1995, **27**, 257–292.
572 R. Qiao and N. R. Aluru, *Phys. Rev. Lett.*, 2004, **92**, 198301.
573 T. M. Squires and S. R. Quake, *Rev. Mod. Phys.*, 2005, **77**, 977.
574 A. Y. Grosberg, T. T. Nguyen and B. I. Shklovskii, *Rev. Mod. Phys.*, 2002, **74**, 329–345.
575 A. G. Moreira and R. R. Netz, *Eur. Phys. J. E*, 2002, **8**, 33–58.
576 D. J. Bonthuis, S. Gekle and R. R. Netz, *Phys. Rev. Lett.*, 2011, **107**, 166102.
577 M. Heiranian and N. R. Aluru, *ACS Nano*, 2019, **14**, 272–281.
578 M. Z. Bazant, B. D. Storey and A. A. Kornyshev, *Phys. Rev. Lett.*, 2011, **106**, 046102.
579 J. P. de Souza and M. Z. Bazant, *J. Phys. Chem. C*, 2020, **124**, 11414–11421.
580 R. P. Misra, J. P. de Souza, D. Blankschtein and M. Z. Bazant, *Langmuir*, 2019, **35**, 11550–11565.
581 B. D. Storey and M. Z. Bazant, *Phys. Rev. E*, 2012, **86**, 056303.
582 S. Y. Mashayak and N. R. Aluru, *J. Chem. Phys*, 2012, **137**, 214707.
583 S. Y. Mashayak and N. R. Aluru, *J. Chem. Phys*, 2018, **148**, 214102.
584 D. V. Matyushov, *J. Chem. Phys*, 2022, **157**, 080901.
585 W. Ren and E. Weinan, *J. Comput. Phys.*, 2005, **204**, 1–26.
586 K. Ritos, M. K. Borg, D. A. Lockerby, D. R. Emerson and J. M. Reese, *Microfluid. Nanofluid.*, 2015, **19**, 997–1010.
587 A. Horner and P. Pohl, *Faraday Discuss.*, 2018, **209**, 9–33.
588 C. Fang, D. Huang and J. Su, *J. Phys. Chem. Lett.*, 2020, **11**, 940–944.
589 J. Köfinger, G. Hummer and C. Dellago, *Phys. Chem. Chem. Phys.*, 2011, **13**, 15403–15417.
590 J. Kou, H. Lu, F. Wu, J. Fan and J. Yao, *Nano Lett.*, 2014, **14**, 4931–4936.
591 J. Kou, J. Yao, H. Lu, B. Zhang, A. Li, Z. Sun, J. Zhang, Y. Fang, F. Wu and J. Fan, *Angew. Chem., Int. Ed.*, 2015, **54**, 2351–2355.
592 L. Liu and G. N. Patey, *J. Chem. Phys*, 2016, **144**, 184502.
593 M. Melillo, F. Zhu, M. A. Snyder and J. Mittal, *J. Phys. Chem. Lett.*, 2011, **2**, 2978–2983.
594 A. Sam, V. Prasad and S. P. Sathian, *Phys. Chem. Chem. Phys.*, 2019, **21**, 6566–6573.
595 A. Waghe, J. C. Rasaiah and G. Hummer, *J. Chem. Phys*, 2012, **137**, 044709.
596 Y. Xu, X. Tian, M. Lv, M. Deng, B. He, P. Xiu, Y. Tu and Y. Zheng, *J. Phys. D:Appl. Phys.*, 2016, **49**, 285302.
597 Q. L. Zhang, R. Y. Yang, W. Z. Jiang and Z. Q. Huang, *Nanoscale*, 2016, **8**, 1886–1891.
598 J. Zhu, Y. Lan, H. Du, Y. Zhang and J. Su, *Phys. Chem. Chem. Phys.*, 2016, **18**, 17991–17996.
599 A. Horner, F. Zocher, J. Preiner, N. Ollinger, C. Siligan, S. A. Akimov and P. Pohl, *Sci. Adv.*, 2015, **1**, e1400083.
600 Z. Zhu, C. Chang, Y. Shu and B. Song, *J. Phys. Chem. Lett.*, 2020, **11**, 256–262.
601 J. Pfeffermann, N. Goessweiner-Mohr and P. Pohl, *Biophys. Rev.*, 2021, **13**, 913–923.
602 R. Mills, *J. Phys. Chem.*, 1973, **77**, 685–688.
603 M. Chen, L. Zheng, B. Santra, H.-Y. Ko, R. A. DiStasio Jr, M. L. Klein, R. Car and X. Wu, *Nat. Chem.*, 2018, **10**, 413–419.
604 C. A. Wraight, *Biochim. Biophys. Acta, Bioenerg.*, 2006, **1757**, 886–912.
605 K.-D. Kreuer, S. J. Paddison, E. Spohr and M. Schuster, *Chem. Rev.*, 2004, **104**, 4637–4678.
606 N. Agmon, *Chem. Phys. Lett.*, 1995, **244**, 456–462.
607 C. De Grotthuss, *Ann. Chim.*, 1806, **58**, 54–74.
608 S. Cukierman, *Biochim. Biophys. Act. (BBA) – Bioenerg.*, 2006, **1757**, 876–885.
609 H. Danneel, *Z. Elektrochem. Angew. Phys. Chem.*, 1905, **11**, 249–252.
610 C. Knight and G. A. Voth, *Acc. Chem. Res.*, 2012, **45**, 101–109.
611 C. T. Wolke, J. A. Fournier, L. C. Dzugan, M. R. Fagiani, T. T. Odbadrakh, H. Knorke, K. D. Jordan, A. B. McCoy, K. R. Asmis and M. A. Johnson, *Science*, 2016, **354**, 1131–1135.
612 D. Marx, M. E. Tuckerman, J. Hutter and M. Parrinello, *Nature*, 1999, **397**, 601–604.
613 N. Agmon, S. Y. Goldberg and D. Huppert, *J. Mol. Liq.*, 1995, **64**, 161–195.
614 H. Lapid, N. Agmon, M. K. Petersen and G. A. Voth, *J. Chem. Phys*, 2005, **122**, 14506.
615 O. Markovitch, H. Chen, S. Izvekov, F. Paesani, G. A. Voth and N. Agmon, *J. Phys. Chem. B*, 2008, **112**, 9456–9466.

616 H. Chen, B. Ilan, Y. Wu, F. Zhu, K. Schulten and G. A. Voth, *Biophys. J.*, 2007, **92**, 46–60.
617 H. S. Mei, M. E. Tuckerman, D. E. Sagnella and M. L. Klein, *J. Phys. Chem. B*, 1998, **102**, 10446–10458.
618 Y. Peng, J. M. J. Swanson, S.-G. Kang, R. Zhou and G. A. Voth, *J. Phys. Chem. B*, 2015, **119**, 9212–9218.
619 Y. Wu, B. Ilan and G. A. Voth, *Biophys. J.*, 2007, **92**, 61–69.
620 E. Tajkhorshid, P. Nollert, M. Jensen, L. J. Miercke, J. O'Connell, R. M. Stroud and K. Schulten, *Science*, 2002, **296**, 525–530.
621 M. C. Gordillo and J. Marti, *Chem. Phys. Lett.*, 2000, **329**, 341–345.
622 I. Hanasaki, A. Nakamura, T. Yonebayashi and S. Kawano, *J. Phys.:Condens. Matter*, 2007, **20**, 015213.
623 J. Köfinger, G. Hummer and C. Dellago, *Proc. Natl. Acad. Sci. U. S. A.*, 2008, **105**, 13218–13222.
624 Y. Maniwa, K. Matsuda, H. Kyakuno, S. Ogasawara, T. Hibi, H. Kadowaki, S. Suzuki, Y. Achiba and H. Kataura, *Nat. Mater.*, 2007, **6**, 135–141.
625 B. Mukherjee, P. K. Maiti, C. Dasgupta and A. Sood, *J. Phys. Chem. B*, 2009, **113**, 10322–10330.
626 U. Zimmerli, P. G. Gonnet, J. H. Walther and P. Koumoutsakos, *Nano Lett.*, 2005, **5**, 1017–1022.
627 K.-i Otake, K. Otsubo, T. Komatsu, S. Dekura, J. M. Taylor, R. Ikeda, K. Sugimoto, A. Fujiwara, C.-P. Chou, A. W. Sakti, Y. Nishimura, H. Nakai and H. Kitagawa, *Nat. Commun.*, 2020, **11**, 843.
628 X. Ma, C. Li, A. B. Martinson and G. A. Voth, *J. Phys. Chem. C*, 2020, **124**, 16186–16201.
629 Y. Matsuki, M. Iwamoto, K. Mita, K. Shigemi, S. Matsunaga and S. Oiki, *J. Am. Chem. Soc.*, 2016, **138**, 4168–4177.
630 M. Rossi, M. Ceriotti and D. E. Manolopoulos, *J. Phys. Chem. Lett.*, 2016, **7**, 3001–3007.
631 Y. Sun, C. Zhan, P. R. Kent and D.-E. Jiang, *J. Phys. Chem. C*, 2021, **125**, 11508–11512.
632 X. Yang, F. Yu, L. Wang, R. Liu, Y. Xin, R. Li, Y. Shi and Z. Wang, *J. Chem. Phys*, 2024, **160**, 194904.
633 T. Dumitric, C. M. Landis and B. I. Yakobson, *Chem. Phys. Lett.*, 2002, **360**, 182–188.
634 S. A. Hassan, G. Hummer and Y. S. Lee, *J. Chem. Phys*, 2006, **124**, 204510.
635 A. Chernyshev and S. Cukierman, *Biophys. J.*, 2002, **82**, 182–192.
636 T. E. Decoursey, *Physiol. Rev.*, 2003, **83**, 475–579.
637 P. Robin and L. Bocquet, *J. Chem. Phys*, 2023, **158**, 160901.
638 P. Robin, A. Delahais, L. Bocquet and N. Kavokine, *J. Chem. Phys*, 2023, **158**, 124703.
639 N. Kavokine, P. Robin and L. Bocquet, *J. Chem. Phys*, 2022, **157**, 114703.
640 J. Zhang, A. Kamenev and B. I. Shklovskii, *Phys. Rev. Lett.*, 2005, **95**, 148101.
641 Y. Avni, R. M. Adar, D. Andelman and H. Orland, *Phys. Rev. Lett.*, 2022, **128**, 098002.
642 A. B. Farimani, M. Heiranian and N. R. Aluru, *Sci. Rep.*, 2016, **6**, 26211.
643 R. P. Misra and D. Blankschtein, *J. Phys. Chem. C*, 2021, **125**, 2666–2679.
644 R. P. Misra and D. Blankschtein, *Langmuir*, 2021, **37**, 722–733.
645 W. Nernst, *Z. fur Phys. Chem.*, 1888, **2**, 613–637.
646 A. Einstein, *Ann. Phys.*, 1905, **4**, 549–560.
647 P. M. Chaikin, T. C. Lubensky and T. A. Witten, *Principles of Condensed Matter Physics*, Cambridge University Press, Cambridge, 1995, vol. 10.
648 G. Benenti, D. Donadio, S. Lepri and R. Livi, *Riv. Nuovo Cim.*, 2023, **46**, 105–161.
649 S. Baranovskii, T. Faber, F. Hensel, P. Thomas and G. Adriaenssens, *J. Non-Cryst. Solids.*, 1996, **198**, 214–217.
650 Y. A. Berlin, L. D. Siebbeles and A. A. Zharikov, *Chem. Phys. Lett.*, 1999, **305**, 123–131.
651 R. Richert, L. Pautmeier and H. Bässler, *Phys. Rev. Lett.*, 1989, **63**, 547.
652 B. Abou and F. Gallet, *Phys. Rev. Lett.*, 2004, **93**, 160603.
653 Q. Gu, E. A. Schiff, S. Grebner, F. Wang and R. Schwarz, *Phys. Rev. Lett.*, 1996, **76**, 3196.
654 K. Harada, A. Werner, M. Pfeiffer, C. Bloom, C. Elliott and K. Leo, *Phys. Rev. Lett.*, 2005, **94**, 036601.
655 Z. Li, M. Florian, K. Datta, Z. Jiang, M. Borsch, Q. Wen, M. Kira and P. B. Deotare, *ACS Nano*, 2023, **17**, 22410–22417.
656 G. Wetzelaer, L. Koster and P. Blom, *Phys. Rev. Lett.*, 2011, **107**, 066605.
657 H. Daiguji, P. Yang and A. Majumdar, *Nano Lett.*, 2004, **4**, 137–142.
658 C.-Y. Lin, C. Combs, Y.-S. Su, L.-H. Yeh and Z. S. Siwy, *J. Am. Chem. Soc.*, 2019, **141**, 3691–3698.
659 P. Dechadilok and W. M. Deen, *Ind. Eng. Chem. Res.*, 2006, **45**, 6953–6959.
660 E. M. Renkin, *J. Gen. Physiol.*, 1954, **38**, 225–243.
661 M. Manghi, J. Palmeri, K. Yazda, F. Henn and V. Jourdain, *Phys. Rev. E*, 2018, **98**, 012605.
662 Y. Uematsu, R. R. Netz, L. Bocquet and D. J. Bonthuis, *J. Phys. Chem. B*, 2018, **122**, 2992–2997.
663 S. Marbach and L. Bocquet, *Chem. Soc. Rev.*, 2019, **48**, 3102–3144.
664 Y. Baek, C. Kim, D. K. Seo, T. Kim, J. S. Lee, Y. H. Kim, K. H. Ahn, S. S. Bae, S. C. Lee, J. Lim, K. Lee and J. Yoon, *J. Membr. Sci.*, 2014, **460**, 171–177.
665 F. Du, L. Qu, Z. Xia, L. Feng and L. Dai, *Langmuir*, 2011, **27**, 8437–8443.
666 B. Lee, Y. Baek, M. Lee, D. H. Jeong, H. H. Lee, J. Yoon and Y. H. Kim, *Nat. Commun.*, 2015, **6**, 7109.
667 M. Majumder and B. Corry, *Chem. Commun.*, 2011, **47**, 7683–7685.
668 H. Matsumoto, S. Tsuruoka, Y. Hayashi, K. Abe, K. Hata, S. Zhang, Y. Saito, M. Aiba, T. Tokunaga, T. Iijima, T. Hayashi, H. Inoue and G. A. J. Amaratunga, *Carbon*, 2017, **120**, 358–365.
669 D. Mattia, H. Leese and K. P. Lee, *J. Membr. Sci.*, 2015, **475**, 266–272.

670 S. Sinha, M. Pia Rossi, D. Mattia, Y. Gogotsi and H. H. Bau, *Phys. Fluids*, 2007, **19**, 013603.
671 S. Trivedi and K. Alameh, *SpringerPlus*, 2016, **5**, 1158.
672 M. Yu, H. H. Funke, J. L. Falconer and R. D. Noble, *Nano Lett.*, 2009, **9**, 225–229.
673 L. Zhang, B. Zhao, C. Jiang, J. Yang and G. Zheng, *Nanoscale Res. Lett.*, 2015, **10**, 1–8.
674 S. Cetindag, S. J. Park, S. F. Buchsbaum, Y. Zheng, M. Liu, S. Wang, R. Xiang, S. Maruyama, F. Fornasiero and J. W. Shan, *ACS Nano*, 2024, **18**, 355–363.
675 M. Heiranian, A. Taqieddin and N. R. Aluru, *Phys. Rev. Res.*, 2020, **2**, 043153.
676 K. E. Karim, M. Barisik, C. Bakli and B. Kim, *Phys. Chem. Chem. Phys.*, 2024, **26**, 19069–19082.
677 Z. Zhu, S. Lv, Q. Gao, S. Zhao and X. Lu, *J. Membr. Sci.*, 2022, **644**, 120157.
678 S. K. Kannam, P. J. Daivis and B. D. Todd, *MRS Bull.*, 2017, **42**, 283–288.
679 M. Majumder, A. Siria and L. Bocquet, *MRS Bull.*, 2017, **42**, 278–282.
680 M. Xue, Z. Hu, H. Qiu, C. Shen, W. Guo and Z. Zhang, *Natl. Sci. Rev.*, 2022, **9**, nwab214.
681 W. D. Nicholls, M. K. Borg, D. A. Lockerby and J. M. Reese, *Mol. Simul.*, 2012, **38**, 781–785.
682 J. Zhu, E. Zhu, J. Gao, X. Li and J. Su, *J. Chem. Phys*, 2018, **149**, 074703.
683 M. Elimelech and W. A. Phillip, *Science*, 2011, **333**, 712–717.
684 M. M. Pendergast and E. M. V. Hoek, *Energy Environ. Sci.*, 2011, **4**, 1946–1971.
685 B. Corry, *Energy Environ. Sci.*, 2011, **4**, 751–759.
686 C. H. Ahn, Y. Baek, C. Lee, S. O. Kim, S. Kim, S. Lee, S. H. Kim, S. S. Bae, J. Park and J. Yoon, *J. Ind. Eng. Chem.*, 2012, **18**, 1551–1559.
687 R. Das, M. E. Ali, S. B. A. Hamid, S. Ramakrishna and Z. Z. Chowdhury, *Desalination*, 2014, **336**, 97–109.
688 S. Kar, R. Bindal and P. Tewari, *Nano Today*, 2012, **7**, 385–389.
689 H. B. Park, J. Kamcev, L. M. Robeson, M. Elimelech and B. D. Freeman, *Science*, 2017, **356**, eaab0530.
690 B. Grosjean, M.-L. Bocquet and R. Vuilleumier, *Nat. Commun.*, 2019, **10**, 1656.
691 W. M. Haynes, *Crc Handbook of Chemistry and Physics*, CRC Press, Boca Raton, FL, 97th edn, 2016.
692 Y. Wang, Z. Wang, L. Wang, T. Tong, X. Zhang, S. Fang, W. Xie, L. Liang, B. Yin, J. Yuan, J. Zhang and D. Wang, *Nano Lett.*, 2022, **22**, 2147–2154.
693 L. Bsawmaii, C. Delacou, V. Kotok, S. Méance, K. Saada, M. A. Kribeche, S. Tahir, C. Roblin, A. Louiset, H. Okuno, M. Manghi, J. Palmeri, F. Henn, A. Noury and V. Jourdain, *Nanoscale*, 2024, **16**, 21970–21978.
694 P. Liu, X.-Y. Kong, L. Jiang and L. Wen, *Chem. Soc. Rev.*, 2024, **53**, 2972–3001.
695 B. Hille, *J. Gen. Physiol*, 1968, **51**, 221–236.
696 J. E. Hall, *J. Gen. Physiol*, 1975, **66**, 531–532.
697 R. M. Smeets, U. F. Keyser, D. Krapf, M. Y. Wu, N. H. Dekker and C. Dekker, *Nano Lett.*, 2006, **6**, 89–95.
698 L. M. Alvero-González, M. Aguilella-Arzo, D. A. Perini, L. A. Bergdoll, M. Queralt-Martín and A. Alcaraz, *Nanoscale Adv.*, 2024, **6**, 6344–6357.
699 M. Queralt-Martin, M. L. Lopez, M. Aguilella-Arzo, V. M. Aguilella and A. Alcaraz, *Nano Lett.*, 2018, **18**, 6604–6610.
700 A. Esfandiar, B. Radha, F. C. Wang, Q. Yang, S. Hu, S. Garaj, R. R. Nair, A. K. Geim and K. Gopinadhan, *Science*, 2017, **358**, 511–513.
701 Y. Jiang, R. Hu, C. Yang, Z. Zhou, G. Yuan, H. Zhou and S. Hu, *Sci. Adv.*, 2023, **9**, eadi8493.
702 S. Hong, F. Ming, Y. Shi, R. Li, I. S. Kim, C. Y. Tang, H. N. Alshareef and P. Wang, *ACS Nano*, 2019, **13**, 8917–8925.
703 Y. Noh and N. R. Aluru, *ACS Nano*, 2020, **14**, 10518–10526.
704 W. B. S. de Lint, P. M. Biesheuvel and H. Verweij, *J. Colloid Interface Sci.*, 2002, **251**, 131–142.
705 B. W. Ninham and V. A. Parsegian, *J. Theor. Biol.*, 1971, **31**, 405–428.
706 R. Podgornik, *J. Chem. Phys*, 1989, **91**, 5840–5849.
707 B. Grosjean, C. Pean, A. Siria, L. Bocquet, R. Vuilleumier and M. L. Bocquet, *J. Phys. Chem. Lett.*, 2016, **7**, 4695–4700.
708 E. Mangaud, M. L. Bocquet, L. Bocquet and B. Rotenberg, *J. Chem. Phys*, 2022, **156**, 044703.
709 P. M. Biesheuvel and M. Z. Bazant, *Phys. Rev. E*, 2016, **94**, 050601.
710 A. Levy, J. P. de Souza and M. Z. Bazant, *J. Colloid Interface Sci.*, 2020, **579**, 162–176.
711 J. P. de Souza, A. Levy and M. Z. Bazant, *Phys. Rev. E*, 2021, **104**, 044803.
712 Y. Green, *J. Chem. Phys*, 2021, **155**, 184701.
713 Z. X. Luo, Y. Z. Xing, Y. C. Ling, A. Kleinhammes and Y. Wu, *Nat. Commun.*, 2015, **6**, 6358.
714 T. Mouterde and L. Bocquet, *Eur. Phys. J. E*, 2018, **41**, 1–10.
715 A. Panahi, P. Sadeghi, A. Akhlaghi and M. H. Sabour, *Diamond Relat. Mater.*, 2020, **110**, 108105.
716 J. D. Jackson, *Classical Electrodynamics*, John Wiley & Sons, 2012.
717 G. Lamoureux and B. Roux, *J. Chem. Phys*, 2003, **119**, 3025–3039.
718 T. Pichler, M. Knupfer, M. S. Golden, J. Fink, A. Rinzler and R. E. Smalley, *Phys. Rev. Lett.*, 1998, **80**, 4729–4732.
719 E. N. Brothers, G. E. Scuseria and K. N. Kudin, *J. Phys. Chem. B*, 2006, **110**, 12860–12864.
720 B. Kozinsky and N. Marzari, *Phys. Rev. Lett.*, 2006, **96**, 166801.
721 W. Lu, D. Wang and L. Chen, *Nano Lett.*, 2007, **7**, 2729–2733.
722 G. Cicero, J. C. Grossman, E. Schwegler, F. Gygi and G. Galli, *J. Am. Chem. Soc.*, 2008, **130**, 1871–1878.
723 V. Rozsa, T. A. Pham and G. Galli, *J. Chem. Phys*, 2020, **152**, 124501.
724 S. Mondal and B. Bagchi, *J. Phys. Chem. Lett.*, 2019, **10**, 6287–6292.

725 E. Papadopoulou, J. Zavadlav, R. Podgornik, M. Praprotnik and P. Koumoutsakos, *ACS Nano*, 2021, **15**, 20311–20318.
726 H. Zhu, A. Ghoufi, A. Szymczyk, B. Balannec and D. Morineau, *Phys. Rev. Lett.*, 2012, **109**, 107801.
727 D. Donadio, G. Cicero, E. Schwegler, M. Sharma and G. Galli, *J. Phys. Chem. B*, 2009, **113**, 4170–4175.
728 M. Sharma, D. Donadio, E. Schwegler and G. Galli, *Nano Lett.*, 2008, **8**, 2959–2962.
729 J. A. Fagan, C. Y. Khripin, C. A. Silvera Batista, J. R. Simpson, E. H. Hároz, A. R. Hight Walker and M. Zheng, *Adv. Mater.*, 2014, **26**, 2800–2804.
730 R. A. Sampson, *Philos. Trans. R. Soc. A*, 1891, 449–518.
731 H. L. Weissberg, *Phys. Fluids*, 1962, **5**, 1033–1036.
732 B. Hille, *J. Gen. Physiol*, 1968, **51**, 199–219.
733 H. Kumar, B. Mukherjee, S. T. Lin, C. Dasgupta, A. K. Sood and P. K. Maiti, *J. Chem. Phys.*, 2011, **134**, 124105.
734 Y. Hong, J. Zhang, C. Zhu, X. C. Zeng and J. S. Francisco, *J. Mater. Chem. A*, 2019, **7**, 3583–3591.
735 S. R. Varanasi, Y. Subramanian and S. K. Bhatia, *Langmuir*, 2018, **34**, 8099–8111.
736 S. Gravelle, L. Joly, F. Detcheverry, C. Ybert, C. Cottin-Bizonne and L. Bocquet, *Proc. Natl. Acad. Sci. U. S. A.*, 2013, **110**, 16367–16372.
737 F. G. Donnan, *Chem. Rev.*, 1924, **1**, 73–90.
738 Q. Wang, X. Zhang, H. Zhu, X. Zhang, Q. Liu, M. Fu, J. Zhu, J. Pu and Z. Qu, *Adv. Phys. Res.*, 2023, **2**, 2300016.
739 V. Freger, *Faraday Discuss.*, 2018, **209**, 371–388.
740 J. H. Park, S. B. Sinnott and N. R. Aluru, *Nanotechnology*, 2006, **17**, 895–900.
741 Q. Wang, J. Song, X. Gao, L. Liu and C. Liu, *Desalination*, 2022, **540**, 115996.
742 L. Yang and S. Garde, *J. Chem. Phys*, 2007, **126**, 084706.
743 X. Zhan, J. Wu, Z. Chen and B. J. Hinds, *Nanoscale Res. Lett.*, 2013, **8**, 1–11.
744 S. Zhang, L. Fu and Y. Xie, *J. Phys. Chem. B*, 2024, **128**, 9206–9212.
745 J. Hou and H. Zhang, *Adv. Mater. Technol.*, 2023, **8**, 2201433.
746 J. Schaep, B. Van der Bruggen, C. Vandecasteele and D. Wilms, *Sep. Purif. Technol.*, 1998, **14**, 155–162.
747 S. S. Wong, E. Joselevich, A. T. Woolley, C. L. Cheung and C. M. Lieber, *Nature*, 1998, **394**, 52–55.
748 S. S. Wong, A. T. Woolley, E. Joselevich, C. L. Cheung and C. M. Lieber, *J. Am. Chem. Soc.*, 1998, **120**, 8557–8558.
749 Z. He, J. Zhou, X. Lu and B. Corry, *J. Phys. Chem. C*, 2013, **117**, 11412–11420.
750 R. Epsztein, E. Shaulsky, N. Dizge, D. M. Warsinger and M. Elimelech, *Environ. Sci. Technol.*, 2018, **52**, 4108–4116.
751 G. De Luca, J. Luque Di Salvo, A. Cipollina, G. L. Luque, A. Fuoco, E. P. M. Leiva and G. Micale, *Desalination*, 2022, **544**, 116123.
752 B. Tansel, *Sep. Purif. Technol.*, 2012, **86**, 119–126.
753 K. E. Moore, M. Pfohl, D. D. Tune, F. Hennrich, S. Dehm, V. S. K. Chakradhanula, C. Kubel, R. Krupke and B. S. Flavel, *ACS Nano*, 2015, **9**, 3849–3857.
754 X. Xu, X. Jin, M. Kuehne, D.-L. Bao, J. Martis, Y.-M. Tu, C. L. Ritt, J. C. Idrobo, M. S. Strano and A. Majumdar, *arXiv*, 2024, preprint, arXiv:2402.17989, DOI: **10.48550/arXiv.2402.17989**.
755 G. Gonella, E. H. G. Backus, Y. Nagata, D. J. Bonthuis, P. Loche, A. Schlaich, R. R. Netz, A. Kühnle, I. T. McCrum, M. T. M. Koper, M. Wolf, B. Winter, G. Meijer, R. K. Campen and M. Bonn, *Nat. Rev. Chem.*, 2021, **5**, 466–485.
756 A. Greco, S. Imoto, E. H. G. Backus, Y. Nagata, J. Hunger and M. Bonn, *Science*, 2025, **388**, 405–410.
757 J. Comtet, B. Grosjean, E. Glushkov, A. Avsar, K. Watanabe, T. Taniguchi, R. Vuilleumier, M. L. Bocquet and A. Radenovic, *Nat. Nanotechnol.*, 2020, **15**, 598–604.
758 N. Ronceray, Y. You, E. Glushkov, M. Lihter, B. Rehl, T. H. Chen, G. H. Nam, F. Borza, K. Watanabe, T. Taniguchi, S. Roke, A. Keerthi, J. Comtet, B. Radha and A. Radenovic, *Nat. Mater.*, 2023, **22**, 1236–1242.
759 H. Bazyar, O. A. Moultos and R. G. H. Lammertink, *J. Chem. Phys*, 2022, **157**, 144704.
760 L. Liang, Z. Zhang, J.-W. Shen and X.-Y. Liu, *J. Phys. Chem. C*, 2017, **121**, 19512–19518.
761 B. H. S. Mendonça, D. N. de Freitas, M. H. Köhler, R. J. C. Batista, M. C. Barbosa and A. B. de Oliveira, *Phys. A*, 2019, **517**, 491–498.
762 X. Zhou, F. Wu, J. Kou, X. Nie, Y. Liu and H. Lu, *J. Phys. Chem. B*, 2013, **117**, 11681–11686.
763 L. Hang-Jun, G. Xiao-Jing, W. Chun-Lei, F. Hai-Ping and W. Rong-Zheng, *Chin. Phys. Lett.*, 2008, **25**, 1145.
764 H. Qiu, R. Shen and W. Guo, *Nano Res.*, 2010, **4**, 284–289.
765 Q.-L. Zhang, W.-Z. Jiang, J. Liu, R.-D. Miao and N. Sheng, *Phys. Rev. Lett.*, 2013, **110**, 254501.
766 J. Li, X. Gong, H. Lu, D. Li, H. Fang and R. Zhou, *Proc. Natl. Acad. Sci. U. S. A.*, 2007, **104**, 3687–3692.
767 Y.-C. Yao, Z. Li, A. J. Gillen, S. Yosinski, M. A. Reed and A. Noy, *J. Chem. Phys*, 2021, **154**, 204704.
768 K. F. Rinne, S. Gekle, D. J. Bonthuis and R. R. Netz, *Nano Lett.*, 2012, **12**, 1780–1783.
769 T. Hennequin, M. Manghi, A. Noury, F. Henn, V. Jourdain and J. Palmeri, *J. Phys. Chem. Lett.*, 2024, **15**, 2177–2183.
770 F. Lv, C. Fang and J. Su, *Nanotechnology*, 2019, **30**, 245707.
771 W. Cao, J. Wang and M. Ma, *J. Micromech. Microeng.*, 2018, **28**, 033001.
772 M. Karimzadeh, M. Khatibi, S. N. Ashrafizadeh and P. K. Mondal, *Phys. Chem. Chem. Phys.*, 2022, **24**, 20303–20317.
773 X. Chen, X. Zhang, S. Li and J. Su, *New J. Chem.*, 2022, **46**, 8239–8249.
774 Z. Fu, Y. Luo, J. Ma and G. Wei, *J. Chem. Phys*, 2011, **134**, 154507.
775 D. Ostler, S. K. Kannam, P. J. Daivis, F. Frascoli and B. D. Todd, *J. Phys. Chem. C*, 2017, **121**, 28158–28165.
776 H. F. Ye, H. W. Zhang, Z. Chen, Y. G. Zheng, Z. Zong and Z. Q. Zhang, *Microfluid. Nanofluid.*, 2015, **18**, 1201–1207.
777 X. Zhang and J. Su, *J. Mol. Liq.*, 2021, **328**, 115382.
778 K. Ritos, M. K. Borg, N. J. Mottram and J. M. Reese, *Philos. Trans. R. Soc., A*, 2016, **374**, 20150025.

779 L. Figueras and J. Faraudo, *Mol. Simul.*, 2012, **38**, 23–25.
780 J. A. Garate, N. J. English and J. M. MacElroy, *J. Chem. Phys*, 2009, **131**, 114508.
781 P. K. Mondal, U. Ghosh, A. Bandopadhyay, D. DasGupta and S. Chakraborty, *Phys. Rev. E*, 2013, **88**, 023022.
782 A. Gogoi, K. A. Reddy and P. K. Mondal, *Phys. Fluids*, 2021, **33**, 092115.
783 P. Kumar Mondal and S. Wongwises, *Proc. Inst. Mech. Eng., Part E*, 2020, **234**, 318–330.
784 S. Shyam, B. Dhapola and P. K. Mondal, *J. Fluid Mech.*, 2022, **944**, A51.
785 H. Li, S. Wang, J. Zheng and J. Wang, *J. Phys. Chem. C*, 2024, **128**, 21190–21200.
786 Y. Wu, Z. Wang, S. Li and J. Su, *Phys. Chem. Chem. Phys.*, 2024, **26**, 10919–10931.
787 T. Zhang, Z. Wang, S. Li, X. Zhang and J. Su, *Langmuir*, 2024, **40**, 27104–27113.
788 D. Deamer, M. Akeson and D. Branton, *Nat. Biotechnol.*, 2016, **34**, 518–524.
789 H. Gao, Y. Kong, D. Cui and C. S. Ozkan, *Nano Lett.*, 2003, **3**, 471–473.
790 J. He, H. Liu, P. Pang, D. Cao and S. Lindsay, *J. Phys.:Condens. Matter*, 2010, **22**, 454112.
791 R. Peng, X. S. Tang and D. Li, *Small*, 2018, **14**, 1800013.
792 W. Liu, T. Mei, Z. Cao, C. Li, Y. Wu, L. Wang, G. Xu, Y. Chen, Y. Zhou, S. Wang, Y. Xue, Y. Yu, X.-Y. Kong, R. Chen, B. Tu and K. Xiao, *Sci. Adv.*, 2024, **10**, eadj7867.
793 E. Y. M. Ang, W. Toh, J. Yeo, R. Lin, Z. Liu, K. R. Geethalakshmi and T. Y. Ng, *J. Membr. Sci.*, 2020, **598**, 117785.
794 Y. Baek, D. K. Seo, J. H. Choi, B. Lee, Y. H. Kim, S. M. Park, J. Jung, S. Lee and J. Yoon, *Desalin. Water Treat.*, 2016, **57**, 28133–28140.
795 M. Barrejón and M. Prato, *Adv. Mater. Interfaces*, 2021, 2101260.
796 J. Cao, Z. Xu, M. Wei, L. Li, B. Wu and Y. Wang, *Desalination*, 2025, **593**, 118217.
797 A. Güvensoy-Morkoyun, S. Kürklü-Kocaolu, C. Yldrm, S. Veliolu, H. E. Karahan, T.-H. Bae and B. Tantekin-Ersolmaz, *Carbon*, 2021, **185**, 546–557.
798 M. Thomas and B. Corry, *Philos. Trans. R. Soc., A*, 2016, **374**, 20150020.
799 M. Thomas and B. Corry, *J. Phys. Chem. C*, 2020, **124**, 3820–3826.
800 M. Thomas, B. Corry and T. A. Hilder, *Small*, 2014, **10**, 1453–1465.
801 M. A. Tofighy, Y. Shirazi, T. Mohammadi and A. Pak, *Chem. Eng. J.*, 2011, **168**, 1064–1072.
802 J. R. Werber, C. O. Osuji and M. Elimelech, *Nat. Rev. Mater.*, 2016, **1**, 16018.
803 Winarto, E. Yamamoto and K. Yasuoka, *Phys. Chem. Chem. Phys.*, 2019, **21**, 15431–15438.
804 J. Azamat, J. J. Sardroodi and A. Rastkar, *RSC Adv.*, 2014, **4**, 63712–63718.
805 M. Y. Xiong, K. W. Song and J. P. Leburton, *Nano Energy*, 2023, **117**, 108860.
806 Y. Jiang, W. Liu, T. Wang, Y. Wu, T. Mei, L. Wang, G. Xu, Y. Wang, N. Liu and K. Xiao, *Nat. Commun.*, 2024, **15**, 8582.
807 Q. Yuan and Y. P. Zhao, *J. Am. Chem. Soc.*, 2009, **131**, 6374–6376.
808 P. Král and M. Shapiro, *Phys. Rev. Lett.*, 2001, **86**, 131–134.
809 Y. Zhao, L. Song, K. Deng, Z. Liu, Z. Zhang, Y. Yang, C. Wang, H. Yang, A. Jin and Q. Luo, *Adv. Mater.*, 2008, **20**, 1772.
810 J. R. Werber and M. Elimelech, *Sci. Adv.*, 2018, **4**, eaar8266.
811 B. Fadeel and K. Kostarelos, *Nat. Nanotechnol.*, 2020, **15**, 164.
812 S. F. Hansen and A. Lennquist, *Nat. Nanotechnol.*, 2020, **15**, 3–4.
813 D. A. Heller, P. V. Jena, M. Pasquali, K. Kostarelos, L. G. Delogu, R. E. Meidl, S. V. Rotkin, D. A. Scheinberg, R. E. Schwartz, M. Terrones, Y. Wang, A. Bianco, A. A. Boghossian, S. Cambré, L. Cognet, S. R. Corrie, P. Demokritou, S. Giordani, T. Hertel, T. Ignatova, M. F. Islam, N. M. Iverson, A. Jagota, D. Janas, J. Kono, S. Kruss, M. P. Landry, Y. Li, R. Martel, S. Maruyama, A. V. Naumov, M. Prato, S. J. Quinn, D. Roxbury, M. S. Strano, J. M. Tour, R. B. Weisman, W. Wenseleers and M. Yudasaka, *Nat. Nanotechnol.*, 2020, **15**, 164–166.
814 K. K. Das, Y. You, M. Torres, F. Barrios-Masias, X. Wang, S. Tao, B. Xing and Y. Yang, *Environ. Sci.:Nano*, 2018, **5**, 659–668.
815 F. Gottschalk, T. Sonderer, R. W. Scholz and B. Nowack, *Environ. Sci. Technol.*, 2009, **43**, 9216–9222.
816 T. Y. Sun, D. M. Mitrano, N. A. Bornhöft, M. Scheringer, K. Hungerbühler and B. Nowack, *Environ. Sci. Technol.*, 2017, **51**, 2854–2863.
817 B. Avant, D. Bouchard, X. Chang, H.-S. Hsieh, B. Acrey, Y. Han, J. Spear, R. Zepp and C. D. Knightes, *NanoImpact*, 2019, **13**, 1–12.
818 M. Morozesk, L. S. Franqui, F. C. Pinheiro, J. A. Nóbrega, D. S. T. Martinez and M. N. Fernandes, *Ecotoxicol. Environ. Saf.*, 2020, **202**, 110892.
819 J. Bornholdt, A. T. Saber, B. Lilje, M. Boyd, M. Jørgensen, Y. Chen, M. Vitezic, N. R. Jacobsen, S. S. Poulsen and T. Berthing, *ACS Nano*, 2017, **11**, 3597–3613.
820 C.-W. Lam, J. T. James, R. McCluskey and R. L. Hunter, *Toxicol. Sci.*, 2004, **77**, 126–134.
821 C. A. Poland, R. Duffin, I. Kinloch, A. Maynard, W. A. Wallace, A. Seaton, V. Stone, S. Brown, W. MacNee and K. Donaldson, *Nat. Nanotechnol.*, 2008, **3**, 423–428.
822 J. Zhao, W. Luo, Y. Xu, J. Ling and L. Deng, *Sci. Total Environ.*, 2021, **766**, 142652.
823 E. D. Kuempel, M.-C. Jaurand, P. Møller, Y. Morimoto, N. Kobayashi, K. E. Pinkerton, L. M. Sargent, R. C. Vermeulen, B. Fubini and A. B. Kane, *Crit. Rev. Toxicol.*, 2017, **47**, 1–58.
824 W. Zhu, A. Von Dem Bussche, X. Yi, Y. Qiu, Z. Wang, P. Weston, R. H. Hurt, A. B. Kane and H. Gao, *Proc. Natl. Acad. Sci. U. S. A.*, 2016, **113**, 12374–12379.
825 D.-K. Lee, S. Jeon, Y. Han, S.-H. Kim, S. Lee, I. J. Yu, K. S. Song, A. Kang, W. S. Yun and S.-M. Kang, *ACS Nano*, 2018, **12**, 10867–10879.

826 S. Alidori, N. Akhavein, D. L. Thorek, K. Behling, Y. Romin, D. Queen, B. J. Beattie, K. Manova-Todorova, M. Bergkvist and D. A. Scheinberg, *et al.*, *Sci. Transl. Med.*, 2016, **8**, 331ra39.

827 F. A. Murphy, C. A. Poland, R. Duffin, K. T. Al-Jamal, H. Ali-Boucetta, A. Nunes, F. Byrne, A. Prina-Mello, Y. Volkov and S. Li, *Am. J. Pathol.*, 2011, **178**, 2587–2600.

828 S. Alidori, D. L. Thorek, B. J. Beattie, D. Ulmert, B. A. Almeida, S. Monette, D. A. Scheinberg and M. R. McDevitt, *PLoS One*, 2017, **12**, e0183902.

829 H. Aliâ-Boucetta, A. Nunes, R. Sainz, M. A. Herrero, B. Tian, M. Prato, A. Bianco and K. Kostarelos, *Angew. Chem., Int. Ed.*, 2013, **52**, 2274–2278.

830 H. Nagai, Y. Okazaki, S. H. Chew, N. Misawa, Y. Yamashita, S. Akatsuka, T. Ishihara, K. Yamashita, Y. Yoshikawa and H. Yasui, *Proc. Natl. Acad. Sci. U. S. A.*, 2011, **108**, E1330–E1338.

831 V. E. Kagan, N. V. Konduru, W. Feng, B. L. Allen, J. Conroy, Y. Volkov, I. I. Vlasova, N. A. Belikova, N. Yanamala, A. Kapralov, Y. Y. Tyurina, J. Shi, E. R. Kisin, A. R. Murray, J. Franks, D. Stolz, P. Gou, J. Klein-Seetharaman, B. Fadeel, A. Star and A. A. Shvedova, *Nat. Nanotechnol.*, 2010, **5**, 354–359.

832 D. Elgrabli, W. Dachraoui, C. Ménard-Moyon, X. J. Liu, D. Bégin, S. Bégin-Colin, A. Bianco, F. Gazeau and D. Alloyeau, *ACS Nano*, 2015, **9**, 10113–10124.

833 C. Bussy, K. T. Al-Jamal, J. Boczkowski, S. Lanone, M. Prato, A. Bianco and K. Kostarelos, *ACS Nano*, 2015, **9**, 7815–7830.

834 A. E. Goode, D. A. G. Carter, M. Motskin, I. S. Pienaar, S. Chen, S. Hu, P. Ruenraroengsak, M. P. Ryan, M. S. Shaffer and D. T. Dexter, *Biomaterials*, 2015, **70**, 57–70.